8-2006

Growth and Superconductivity of Pb and Pb-Bi Alloys in the Quantum Regime

Mustafa Murat Ozer

To the Graduate Council:

I am submitting herewith a dissertation written by Mustafa Murat Ozer entitled "Growth and Superconductivity of Pb and Pb-Bi Alloys in the Quantum Regime." I have examined the final electronic copy of this dissertation for form and content and recommend that it be accepted in partial fulfillment of the requirements for the degree of Doctor of Philosophy, with a major in Physics.

Hanno H. Weitering, Major Professor

We have read this dissertation and recommend its acceptance:

James R. Thompson, E. Ward Plummer, Takeshi Egami, Robert N. Compton

Accepted for the Council:
Dixie L. Thompson

Vice Provost and Dean of the Graduate School

(Original signatures are on file with official student records.)

To the Graduate Council:

I am submitting herewith a dissertation written by Mustafa Murat Özer entitled "Growth and Superconductivity of Pb and Pb-Bi Alloys in the Quantum Regime". I have examined the final electronic copy of this dissertation for form and content and recommend that it be accepted in partial fulfillment of the requirements for the degree of Doctor of Philosophy, with a major in Physics.

Hanno H Weitering, Major Professor

We have read this dissertation
and recommend its acceptance:

James R Thompson

E. Ward Plummer

Takeshi Egami

Robert N Compton

Accepted for the Council:

Anne Mayhew

Vice Chancellor and Dean of

Graduate Studies

(Original signatures are on file with official student records.)

Growth and Superconductivity of Pb and Pb-Bi Alloys in the Quantum Regime

A Dissertation

Presented for the

Doctor of Philosophy

Degree

The University of Tennessee, Knoxville

Mustafa Murat Özer

August 2006

Acknowledgements

As usual, but definitely not since customary, my deepest and sincere gratitude are reserved for my primary advisor Prof. Dr. Hanno H. Weitering and co-advisor Prof. Dr. James R. Thompson.

Dr. Weitering, “who has shown me the light” some years ago, has been initiative for a fruitful research period. It has been a pleasure to utilize his wide experience and work as a member of his group. Besides being available all the time for my endless questions, he has also been a very patient teacher. His justice as a group leader, as well as being the cornerstone of peace in such a productive group can never be emphasized enough.

Dr. Thompson carries the whole of physics in his pockets and is always ready to give you a bunch - usually more than you would ask for. Horizons you can reach during his discussions are by no means limited. Anytime you should be ready to see how the number π can be determined experimentally or how the phases of the moon could affect magnetization measurements. A substantial part of my work simply could not be done without his patronize.

Abstract

Superconductivity is a collective quantum phenomenon that is inevitably suppressed in reduced dimensionality. Questions of how thin superconducting wires or films can be before they lose their superconducting properties have important technological ramifications and go to the heart of understanding formation, coherence, and robustness of the superconducting state in quantum confined geometries. Suppression of superconductivity in low dimensions is usually attributed to thermal or quantum fluctuations, or to pair-breaking Coulomb interactions in the presence of strong disorder. Control and quantification of a film's disorder length scale remained a critical experimental obstacle, however. Here, we exploit quantum confinement of itinerant electrons in a soft metal (Pb), to stabilize atomically-flat superconductors with lateral dimensions of the order of a few millimeters and vertical dimensions of only a few atomic layers. These extremely thin superconductors show no indication of defect- or fluctuation-driven suppression of superconductivity and sustain *macroscopic* super-currents of up to ~10% of the theoretical depairing current density. The extreme hardness of the critical state can be attributed to the presence of intrinsic vortex traps that are stabilized by quantum confinement. We furthermore show that the quantum growth and superconductive properties of the films can be tailored by Fermi surface engineering via controlled alloying. The present study paints a conceptually appealing, elegant picture of a model nano-scale superconductor with calculable critical state properties. It furthermore

indicates the intriguing possibility of achieving and exploiting superconductivity in the ultimate low-dimensional limit.

Contents

List of Figures

Chapter 1

Introduction

1.1 Cooperative Quantum Phenomena in Artificial Solids

The final chapters of textbooks on solid-state physics mostly deal with classical and quantum cooperative phenomena, which merge solid-state concepts of structure and electronic structure with statistical mechanics. In all examples of ferroelectricity, ferromagnetism, charge density waves, and superconductivity, the presence of long-range order relies on a delicate balance between the internal energy and entropy of the system. The latter, being largely a function of dimensionality,[1] makes cooperative phenomena in low dimensional systems very interesting and radically different from those in the bulk, particularly when considering their spatial coherence.

The possibility of establishing superconducting quantum coherence over macroscopic length scales is maybe one of the most intriguing issues in this context. When superconducting materials are made very small or thin, they often lose their ability

to ‘superconduct’. The culprit is entropy which, loosely speaking, refers to nature’s tendency to maximize disorder. Entropy effects (or thermodynamic ‘fluctuations’) are always more dramatic in low-dimensional geometries. In macroscopic superconductors, paired electrons or ‘Cooper pairs’ carry the super-currents. Cooper pairs all have to ‘dance in step’ so as to form a macroscopic quantum mechanical wave. As the size of the superconductor is reduced to the nano-scale, more and more Cooper pairs become disorganized. Hence, quantum mechanical coherence or superconducting order is destroyed and the material generally loses its ability to carry electrical currents without resistance. This concept is of course very important in designing future superconducting nano-devices because fail-proof quantum computing requires strong phase coherence. In particular, “coherence” is the keyword in nearly all of the forefront reports on quantum computing.[2]

It is evident that exploring the laws of physics in low dimensionality is essential from both a scientific and technological point of view. In fact, experimental practicalities and fundamental physics seem even more heavily intertwined in low dimensions. For example, due to the topology of low dimensional systems, the consequence of the inevitable fabrication defects or structural imperfections on the *macroscopic* physical properties is profound. To be more specific, sample imperfections, which could be tolerated to some extend in bulk systems, may cause a tremendous loss of macroscopic phase coherence in the superconductive state. In their 1998 Physics Today article on 2D superconductivity, Allen Goldman and Nina Markovic pointed out that “control and quantification of a film’s disorder length scale represent a critical experimental problem.”[3] In this thesis, we have made significant progress toward the quality control of

low-dimensional superconductors by using the tools and knowledge base of surface science. As we will show, the superconductive properties of high quality Pb films and Pb-Bi alloy films are surprisingly robust.

The availability of the "well defined clean surface" dates back to the 1970's when Ultra High Vacuum (~10^{-10} mbar) or UHV equipment became available. This made it possible to prepare and maintain atomically clean samples for extended periods of time. Photoelectron spectroscopy and Auger electron spectroscopy allowed for in-situ monitoring the surface chemical composition. The invention of the scanning tunneling microscope in 1982, however, truly revolutionized surface science and enabled real space observation of the electronic surface topography with atomic resolution. Meanwhile, advances in growth science and UHV-based synthesis techniques have spurred the development of novel quantum materials such as semiconductor heterostructures[4] including the quantum cascade laser,[5] and spintronic materials such as the spin valve.[6]

Of particular interest to the present study on low-dimensional superconductivity is the notion that under carefully controlled UHV growth conditions, quantum-mechanical confinement of itinerant electrons can be exploited to stabilize superconductors with lateral dimensions of the order of a few millimeters and vertical dimensions of only a few atomic layers[7,8]. Under less-well controlled growth conditions, however, metal atoms prefer to clump together instead of covering the surface evenly. The extraordinary morphological stability of these ultra-smooth quantum films, which is reminiscent of the stability of closed electron shell configuration of the noble gases, was first noticed about ten years ago[9,10]. For instance Pb, which is a type I superconductor in the bulk, has a Fermi wavelength that is almost perfectly commensurate with the atomic layer spacing

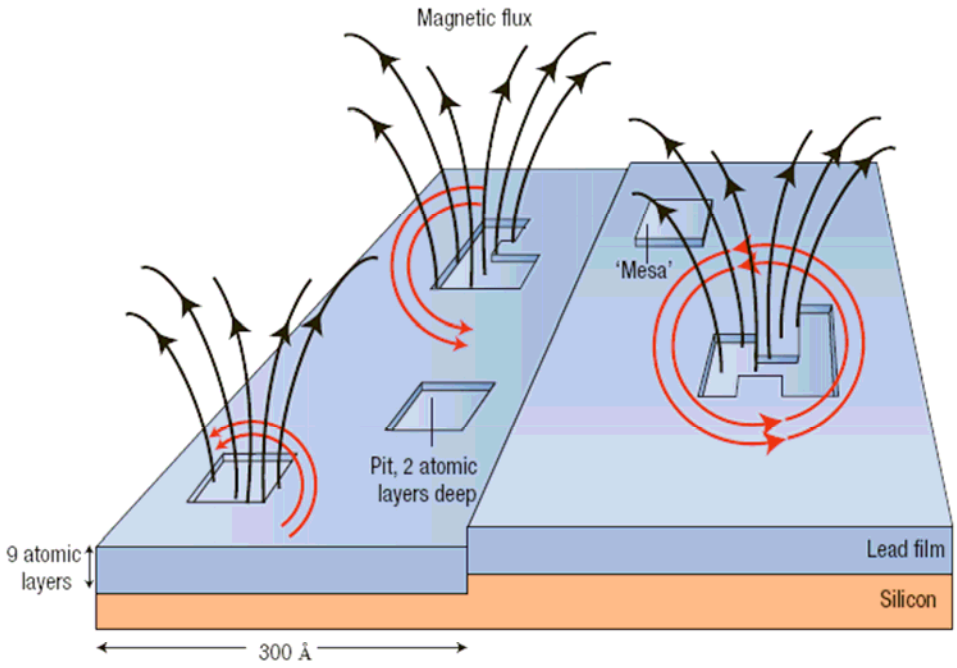

Figure 1.1: Pictorial illustration[11] of the flux pinning inside 2 ML deep quantum traps. Black arrows represent the magnetic field lines; red ones stand for supercurrents circulating vortices.

along the (111) direction. Ultrathin Pb(111) films therefore evolve, under certain kinetic growth conditions, into perfect bilayers.[7] Because of the strong quantum size effects in these Pb(111) films, the surface is atomically smooth implying specular reflection and long mean free path for the conduction electrons. This in turn greatly enhances the superconducting coherence length as compared to previous studies on granular and amorphous films.

Another consequence of the quantum size effect is the presence of two-monolayer deep depression ("blind holes") or two-monolayer tall mesas for slightly underdosed or overdosed thin films, respectively (figure 1.1).[11] The blind holes are very effective

trapping centers of the superconducting flux quanta ("vortices"), leading to an unusually strong phase coherence. For instance, a film that is only nine atom layers thick and decorated with blind holes can sustain amazingly large circulating supercurrents of about 100 milliamperes in a 3 millimeter square film; this corresponds to a supercurrent density of about 2 million amperes per cm.[2,8] On the other hand, mesas repel vortices. Artificially created structures such as the ones illustrated in figure 1.1 thus have very contrasting critical state properties. The nearly five times larger critical currents attained due to flux pinning by blind holes show how these self-assembled nanostructures can be used to control the critical state parameters.

In order to resolve the longstanding academic questions regarding the mechanisms of destruction of superconductivity in low dimensions, quality control is absolutely essential. Ideally, one would like to tweak the superconductor from the usual dirty limit to the clean limit. The answer to the question "how clean?" depends on the other length scales shown in the picture (figure 1.1). In particular, the coherence length ξ and magnetic penetration depth λ of classic low temperature superconductors are nearly mesoscopic, i.e., much larger than the atomic film thicknesses in this study. Hence, from this point of view, these thin film superconductors are definitely two dimensional. For clean limit two-dimensional superconductors, the destruction of superconducting order requires spontaneous generation of topological free defects or vortices via a Kosterlitz-Thouless (KT) process.[1] However, in dirty superconductors the KT transition is usually preempted by much stronger fluctuations driven by Coulomb interactions in disordered systems. For example, it was shown that superconductivity disappears when the normal state resistance per square *exceeds* the quantum resistance for Cooper pairs, $h/4e^2 = 6.45$

kΩ.[12] In previous studies on disordered thin films, the resistance was used as the primary control parameter for tuning superconductivity[12]. The films could only be driven into the superconducting state by increasing the deposition amount (thus lowering the sheet resistance) while the atomic-scale morphology and amount of "dirt" remained unknown. The use of atomically-smooth, single crystalline thin films with atomically precise thickness represents takes a big leap towards fundamental understanding of superconductivity in reduced dimensionality. The superior film quality achieved in our studies establishes a fundamental advance in modeling thin film superconductors: it sets the film thickness as the primary parameter instead of the sheet resistance.

1.2 Overview of the Thesis

In Chapter 2, we will review the equilibrium growth modes of ultrathin films and discuss how the kinetics of surface diffusion can be adjusted to create structures that are metastable from a thermodynamic point of view. In particular, we will learn how the quantized energy levels of the itinerant electrons inside the film can play a decisive role in determining the resulting morphology. We will introduce a reentrant bilayer-by-bilayer growth mode and show how this novel growth mode is related to the quantum size effect. After familiarizing ourselves with the experimental techniques in Chapter 3, we will revisit this issue in Chapter 4 with more detailed analyses of new experimental STM results and first principles Density Functional Theory (DFT) calculations. This part of the work reveals remarkably good agreement between experiments, free-electron theory

modeling, and DFT calculations[7], which firmly corroborates the concept of "electronic growth"[10].

In Chapter 5 we will briefly introduce the Bardeen, Cooper and Schrieffer (BCS) and Ginzburg-Landau (GL) formalisms of superconductivity. We underline the key points of the Bean critical state model on which most of our analysis will be based. Existing mechanisms for the destruction of superconductivity in low dimensionality will be reviewed.

Chapter 6 concentrates on the experimental superconductivity data from ultrathin Pb films. The data are analyzed within framework of Ginzburg-Landau theory, and employ the critical state model. We thoroughly discuss the effects of scattering and dimensionality on the equilibrium and non-equilibrium critical state properties. In particular, the superconducting critical temperature T_c and upper critical fields H_{c2} vary systematically with the layer thickness. The unusual curvature of the upper critical field near T_c indicates a very systematic deviation from GL theory with shrinking dimensionality. We will show that quantum stabilized nanostructures ("blind holes") have a striking effect on the critical current density via vortex pinning.

In Chapter 7 we will "engineer" Fermi surface of lead and create Pb-Bi quantum alloys via chemical substitution. The bismuth contents in these alloys are 11% and 20%. We will show how electron doping via Bi substitution decreases the Fermi wavelength and, consequently, changes the quantum growth mode of the films. Second, the deviations of H_{c2} from linear GL behavior near T_c become even more pronounced with increasing Bi content. We establish an empirical correlation between the reduced mean free path in the alloys and the upward curvature of H_{c2}, which suggests the intriguing

possibility of multi-subband superconductivity, analogous to the two-gap superconductivity in bulk MgB_2.[13] The multi-band structure in the Pb and Pb-Bi films arises from the quantized electronic structure.

Today's interest in superconductors almost always involves the type II materials due to their generally higher T_c and their robustness at high magnetic fields. This fact, combined with the continuing miniaturization of solid-state electronic devices, underscores the need of studying superconductivity and particularly vortex pinning in low dimensionality. This is an area where fundamental understanding of longstanding academic problems will be essential in developing tomorrow's nanoscale superconducting devices. Whereas in the past, researchers had focused on the destruction of superconductivity via disorder and/or fluctuations, we have made significant progress in separating the effects of scattering and dimensionality by focusing on superior quality thin films. We believe it should now be possible to approach the ultimate two-dimensional clean limit by exploiting quantum mechanical phenomena in thin film growth and by making judicious choices of the substrate and capping layers. Such structures not only present an ideal testing ground for theories of low-dimensional superconductivity with quantifiable parameters but may also unveil novel and unexpectedly robust critical-state properties that could be useful for superconductive nano devices.

Chapter 2

Epitaxial Thin Film Growth in the Classical and Quantum Regime

2.1 Introduction

A surface represents the termination of a three-dimensional bulk material. In traditional condensed matter physics, we usually neglect the presence of a surface because the number of surface atoms (~ 10^{15} atoms/cm^2) can be safely ignored compared to the ~ 10^{23} atoms/cm^3 of the bulk. However, in this work we will consider ultrathin films whose interior is only several atomic distances away from the surface or interface. Hence, surfaces and also interfaces are expected to play a significant role in the film properties.

Even in the thick film limit, electronic phenomena at interfaces constitute the basis for many interesting applications, such as thin film diodes and transistors. The structure of the interface furthermore determines the structure and morphology of the film. In the

remainder of this chapter, first we will summarize the theory of thin film growth and present a description of the well-established classical growth modes. Next, we will discuss the influence of the quantized electronic structure or "Quantum Size Effect" (QSE) on ultra-thin film growth.

2.2 Classical Film Growth

The growth modes of the adsorbate material on a given substrate can be characterized as a consequence of a delicate balance between adsorbate-substrate and adsorbate-adsorbate interaction energies.[14] In addition, the periodicity of the potential at the interface is an important factor in determining the structure and crystal orientation of the film. If the adsorbate-adsorbate energy is much stronger than adsorbate-substrate energy, then the lattice constant of overlayer will quickly relax to its bulk equilibrium value, which is generally incommensurate with the periodicity of the substrate. In the other extreme limit where the adsorbate-substrate energy is much larger, the overlayer will initially assume the lattice constant of the substrate. However, in this case excessive strain energy will eventually be released by forming misfit dislocations or domain walls. The grain size is of course correlated with the accumulated strain in the layer.

In the following discussion, we will briefly introduce the three classical thermodynamic growth modes named (1) Frank-van der Merwe (FM) growth (Figure 2.1.a), (2) Stranski-Krastanov (SK) growth (Figure 2.1.b) and (3) Volmer-Weber (VW) growth (Figure 2.1.c).[14,15] The FM mode refers to layer-by-layer growth. SK is characterized by initial layer-by layer growth, followed by three-dimensional islanding.

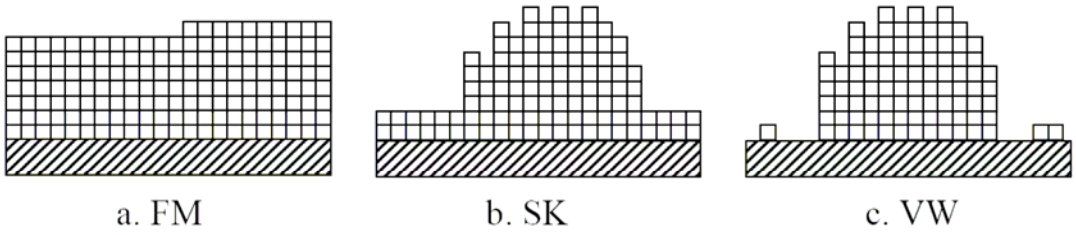

Figure 2.1: Schematic illustration of the classical growth modes. (a) Frank-van der Merwe, (b) Stranski-Krastanov, and (c) Volmer-Weber.

Finally, the VW growth mode refers to three-dimensional nucleation and growth, exposing the bare substrate in between the three dimensional clusters. These morphologies are inferred from thermodynamic equilibrium considerations. Note, however, that epitaxial growth seldom takes place under thermodynamic equilibrium conditions. Kinematic limitations toward reaching thermodynamic equilibrium imply that one cannot deduce the growth mechanism entirely from free energy considerations. We first consider the *thermodynamic criteria,* which yield the different growth modes mentioned above.

Let γ be the energy stored per unit area after cleaving a crystal. Stretching or compressing the surface after cleavage changes the surface energy and this change can be expressed via the introduction of the surface stress and strain tensors[15]. For our simple analysis it is enough to absorb these effects into the binding energy E_{ab} between the substrate and adsorbate.

Suppose we bring two semi-infinite crystals A and B into contact. E_{ab} will be the energy per unit area released after forming the contact. The interface free energy per unit area can be defined as $\gamma_i = \gamma_a + \gamma_b - E_{ab}$. First assume that crystal B grows epitaxially on

crystal A (FM growth). Secondly, consider a situation where crystal B forms clusters on A, covering a fraction x of the total surface area S (VW growth). Then, the energy difference between the FM and VW modes becomes

$$\Delta E = E_{FM} - E_{VW} = (\gamma_b + \gamma_i)S - x(\gamma_b + \gamma_i)S - (1-x)\gamma_a S . \tag{2.1}$$

It is clear that if $\Delta E > 0$ VW clustering will be favored. We can easily see that if ΔE is negative i.e.

$$\gamma_b + \gamma_i - \gamma_a \leq 0 \tag{2.2}$$

or

$$E_{ab} \geq 2\gamma_b , \tag{2.3}$$

then we obtain complete wetting. However, in order to maintain layer-by-layer growth at higher coverages, it is necessary that

$$\gamma_{b,n} + \gamma_{i,n} - \gamma_{a,n} \leq 0 . \tag{2.4}$$

is satisfied for each new layer n. So, if equation 2.3 is satisfied at the original interface but equation 2.4 is no longer satisfied after some layer n, then clusters would still form on top of a two-dimensional "wetting layer" and the SK growth mode prevails. This could happen if the adsorbate-substrate interaction is strong enough to overcome the strain energy during the first few layers but not at higher coverages.

An alternative analysis indicates that the equilibrium growth mode is determined by the chemical potential of the adsorbate species. This consideration is based on the comparison between the adsorbate's vapor pressure in the source and at the sample. This pressure differential determines the chemical potential difference $\Delta\mu = kT \ln(P_\infty / P_S)$ where P_∞ is the pressure inside the effusion cell and P_S is the vapor pressure at the

substrate. The latter is of course determined by the energetic considerations discussed in the previous paragraph. Complete wetting takes place for undersaturation ($\Delta\mu < 0$) whereas three-dimensional nucleation can take place only if $\Delta\mu > 0$, meaning supersaturation. None of these considerations include kinetic aspects related to the mobility of the adatoms. As we will see, the role of kinetics is essential in our low-temperature growth studies.

2.3 Quantum Growth

2.3.1 Introduction

As already mentioned, the above discussion governs classical film growth under thermodynamic equilibrium conditions. For a wide range of metal on semiconductor systems, the usual growth mode is known to be SK type even for lattice-matched systems like Fe on GaAs. In 1996, Smith *et al*. provided the first striking example of atomically smooth film growth of an elemental metal on a semiconductor.[9] This was accomplished by depositing Ag on GaAs in a two-step process; deposition at low temperature and subsequent annealing to room temperature. At very low temperature, atoms stick wherever they hit. Since the mobility is very low, only tiny grains are formed as opposed to smooth films or large three-dimensional clusters. Upon heating the sample to room temperature, the atoms acquired sufficient mobility to form atomically smooth films with a thickness of 15 $\mathring{A}$. If the nominal deposition amount is less than necessary to

completely cover the surface with a 15 $\mathring{A}$ thick Ag film, then the film contains large holes exposing the bare GaAs substrate. Evidently, the "underdosed" Ag film phase separates into a 15 $\mathring{A}$ thick Ag layer and bare substrate, indicating that the atomically-flat 15 $\mathring{A}$ thick Ag film is a particularly stable morphology. This unusual growth mode has been attributed to the quantum size effect.

Although this direct (STM) observation of atomically flat metal films with preferred height on semiconductors is quite recent, questions related to a possible QSE in film growth and electronic properties date back to 1976.[16]

2.3.2 Physics of the quantum size effect.

The Fermi wavelength of most metals is comparable to the lattice spacing. Therefore, for nearly-free electron metals one might expect that the electronic properties are sensitive to the film thickness, especially in the ultrathin limit. The basic idea of the QSE is derived from the "particle-in-a–box" problem of Quantum Mechanics.

Figure 2.2 illustrates the probability density of a particle trapped between two hard wall barriers. The wave function in the film plane is represented by the usual Bloch functions. The confinement in the perpendicular direction, however, introduces quantized energy levels. The wave function and energy levels for the one-dimensional quantum well with infinite potential boundaries can be easily obtained from the boundary conditions at the walls. The fitting condition is[17]

$$d = n\lambda / 2 \tag{2.5}$$

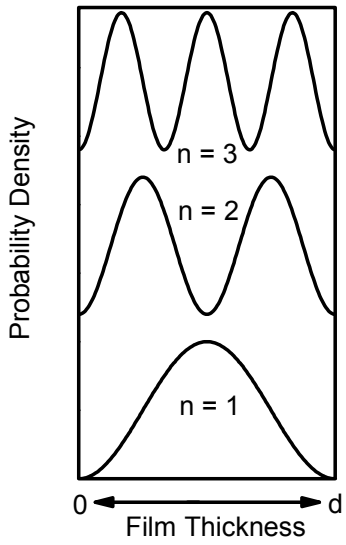

Figure. 2.2: Probability densities of the lowest-lying energy levels inside a 1D quantum well.

where n is an integer; d is the thickness of the film and lambda is the wavelength. The eigenstates and corresponding energy levels are[17]

$$\Psi(z) \propto \sin\frac{n\pi z}{d} \tag{2.6}$$

and

$$E_n = \frac{n^2\pi^2\hbar^2}{2md^2}. \tag{2.7}$$

The presence of such standing waves raises the natural question to what extent the electronic and structural properties of ultra-thin epitaxial overlayers are affected by the QSE. Pioneering experiments of Jaklevik and Lambe indicated QSE's in the tunneling spectra of metallic thin films on various substrate.[18] Around the same time, Schulte theoretically explored QSE in freestanding jellium slabs.[16] In Schulte's work, all the electronic properties like electron densities, potentials and work functions were

calculated self-consistently within Density Functional Theory, and were shown to oscillate with a period of one half Fermi wavelength. Schulte's oscillations are a direct consequence of the fitting condition (Equation 2.5), meaning that whenever the thickness increases up to a multiple of one-half Fermi wavelength, a new quantum well subband drops below the Fermi energy, giving rise to the observed oscillations. In practice, the film thickness may not be increased by precisely one-half Fermi wavelength because the atomic layer spacing and Fermi wavelength are generally incommensurate. Feibelman subsequently included a crystal lattice and calculated the work function and surface energy of freestanding Al(111) and Mg(0001) slabs using DFT.[19] He showed that the theoretical work function of Al(111) slabs sample Schulte's jellium calculations[16] quite nicely for integer layer thickness. Following these initial considerations many experiments have been performed to observe QSE in thin films.

The existence of the QWS sketched above gives rise to distinct features in photoemission spectroscopy (PES) and in Scanning Tunneling Spectroscopy (STS). PES experiments of the QSE in thin metal films have been reviewed by T.-C. Chiang[20]. Experiments by Su *et al.*[21] and by Altfeder *et al.*[22] nicely demonstrated the use of STS in verifying basic predictions from the particle-in-a-box model. These researchers performed STS measurements on individual Pb islands *on top of* a 2D Pb wetting layer on Si(111) and determined the energy levels of the quantum well states. Using equation (2.7) one easily determines the level spacing between the highest occupied quantum state and lowest unoccupied quantum state:

$$\Delta E = E_n - E_{n-1}; \qquad E_n \approx E_F. \tag{2.8}$$

This yields

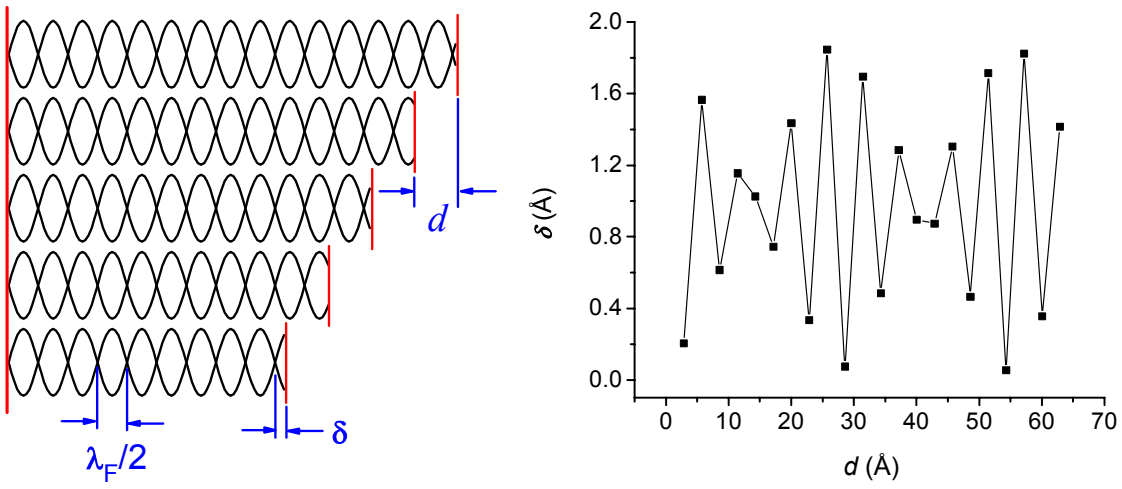

Figure 2.3: An illustration showing the misfit between the wave function and film thicknesses.

$$\Delta E \approx \frac{\hbar^2}{2m}[k_F^2 - (k_F - \frac{\pi}{d})^2] = v_F \hbar \frac{\pi}{d}. \tag{2.9}$$

Hence, a plot of $1/\Delta E$ versus island height d should produce a straight line. The slope indeed reproduced the correct Fermi velocity v_F of bulk Pb.[21] However, extrapolation of this line to the thickness axis produced an offset of d_0 = –3 ML which was attributed to the presence of a 3 ML thick wetting layer. Another aspect that emerged from both studies is the clear oscillations in the electronic structure as a function of layer thickness, indicating a 2 ML periodicity. Electron fringes observed in the filled state images of reference 22 and oscillations of the measured island heights in reference 21 seem to be related to the accidental near-commensurateness of Pb lattice constant and Fermi wavelength, as will be shown below.

In figure 2.3, δ represents the misfit between the film thickness and standing wave pattern with wavelength $\lambda_F/2$ i.e. $\delta = nd - m\lambda_F/2$. Possible relaxations of lattice and

slight readjustments of the Fermi energy are ignored in this simple sketch. Moreover, possible phase shifts (other than the usual 180 degree phase shift at hard wall barriers) due to charge spilling at the film boundaries are also neglected. By plotting the misfits as shown in figure 2.3 we observe 2 ML oscillations over ~ 9 ML intervals. As it turns out, these are precisely the same oscillations that have been observed in the electronic structure and thin film stability. The latter can be attributed to oscillations in the total charge density, which also have a 2 k_F periodicity.[7]

PES studies by Mans *et al.*[23] follow a more careful treatment of the problem, taking into account the possible phase shifts at the surface and interface. To incorporate the phase shifts into the picture, the simple fitting condition in equation 2.5 should be replaced by the corresponding expression of the Bohr-Sommerfeld phase accumulation model

$$2k(E)d + \Phi_B(E) + \Phi_C(E) = 2\pi n \tag{2.10}$$

where $\Phi_B(E)$ and $\Phi_C(E)$ are the phase shifts at the vacuum and substrate interfaces. Within the WKB approximation it can be shown[23] that Φ only depends on energy. So, if we pick two QWS at the same energy from the PES spectra recorded at different thicknesses we easily obtain the perpendicular momentum k at that particular energy using:

$$k(E) = \pi(n_2 - n_1)/(d_2 - d_1)\,. \tag{2.11}$$

Using this procedure, one can in principle obtain the full perpendicular momentum dispersion k(E), which in turn can be used to calculate the total phase shift via equation 2.10. It is interesting to note that the qualitative outcome drawn from this simple 1-D model does not change much after integrating over k// of the subbands.[24]

QSE have also been revealed in thin film growth experiments. The first report of QSE on ultrathin metal film growth dates back to 1989 when Hinch and coworkers[25] performed helium atom scattering (HAS) experiments of Pb films grown on Pb(111) and on Cu(111). In the case of Pb on Pb(111), specular beam intensity measurements indicated classical layer-by-layer growth as expected. However, the specular beam intensity for Pb on Cu(111) exhibited quasi bi-layer oscillations, reminiscent of the oscillations in the misfit function shown in figure 2.3. Notice that figure 2.3 is slightly different from the misfit function in reference 25 because we use a somewhat larger λ_F ($3.95\,\text{Å}$ vs. $3.66\,\text{Å}$). Hinch *et al*. interpreted their result in terms of an unusual quantum growth mode, following Schulte's[16] and Feibelman's[19] initial ideas. Later it was argued[26] that the bilayer oscillations in the HAS are due to bi-layer variations in the charge spilling at the surface, instead of a bilayer growth mode. More recent studies, however, supplied ample evidence for a QSE on thin film growth.

The first example, namely the observation of atomically smooth Ag films on GaAs, has already been mentioned[9]. In 2000, Tringides and coworkers reported that low temperature (185 K) deposition of Pb on Si (111)-(7x7) results in the formation of flat-top islands with steep-edges and a surprisingly uniform height distribution centered at 7 ML.[27] Subsequent studies of this system provided more detailed information on the kinetics aspects of growth.[28] In this reference, the existence of competing 4 or 5 ML, 7 ML and 9 ML island heights was summarized in a "kinetic phase diagram" for nominal coverages up to 10 ML and temperatures between 120 to 250 K. The general trend is that in this quantum growth regime, flat-topped islands are always formed on top of a 2D wetting layer and that the island height increases with increasing coverage and increasing

temperature. If the temperature is too low, the resulting films are continuous but rough. This is classical non-equilibrium layer-by-layer growth. If the deposition temperature is too high, then the adsorbate atoms ball up into thermodynamically favored 3D islands (SK growth). The quantum growth regime, leading to atomically smooth films, is located in between the low temperature layer-by-layer regime and the high temperature SK regime.

To investigate the role of the metal/semiconductor interface, similar studies were conducted on Si(111)-Pb($\sqrt{3}\times\sqrt{3}$).[29] This time the minimum preferred height was 5 ML instead of 7 ML. This change was attributed to the different potential barrier or Schottky barrier height at the interface, leading to a different amount of charge spilling at the interface. Indeed, the role of the substrate on the total free energy of the film had been considered in an earlier work[10], which elucidated the effects of quantum confinement, charge spilling, and Friedel oscillations.

In the jellium model,[14] where a uniform, positive background replaces the ion cores, the electron density does not follow the step function behavior of the positive charge background. Instead, the screening response of the free electron gas to this step potential produces oscillations in the electron density, which decay into the bulk of the film. The oscillations are called Friedel oscillations and have a wavelength equal to π / k_F where $k_F = (3\pi^2 \overline{n})^{1/3}$ in the free electron gas model. Whether or not Friedel oscillations persist in the presence of an atomic configuration is not a priori clear. However, if this Friedel wavelength is commensurate with the atomic layer spacing, then one could imagine persistent density oscillations inside the film, emanating from both interfaces. These 2 k_F

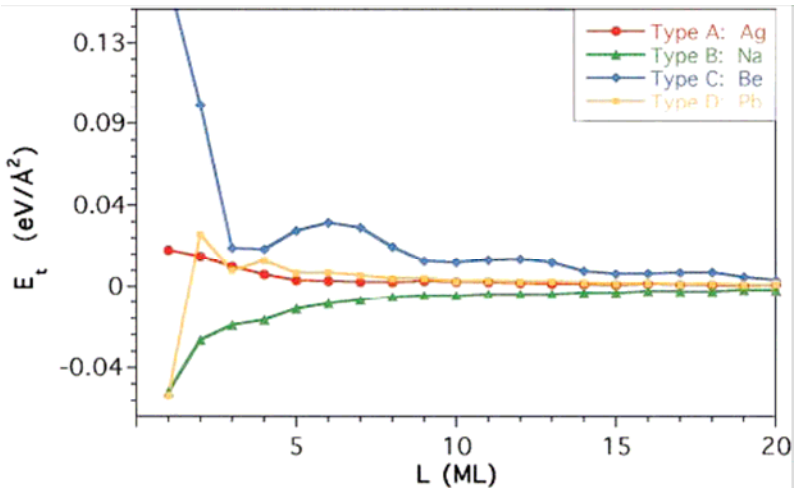

Figure 2.4: Total film energies reproduced from reference 10 for different types of metals. An exemplary metal for each type is pronounced.

oscillations in the total charge density are expected to affect the thickness-dependent stability via Coulomb potential.

In reference[10], a total film energy $E_t = E_0 - E_c$ is introduced where E_0 is total electronic energy from free electron model after subtracting a term linear in film thickness and E_c is the stored "capacitor" energy at the interface due to charge spilling. The thermodynamic stability condition for a particular film thickness L is then given by $\partial^2 E_t / \partial L^2 > 0$. The competition between the film energy and capacitor energy determines the growth mode of the metal layers. Accordingly, it can be shown that Ag on GaAs should be stable above 5 ML, which is reasonably close to experimental finding[9]. In the case of Pb, 2 ML damped oscillations are evident which have been attributed to Friedel oscillations. These results are summarized in figure 2.4 for different types of metals.

The above calculations are valuable for giving physical insight, although the results are not very accurate. In recent years, powerful computers have enabled accurate total

energy calculations from first principles. One major difficulty with these DFT calculations is to choose a unit cell that is large enough to accurately reproduce the atomic relaxations of the true ground state while keeping the CPU time within reasonable limits. Note that for 2D systems, one cannot employ the Bloch theorem in the direction perpendicular to the surface or thin film. A commonly applied trick for 2D systems is to create an artificial periodic arrangement of 2D slabs of material separated by vacuum gaps. It still is a very difficult task to include the substrate in such slab calculations because the substrate and overlayer are generally incommensurate and hence, there is no periodicity along the parallel direction either.

Researchers have tried to mimic the role of the substrate with a jellium[30] or with an artificially strained substrate that matches the lattice constant of the film.[31] In this thesis, we employ the accidental commensurateness between Pb(111) layers and the Ge(111)-($\sqrt{3}\times\sqrt{3}$) reconstructed surface to obtain more accurate results.[7] We will leave the details of this nice system for chapter 4 and close this chapter by briefly mentioning the DFT calculations on freestanding Pb slabs in reference.[32] Here, the calculated surface energy and work function oscillate with a quasi bi-layer periodicity, exactly as one would expect from the simple fitting arguments demonstrated in figure 2.3. However, we will show both experimentally and theoretically that the substrate does play an important role in determining the thin film stability. Finally, it should be noted that in spite of the accuracy of many DFT calculations, they do not easily convey the underlying physics. In this regard, free electron model calculations will remain an important tool for analyzing these physics principles.

Chapter 3

Experimental Methods

3.1 Thin Film Growth in Ultrahigh Vacuum

Experimental studies of surface phenomena require special techniques. The cleanliness of a surface depends on its reactivity, the residual gases in the atmosphere surrounding it, and the pressure. According to kinetic theory of gases, if we assume that every single molecule hitting a surface sticks at the point of collision, then it takes only one second to cover the surface with 1 atomic layer (ML) of atoms at 10^{-6} mbar pressure. So, an experiment, which takes typically many hours or a day, must be carried out at pressures of 10^{-10} mbar or better. This extremely low pressure is typically referred to as Ultra High Vacuum (UHV). It requires use of special materials and pumping techniques. All characterization and measurement tools attached to UHV chamber also must be UHV compatible. In the following we will briefly summarize the basic operating principles of the equipment used throughout this study and point out some subtleties one must be careful about, for otherwise the measurements could produce spurious results.

UHV equipment roughly serves two purposes: in-situ sample preparation and characterization. Surface preparation involves surface cleaning via e.g. sputtering and annealing or quick sample flashing. For thin film growth, we employ Molecular Beam Epitaxy (MBE). MBE refers to the in-situ growth of well-defined epitaxial layers on clean crystalline surfaces through precisely controlled thermal evaporation. Typical deposition rates are of the order of 1-10 ML per minute. The calibration procedure for determining the deposition rate will be described below.

3.2 In-situ Characterization Techniques

3.2.1.a X-Ray Photoelectron Spectroscopy

Photoemission Spectroscopy (PES) is a surface sensitive method used to determine the surface chemical composition.[33] This technique is based on the photoelectric effect. Photons are used to excite electrons inside the sample to energies well above the vacuum level. Electrons escaping into the vacuum are dispersed and counted.

The kinetic energies of the photoelectrons can be correlated with their initial binding energy E_b via

$$E_{kin} = \hbar\omega - E_b - \phi \tag{3.1}$$

where $\hbar\omega$ is the photon energy and ϕ the work function (see figure 3.1). By plotting the number of photoelectrons versus their binding energy, we obtain a photoelectron spectrum, which contains very useful information about the chemical and electronic structure of the sample.

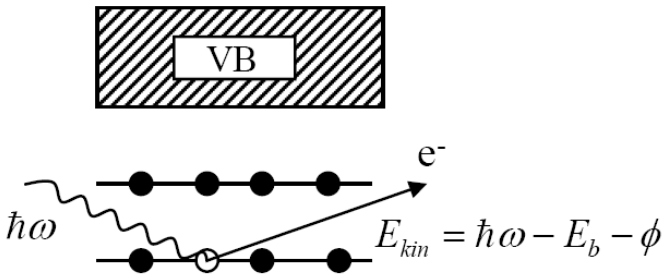

Figure 3.1: Simple illustration of the photoemission process.

Highly energetic X-ray photons are used mainly to probe the core levels of the constituting elements (XPS), whereas ultraviolet light is more suitable to study the valence electronic structure (UPS). Although the light penetrates deep into the sample, the outgoing photoelectrons have a short inelastic mean free path which is typically of the order of 5-50 Å. Hence, PES is very surface sensitive. It is this property that makes PES a very useful tool for calibrating the deposition rate of overlayers as explained in the next section.

The XPS system in our chamber consists of an X-ray source, a monochromator, and an electron energy analyzer. X-rays are produced by bombarding an Al target with electrons. The operating principle of the monochromator is based on Bragg diffraction. A quartz crystal is bent to follow the curvature of a Rowland circle of 500 mm radius. This configuration selects Al $K\alpha_{1,2}$ radiation with $\lambda = 8.34$ Å (1486.7 eV) and a $FWHM \approx 0.2$ eV.

The electron kinetic energies are measured with a hemispherical analyzer with a 7-channel detector (figure3.2). An applied electric field between two concentric metallic

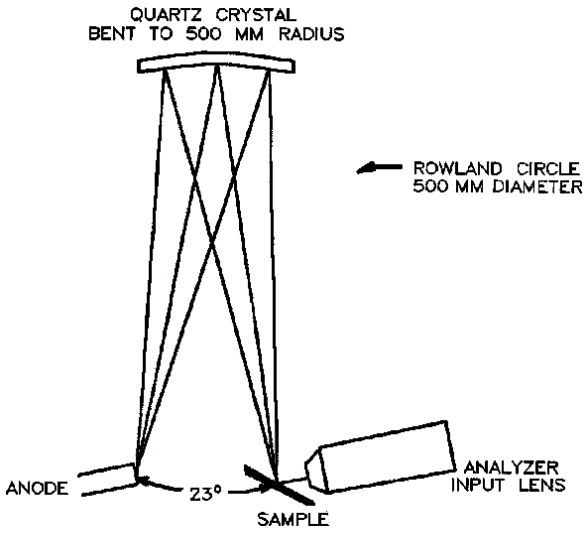

Figure 3.2: Schematics shows the layout of the X-Ray source, monochromator, sample, and electron energy analyzer input lens.

hemispheres deflects the electrons passing through them. Only electrons with a specific (i.e., selected) kinetic energy can follow the curvature of the hemispheres and reach the detector. Electrons with *slightly* higher or lower energy follow a trajectory with a slightly larger or smaller radius of curvature, respectively, and may still reach the exit of the analyzer.

These electrons can also be detected by employing 7 counters positioned at slightly different locations at the exit. All other electrons are filtered out. A full spectrum is obtained by scanning the voltage between the hemispheres, thus selecting the kinetic energies, and counting the electrons for each channel. The core level binding energies in XPS are element specific, which makes XPS a most useful tool for surface chemical analysis. It can also be used to calibrate deposition rates in hetero-epitaxial growth (A on B), as will be shown in the next section.

3.2.1.b XPS Applications

To calibrate the Pb and Bi deposition rates in our experiment, we monitored the evolution of the Pb and Bi core level intensity during the formation of two-dimensional Pb phases and Bi phases on Ge(111) and Si(111), respectively, whose structure and coverage are known precisely. It is well known[34,35] that Pb forms so-called α and β phases on Ge(111) at a coverage of 1/3 and 4/3 ML, respectively. Here, 1 ML corresponds to 1 Pb per Ge atom in the Ge(111) plane, or 7.2×10^{14} Pb atoms/cm^2. Both surface phases exhibit a $(\sqrt{3} \times \sqrt{3})R30^\circ$ periodicity with respect to the underlying (111) substrate. Room temperature deposition of Pb on Ge(111) always produces the α and β phases. These phases also exist on Si(111) but a different kinetic pathway must be followed to break the Si bonds of the clean Si(111)7x7 reconstruction before forming the α and β phases, which requires heating.

Assume that the growth of some material on a substrate follows the Stranski-Krastanov (SK) mode and that we are monitoring the XPS intensity of some core level of the deposited material during the growth process. Initially, the XPS intensity will be proportional to the number of atoms in the first layer, hence the signal should increase linearly until the 2D adlayer is completed. The XPS intensity will increase further upon deposition of a second or third layer but because the intensity from the buried layers is attenuated by a factor $\propto \exp(-d/\lambda)$ (where d is the film thickness and λ the mean free

path of the photoelectron), the XPS uptake signal will not increase as fast, resulting in a clear kink in the intensity versus coverage diagram. Smaller and smaller rates of increase would follow during the growth of 2nd, 3rd, etc. layer. Finally, one would see very little increase after 3-D nucleation sets in. In particular, if 3D islands are formed on a single adlayer, then the XPS uptake would show a very clear kink. Our calibration procedure is based on the fact that 3D islands are formed on top of the β-phase wetting layer. The location of the kink on Ge(111) thus corresponds to exactly 4/3 ML of Pb.

To guarantee SK growth and formation of well-defined α and β phases, one needs to keep the substrate at some elevated temperature. As we mentioned above, Pb on Si(111)(7x7) requires considerably higher temperature compared to Ge(111) to form these phases. Considering the several hours time span needed to perform the calibration experiment, one must consider the issue of thermal desorption of Pb, which is why we have chosen to use Ge(111) for our calibration studies. Figure 3.3a shows a typical uptake curve taken at ~ 200° C. The kink in figure 3.3a corresponds to 4/3 ML phase in terms of Ge(111) plane which is very closely to the atomic density in the (111) plane of bulk Pb. Indeed, this deposition rate is independently verified using the Rutherford Backscattering Spectrometry (RBS) technique.

Bi also forms a $(\sqrt{3}\times\sqrt{3})R30^{\circ}$ structure on Si(111), however, this system is different from the Pb/Ge(111) system discussed above because two distinct phases occur at 1/3 ML and 1.0 ML[36]. We calibrated the Bi deposition rate by depositing Bi on Si(111) again around 200° C. Again, the sharp kink in figure 3.3b corresponds to the completion of a 2D wetting layer, which now corresponds to 1 Bi atom per Si atom in the (111) plane, or

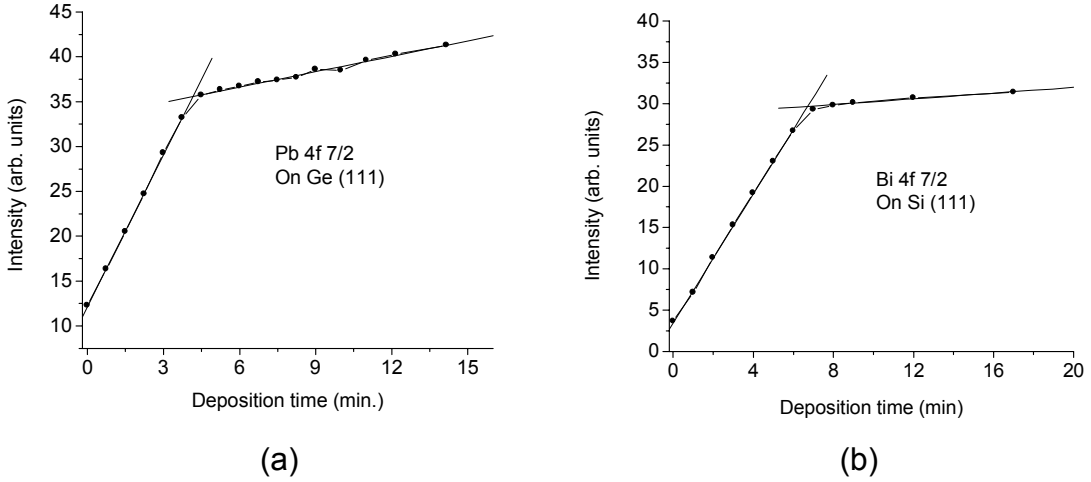

Figure 3.3, a and b: Two example calibration curves for Pb and Bi. The kinks correspond to completion of adlayers.

7.8×10^{14} Bi atoms/cm^2. This interpretation has been successfully verified under the STM using the newly discovered crystal structures of Bi at ultra low coverages.[37]

3.2.2.a Low Energy Electron Diffraction (LEED)

The termination of the bulk periodicity at the surface typically results in a change of crystal structure and electronic structure near the surface. A reorientation of the broken bonds at the surface induces surface reconstructions, which usually exhibit different in-plane periodicities compared to the periodicity of the corresponding crystal planes in the bulk. Low Energy Electron Diffraction (LEED)[33] is a very useful tool in surface science to determine the surface reconstruction because low energy electrons cannot propagate deep into the material: LEED is a surface sensitive probe. In the case of ultrathin films on well-defined substrates, LEED also provides information about the crystal structure of the film.

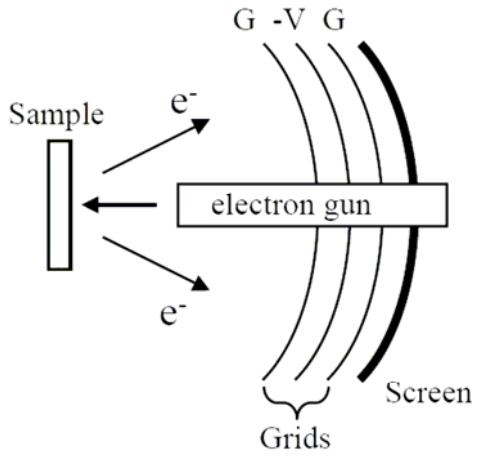

Figure 3.4: LEED Schematics.

Surface reconstructions may be altered and controlled by depositing a sub-monolayer amount of another element, followed by heat treatment. The heat treatment is usually necessary to break the bonds of the clean reconstructed surface and to facilitate the in-plane ordering of the adsorbate atoms. LEED can reveal the presence of new surface phases, which has also been very useful in identifying the $(\sqrt{3}\times\sqrt{3})R30^{\circ}$ phases in our calibration studies.

The LEED image is a diffraction pattern or the Fourier transform of the 2D surface structure. The LEED apparatus consists of an electron gun and a phosphor screen (see figure 3.4). The electron gun emits electrons with beam energies typically ranging from 10-200 eV and a spot size of about 1 mm. The electron beam is scattered off the surface and is made visible on a phosphor screen. The LEED pattern is a wave-like interference pattern of electrons that are backscattered elastically. In this process, the periodic surface structure acts as an atomic scale grating. Elastically scattered electrons only constitute a small fraction of the total number of backscattered electrons. Inelastic electrons are

filtered out by a sequence of metal grids placed in front of the screen. In the simplest setup, there are three grids. The electric field between the first and second grids (counting from the left) decelerates the inelastic electrons, so that only elastically scattered electrons reach the screen.

The *k* vector of an electron can easily be determined from the relation $E = \hbar^2 k^2 / 2m$. The diffraction pattern can be interpreted qualitatively using the Ewald sphere construction used in 3-D crystallography. One needs the 2-D counterparts of the reciprocal lattice vectors, defined via[38]

$$\mathbf{a}_i \cdot \mathbf{b}_j = 2\pi\delta_{ij} \tag{3.2}$$

where $\mathbf{a}_i$ and $\mathbf{b}_i$ denote the unit cell vectors in real space and reciprocal space, respectively. Note that $\mathbf{b}_3$ is a reciprocal lattice vector perpendicular to the surface. If only scattering from the surface layer is considered, the necessary condition for constructive interference is given by

$$\mathbf{d} \cdot \mathbf{q} = 2\pi \times \text{integer}, \qquad \mathbf{q} = \mathbf{k}' - \mathbf{k}, \qquad |\mathbf{k}| = |\mathbf{k}'| \tag{3.3}$$

for all vectors $\mathbf{d}$ joining the lattice points in the surface plane. $\mathbf{k}$ and $\mathbf{k}'$ are the wave vectors of the incoming and backscattered electron beam. The Ewald sphere construction is available in many textbooks[33] and we will not go into details. In order to obtain the atomic positions, one must perform a quantitative analysis of the LEED intensities as a function of beam energy. However, quantitative LEED analyses are very complex and must take into account e.g., multiple scattering, atomic form factors, and scattering phase shifts. However, a visual inspection of the LEED pattern is usually sufficient for obtaining information about the in-plane periodicity of the surface structure.

3.2.2.b LEED Applications

In this study, LEED was used to verify the existence of the various surface phases. LEED is superior to STM (see below) in the sense that it samples macroscopic sample dimensions. At the same time, due to its limited spatial resolution, it is often too forgiving. For instance, samples with clustered contaminants still produce sharp LEED pattern because one can still find areas that are atomically clean and scatter in phase. Most of our studies, however, required surfaces free of all sorts of contamination. Most quantum growth experiments required atomic level smoothness over mesoscopic dimensions while macroscopic cleanliness was desired for the superconductivity experiments in order to achieve macroscopic electrical connectivity. Therefore, in our experiments STM has been the decisive tool for judging the quality of the substrate.

During the quantum growth experiments, we used LEED to verify the structure and lattice constant of ultrathin Pb films grown on Si(111)-7x7, Ge(111)-2x8 and their corresponding α and β phases. We also verified that the $Pb_{89}Bi_{11}$ random alloy films grown on Si(111)-7x7 assume the Pb(111) crystal orientation and also determined their in-plane lattice constant. A special procedure was employed to measure lattice constant with LEED. In principle, one should know the beam energy and distance between sample and LEED screen very precisely. The beam energy can be determined with great precision; however, physical limitations of our UHV system do not allow for a very precise measurement of the sample-to-screen distance. Moreover, due to some small distortion of the LEED pattern developed on the spherical screen geometry and due small

misalignment, the in-plane k values also cannot be determined precisely. In order to overcome these difficulties, we measured the lattice constant of the films relative to the known value of the substrate. To that end, we first recorded the LEED pattern of the thin film and then flashed the sample to high temperature to remove the film without changing the sample position. The comparison between the LEED images of the substrate and film provides lattice constant of the film within a few percent error.

3.2.3.a Scanning Tunneling Microscopy

It can be shown that the LEED pattern represents the Fourier transform of the periodic surface structure. Scanning Tunneling Microscopy (STM)[39], on the other hand, probes the *electron density* at the surface and yields the real-space topography of the surface electronic structure. STM may be used to obtain atomic resolution images or to observe mesoscopic structures and their evolution during thin film growth. In some cases X-ray reflection and Spot Profile Analysis LEED (SPALEED) can be used to obtain statistical information about mesoscopic structures, however, the results are not as direct and as reliable as STM data. Since STM is a tunneling probe, it is also very useful to study the electronic structure of surfaces.

Two of the STM operating modes are most common: Constant current mode and constant height mode. Here we will consider only the constant current mode. A simple STM schematics is shown in figure 3.5. The tip-sample distance (s) can be adjusted by applying a relatively high voltage (U_Z) to a piezoelectric device. If the tip-sample distance is within the range of quantum mechanical tunneling, then one can control the

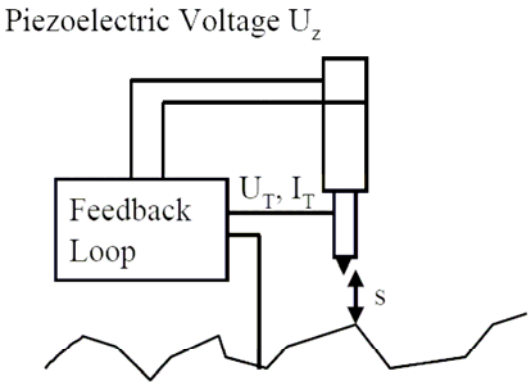

Figure. 3.5: STM Schematics in constant current mode. (See text)

"tunneling current" (I_T) by applying a voltage U_T between the tip and the sample. The tip can also be moved parallel to the surface by applying voltages U_X and U_Y to another piezoelectric element (not shown in the figure). The electronic topography of the surface is probed by measuring the change in the distance s while scanning U_X and U_Y. A feedback loop is implemented so as to maintain a constant tunneling current by constantly readjusting the distance s via U_Z. So, one can obtain the topographic image of the surface (actually an image of the local density of states) by storing U_Z as a function of x and y.

An essential aspect of the STM is that the tunneling current depends exponentially on the tip-sample distance. To solve the simplest 1-D barrier-tunneling problem, two approaches are possible. The first one is the time-independent wave-matching procedure well known from elementary quantum mechanics. The other one is a time dependent treatment (Bardeen's transfer Hamiltonian approach).[39] In the latter approach, the wave function of the tip (sample) is supposed to decay not only outside the tip (sample) but also inside the sample (tip). Then, using perturbation theory, a tunneling matrix element

M for an electron can be calculated between the *unperturbed* states of the tip and the sample. For the 3-D geometry of tip and sample the wave-matching method is impossible to solve. Instead, Bardeen's transfer Hamiltonian can be used for an *assumed* geometry and electronic structure of the tip. Within this formalism the tunneling current *I* is given by[39]

$$I = \frac{2\pi e}{\hbar}\sum_{\mu,\nu}\{f(E_\mu)[1-f(E_\nu+eU)]-f(E_\nu+eU)[1-f(E_\mu)]\} \cdot |M_{\mu\nu}|^2\ \delta(E_\nu - E_\mu). \tag{3.4}$$

where *f(E)* is the Fermi function, *U* is the applied bias voltage, $M_{\mu\nu}$ is the tunneling matrix element between the unperturbed electronic states Ψ_μ of the tip and Ψ_ν of the sample surface, and E_μ (E_ν) is the energy of the state Ψ_μ (Ψ_ν) in the absence of tunneling. The challenge is to calculate the matrix element *M* given by Bardeen as

$$M_{\mu\nu} = \frac{-\hbar^2}{2m}\int d\boldsymbol{S}\cdot(\Psi_\mu^*\nabla\Psi_\nu - \Psi_\nu\nabla\Psi_\mu^*) \tag{3.5}$$

where the integral has to be evaluated over any surface lying entirely within the vacuum barrier region between the tip and the sample. Since the atomic structure of the tip is generally not known, some assumptions must be made. For the simplest model one can imagine a tip with a spherical symmetry at the apex. It has been shown that for *s*-electrons in the tip (i.e., neglecting the $l \neq 0$ angular momentum states) the tunneling current becomes

$$I \propto \exp(-2\chi s) \tag{3.6}$$

where $\chi = (2m\phi)/\hbar$ is the decay rate within the effective local potential ϕ. Generally this expression is not valid at high bias voltage and for tip wave functions with non-zero

angular momentum. Still this expression implies the exponential dependence of tunneling current, which makes the STM operation possible.

3.2.3.b STM Applications

During most of our studies, we have used variable temperature STM to check the substrate quality and the morphological evolution of the metallic thin films. The $(\sqrt{3}\times\sqrt{3})R30^\circ$ α and β phases has also been identified with atomic resolution STM. In the case of Ge, the α and β phases could be distinguished very clearly with STM because only the α phase undergoes an easily recognizable charge density wave transition (CDW) at low temperatures[34]. This distinction is much harder in LEED because both phases produce a $(\sqrt{3}\times\sqrt{3})R30^\circ$ diffraction pattern.

We already emphasized the role of thermally activated surface diffusion in thin film growth. Hence, before starting the experiments, we calibrated the sample temperature at the STM stage, as well as at the manipulator stage where the deposition experiment took place. For this purpose, a non-standard Chromel/gold-iron thermocouple attached to sample was used for its excellent sensitivity at low temperatures. The sensitivity of thermocouple was checked by submersing it into liquid nitrogen and liquid helium, producing excellent results.

Atomic resolution of STM is accomplished by tunneling through a single atom at the apex of the STM tip. The tip shape is usually reconditioned by applying a high bias voltage and large tunneling currents. Usually, our scans at mesoscopic scale do not require atomic resolution. However, the STM tip must be reconditioned regularly in order

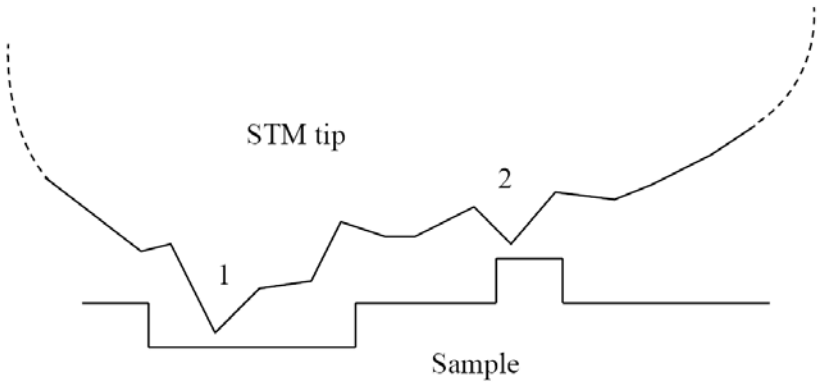

Figure. 3.6: Illustration of a common STM tip problem. (See text)

to obtain "clean" images. Although we have never imaged an STM tip, our experience indicates that the tip condition can be as bad as shown in figure 3.6, especially if the tip had crashed into the sample and was still being used afterwards (usually they are). The lateral size of this image could be several hundreds of nanometers and the vertical scale may be a few nanometers. Fortunately, one can still achieve atomic resolution with such a tip via the apex labeled 1. However, while scanning the "hole" under apex 1, apex 2 will project a ghost "island" image onto the hole. In the final image, the island shown under apex 2 will be duplicated. This very common experience can be identified sometimes from the unrealistic height profiles across the ghost images, indicating for instance island heights corresponding to a half atom.

Closed metal films often exhibit small pinholes exposing the substrate. In such cases, depth measurements become even more tricky. For example, holes in one image may all measure to be 4-5 ML deep although they are actually 9 ML deep. The recommended procedure in such cases is to change the image contrast such that the features at the bottom of the holes become visible while the imaging brightness of all other features is

fully saturated. A depth measurement will only be reliable if all tunneling electrons pass through a single apex, meaning that *all* holes must be free of ghost images. Even if the second apex is scanning a smooth area, the bottom will appear clean but its measured depth would still be wrong.

3.3 Ex-situ Measurement Techniques

3.3.1 Superconducting Quantum Interference Device (SQUID)

The basic principle of SQUID[40] magnetometry (figure 3.7) goes back to Josephson's early prediction which states that a zero voltage supercurrent should flow between two superconducting electrodes that are separated by a thin insulating barrier. This is usually referred to as the dc Josephson effect. The current is given by[40]

$$I_s = I_c \sin \Delta\varphi \tag{3.7}$$

where I_c is the maximum supercurrent that the junction can support and $\Delta\varphi$ is the phase

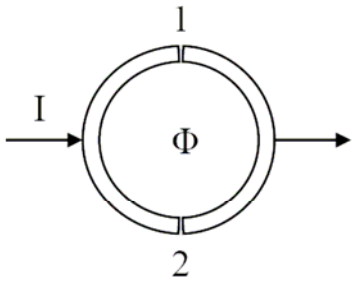

Figure 3.7: Schematics showing two-junction SQUID loop.

difference between the superconducting order parameters on either side of the junction.

Because the phase is single valued, one can show that the phase differences γ_1 and γ_2 across the junctions 1 and 2 respectively must satisfy

$$\gamma_1 - \gamma_2 = 2\pi\Phi / \Phi_0 \pmod{2\pi} \tag{3.8}$$

where Φ is the magnetic flux inside the loop and $\Phi_0 = hc/2e$ is the flux quantum. It can furthermore be shown that the maximum value of the current *I* should be

$$I_m = 2I_c \,|\cos(\pi\Phi / \Phi_0)|. \tag{3.9}$$

This relation indicates that the flux changes through the loop can be measured down to very small fractions of Φ_0.

We have used radio frequency (rf) SQUID in our study. An rf SQUID employs a single junction instead of two as shown in figure 3.8 where J indicates the junction.

By shorting one of the junctions, it has become necessary to monitor the signal in the rf range. Consider the current passing through the junction J as a superposition of the two separate currents flowing through the loops to the left and right of the junction. We will loosely refer to these loops as loop 1 and loop 2. For this geometry, the phase difference

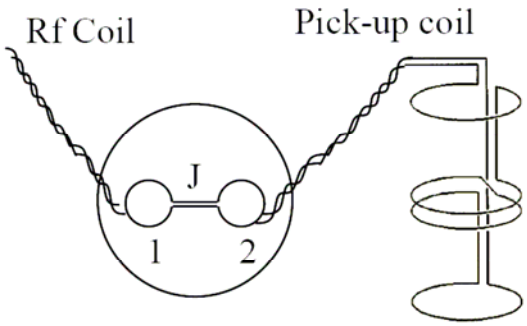

Figure 3.8: Using a single Josephson junction in rf SQUID.

equation is modified to

$$\gamma = 2\pi\Phi / \Phi_0 \pmod{2\pi}. \tag{3.10}$$

Loop 2 contains a solenoid that is coupled to the pick-up coils. A magnetized sample passes through the solenoid and produces an induction signal inside the pick-up coils, which is also inside loop 2. This part of the circuit is called the flux transformer. Another solenoid passes through loop 1 and forms an LC circuit via a capacitor. The rf signal supplied to this LC circuit will be subjected to losses whose amount will vary periodically with the DC flux enclosed by the loop with a period of Φ_0. Hence, the Q factor of the circuit and the rf voltage drop across the circuit will show the same response. Instead of following these changes, our system generates a DC feedback current in circuit 1 so as to oppose the flux changes, meaning that the SQUID magnetometer operates as a "flux-locked loop." The instrument used was a model MPMS-XL manufactured by Quantum Design Inc.

3.3.2 SQUID Measurement procedures

Our SQUID magnetometer has both AC and DC measurement capabilities. The DC signal solely depends on the flux change induced by the *moving* sample inside the pick-up coil. The sample may have a permanent magnetization or it may be magnetized by applying a DC magnetic field (up to 7 Tesla). This DC field is generated by a superconducting magnet surrounding the pick-up coil (not shown in the figure). To improve the sensitivity (down to 10^{-8} emu), one typically resorts to AC measurements. In this case, the sample remains stationary in the middle of the pick-up coil while a purely

AC or AC+DC field is applied. The maximum AC amplitude is 5 G and the frequency can go up to 1100 Hz. Before each AC measurement, the sample is parked outside the pick-up coil so that the induced signal due to the drift of the applied magnetic field is read and recorded first. This is a nulling procedure, which is needed in order to extract the sample's response after the actual measurement is carried out. The final reading of an AC susceptibility measurement is related to the differential susceptibility of the sample, which is defined as $\chi = dm/dH$. The AC signal contains an in-phase and out-of-phase component, which are proportional to the real and imaginary part of the complex magnetization $m = m' + im''$. Here m' is the in-phase real component and m'' is the out-of-phase, imaginary lossy component of the magnetic moment.

The SQUID magnetometer is constructed from non-magnetic materials. However, after large DC fields have been applied and turned off, some magnetic field lines could remain trapped inside the magnetometer, particularly the superconductive magnet. This may cause the following problems:

1) During AC measurements in zero DC field, the superconducting transition seen in the m' versus temperature plots becomes broadened, which impedes accurate determination of the superconducting transition temperature (T_c).
2) During a DC measurement one needs to measure the magnetization of the sample. The sample should be moving inside a uniform magnetic field so that the motion of the sample in the field does not alter the magnetic state of the sample. Sample motion in a non-uniform magnetic field induces electric fields

along the perimeter of the sample and/or changes the magnetic state or vortex configuration of Type II superconductors

3) Number two above is still an issue for AC+DC measurements. Even though the AC measurement employs the stationary sample technique, the nulling procedure explained above still requires sample movement before each measurement.

4) Wrong initial centering of the sample with respect to the pick-up coil.

These unwanted effects can be greatly reduced by demagnetizing the SQUID magnetometer. To do this, first the largest permissible field is applied, and then the field is switched to approximately -4/5 of this value. Going so on, an alternating sequence is obtained in which each new field value is about -4/5 of the previous one. We have waited 10 seconds after each step for the field to become stabilized. The complete sequence is as follows (values given in Gauss = 10^{-4} T):

-70000, 50000, -40000, 32000, -26000, 20000, -16000, 13000, -10000, 8000, -6400, 5100, -4100, 3300, -2600, 2100, -1700, 1300, -1100, 860, -690, 550, -440, 350, -280, 230, -180, 140, -120, 92, -74, 59, -47, 38, -30, 24, -19, 15, -12, 7.5, 0.

This sequence is followed by "resetting the magnet," i.e. warming it above its superconductive transition temperature of ~9 K. This takes the SC magnet back to the normal state so that any flux trapped inside the magnet is eliminated.

Each time a new sample is inserted into the SQUID magnetometer, it must be centered with respect to pick-up coils. This is most easily done by performing a full length DC scan. The asymmetry of the pick-up coil shown in figure 3.8 creates a typical scan profile as a function of sample position. A fitting to the expected scan profile determines the sample position. To use this profile, the scan length should be quite long. On the other hand, long travel distances should be avoided because the magnetic fields are always non-uniform over large distances. A scan length of 6 cm seems to be a good compromise for centering the sample after the first full scan has been carried out.

Chapter 4

Quantum Stability and Reentrant Bilayer-by-Bilayer Growth of Atomically Smooth Pb Films on Semiconductor Substrates

Because of its profound technological significance, fundamental understanding of metal/semiconductor interfaces has been an important objective in surface science and thin film growth. One active line of current research in this area is the exploration of quantum size effects on the stability and physical properties of metal overlayers on various substrates as the overlayer thickness shrinks to the nanometer scale. As a specific example, experimental studies of silver growth on GaAs(110)[9,41] have led to the formulation of the so-called "electronic growth" model, emphasizing the quantum stability of ultrathin metal films,[24,10] Briefly, when the film thickness is only a few atomic layers to a few nanometers, the confined motion perpendicular to the film of the conduction electrons leads to the formation of two-dimensional (2D) subbands. Quantized motion of the many electrons may, in turn, lead to characteristic dependences

of the total energy of the films on the film thickness, making certain film thicknesses more strongly preferred than others. Such quantum stability can be manifested by novel growth modes that otherwise would not be permitted on the basis of classical surface and interface free energy considerations.[42] More importantly, the existence of quantum growth modes in principle facilitates the fabrication of atomically flat metallic nanostructures for novel devices that can operate in the quantum regime.

The morphological evolution of ultrathin Pb films on Si(111) arguably presents the most spectacular manifestation of quantum growth. Under proper kinetic growth conditions, Pb atoms organize into islands with atomically flat tops or "nano mesas."[21,27,29,43,44] The minimal island height is four or five monolayers (ML), as measured from the wetting layer, while the island height increments are exactly 2ML. Quantum size effects appear to be the underlying cause of this remarkable growth phenomenon. First-principles calculations have suggested that the 5-ML preferred height is a manifestation of "quantum phase separation"[31] while the bilayer increments in the layer thickness can be attributed to bilayer oscillations in the total energy of the films.[31,45,46] Theory and experiment also indicated that the substrate is a key factor in this growth regime. To elucidate the role of the substrate at the first-principles level, one would have to perform slab calculations that include the incommensurate Si substrate, a daunting challenge beyond the scope of current computing capabilities.

In this chapter we present a comprehensive and comparative STM study of Pb growth on three different types of Ge(111) and Si(111) substrates, along with first-principles calculations within DFT and phenomenological modeling for Pb films. Our STM observations show in real space that quantum growth is not just limited to nano mesas but

can be exploited to produce atomically smooth Pb films over mesoscopic length scales on all the three substrates. The minimum coverage for smooth film growth, or critical thickness (t_C), is 5 ML. In the smooth growth regime, we establish the existence of an intriguing reentrant bilayer-by-bilayer (RBBB) mode, characterized by strong preference of bilayer growth with periodic interruption of monolayer growth. The existence of t_C and the salient features of the RBBB mode can be attributed to the quantum nature of the film stability, as confirmed *quantitatively* in DFT calculations for Pb/Ge(111). The Pb/Ge(111) system offers the first example in which direct comparison can be made between experiment and DFT calculations with proper treatment of the substrate. The RBBB growth mode is further shown to be inherently connected to the Friedel oscillations of the film electron density with phenomenological modeling.

Pb was evaporated onto the Ge(111) ($\sqrt{3}\times\sqrt{3}$)$R30°$-Pb(α), Si(111)($\sqrt{3}\times\sqrt{3}$)$R30°$-Pb(α), and Si(111)(7x7) surfaces in ultrahigh vacuum (UHV), using an effusion cell. The deposition rate (ranging from 0.25 to 0.33 ML/min) was calibrated with Rutherford Backscattering Spectrometry. The ($\sqrt{3}\times\sqrt{3}$)$R30°$-α phases of Pb on Si(111) and Ge(111) were prepared by depositing 1/3 ML of Pb (in substrate units) on top of clean Si(111)(7x7) and Ge(111)*c*(2x8), respectively, following well-established procedures.[34,35] Continuous Pb films were deposited onto the 7x7 or α-phase substrates at a temperature of 150 K or less. The films all assume the (111) orientation; accordingly, we define a monolayer as the atom density of a closely-packed Pb(111) plane. The low-coverage α-phase first converts into the dense β-phase[34,35] before multilayer growth commences. The films were subsequently annealed and studied *in-situ* with a variable-temperature

STM. The optimum annealing temperature for smoothing the film depends on the substrate and on the layer thickness and ranges from 200 K to 300 K.

Numerous STM images have been recorded to monitor the various stages of growth. Here, we can only present a sampling of the images that illustrate the key points. Generally, as-deposited films (150 K) are quite rough and up to five different layer heights were observed at the growth front by STM (not shown). Upon annealing to ~200 K, the Pb atoms acquire sufficient mobility to smoothen the films. Figure 4.1(a) shows a 500 × 500 nm STM image of a Pb film**.** Flat-topped islands rising 4 or 5 ML above the wetting layer can be seen; no other island heights have been observed. Based on our thickness calibration, the density of the Pb layers below 5ML appears to be ~20% less than that of bulk Pb. Once the bilayer growth sets in (> 5 ML), the density of Pb equals that of bulk Pb, as determined from the relative area fractions of the flat terraces and 2 ML voids/islands in the STM images. Atomic resolution images between the islands (not shown) confirmed the ($\sqrt{3}\times\sqrt{3}$) structure of the β-phase wetting layer. In this coverage range, Pb islands never merge to form a continuous film. In the following discussion, the layer count excludes the wetting layer (unless otherwise stated), so as to be consistent with the convention in previous studies of flat-top Pb islands.[21,27,29]

Fig. 4.1(b) shows a 500x500 nm image of an almost continuous 7-ML Pb film with 2-ML deep voids. It is clear that in this coverage regime, the 5-ML film is atomically flat and continuous on a mesoscopic length scale while the larger part of the 5-ML surface is covered with an additional bilayer of Pb, making the total film thickness to be 7 ML. The 5-ML and 7-ML terraces neither possess single monolayer steps nor single monolayer voids; thus confirming the onset of perfect bilayer growth on top of the closed 5-ML film.

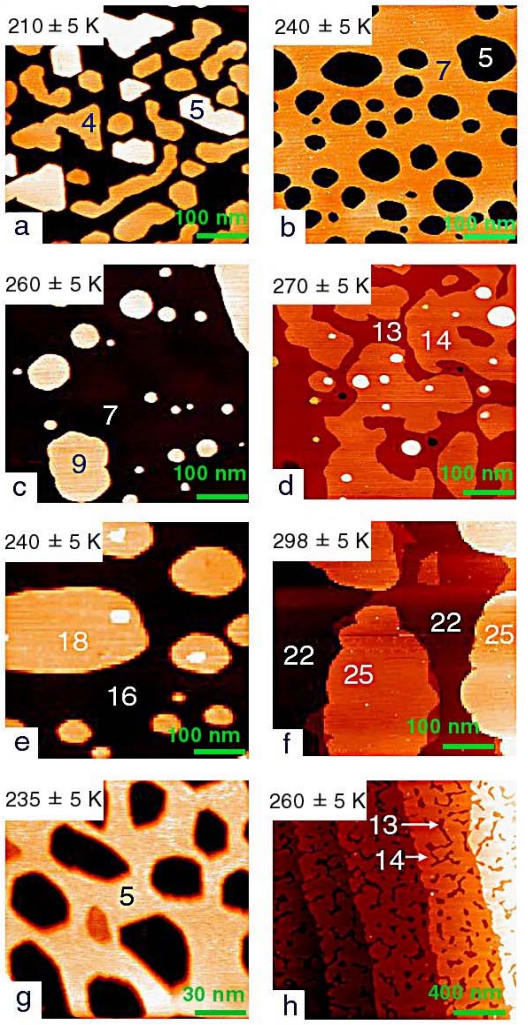

Interface	Observed Layer Thickness										
Si(111)7x7-Pb	5	7	9	11	13	14	16	18	20		
Si(111)(√3×√3)-α	5	7	9	11	13	14	16	18	20	22	25
Ge(111)(√3×√3)-α	5	7	9	11	13	14	16	18	20		

Figure 4.1: STM images of Pb on: (a-f) Si(111)($\sqrt{3}\times\sqrt{3}$)*R*30°-Pb, (g) Ge(111) ($\sqrt{3}\times\sqrt{3}$)*R*30°-Pb, and (h) Si(111)7x7. Layer thicknesses are indicated in each panel and are measured with respect to the wetting layer. The Table summarizes the observed thicknesses for each interface with even-odd crossovers indicated in bold italics. Image sizes and postannealing temperatures are also indicated in (a-h).

Although 5-ML and 7-ML high flat-topped islands have been seen before by STM[21,27,29], the present result is the first real-space demonstration of *continuous film growth proceeding in bilayers*. Fig. 4.1(c) reveals 2-ML high islands on the 7-ML films. Again, the absence of voids or monolayer high islands on the 7-ML film shows that the growth proceeds in a perfect bilayer-by-bilayer mode. Bilayer growth continues until the coverage reaches 13 ML. Fig. 4.1(d) shows a 13 ML high film with monatomic-layer high islands (14 ML) residing on top, and tiny amounts of 16-ML high islands. Amazingly, after this intermission, near-perfect bilayer growth resumes at 14 ML, ending at 22 ML. Fig. 4.1(f) shows 3-ML high steps on top of a 22-ML high film, indicating the onset of another monolayer intermission. In summary, Pb grows in a perfect bilayer-by-bilayer mode from 5 ML to 13 ML and from 14 ML to 22 ML. Evidently, odd numbered layers are favored between 5 and 13 ML while even numbered layers are favored between 14 and 22 ML. As we will show, this RBBB growth mode is a manifestation of the QSE and the even-odd crossover phenomenon is the result of a beating of the interlayer spacing d_0 (2.86 Å) and the Fermi wavelength ($\lambda_F / 2 = 1.98$ Å), which are slightly incommensurate.[31] The resulting beating periodicity of 9 ML implies even-odd crossovers not only between 11-13 ML, but also between 4-5 ML and between 22-23 ML. The latter agrees with the observed trilayer step at 22 ML. Evidence for a 4-5 ML crossover is provided by the coexistence of 4-ML and 5-ML high islands at nominal coverage < 4 ML (see figure 4.1(a)). However, we never observed continuous films of 4 ML or less; however, occasional observation of a single monolayer island or void is attributed to kinetic limitations.

Figure 4.1(g) shows a smooth 5-ML film of Pb on the β-phase of Ge(111) with 5-ML deep voids that go all the way down to the β-phase wetting layer. Upon subsequent deposition, the voids close before bilayer growth commences. Again, a minimum of five monolayers is needed to initiate smooth bilayer film growth on the β-phase substrates of Si(111) and Ge(111), indicative of a *critical thickness* t_C = 5 ML (wetting layer excluded). The even-odd crossovers also occur at the same location as for Si, indicating that the smaller band gap for electron confinement on Ge does not alter the bilayer growth and stability crossovers of the films. The results of Pb growth on Si(111)7x7 are similar. The even-odd crossovers occur at exactly the same locations as for growth of the other two substrates. Figure 4.1(h) shows a 14-ML high film with monatomic-layer-deep voids, taken at the coverage where the second crossover takes place. Notice the very large scale of this figure. Evidently, it is possible to grow *atomically flat Pb on Si(111)*7×7 *on a mesoscopic length scale with a smoothness limited only by the terrace width of the silicon substrate.*

Although oscillations due to QSE have been observed in island heights at coverages less than 9 ML,[21,27,29] the most astonishing result of the present study is that QSE in Pb is a very robust phenomenon and produces atomically flat films over mesoscopic distances, all the way up to 25 ML (possibly even further), and at fairly high temperatures. As shown below, the robust RBBB growth is almost perfectly reproduced in our extensive first-principles DFT calculations of the thickness-dependent film energy for the case of Pb on Ge(111). In these calculations, the Pb(111) films are placed on a 30° rotated Ge(111) lattice. The introduction of the rotation in the supercells enables us to accommodate the lattice mismatch by expanding the Ge lattice by only 1%. Applying the

same trick for Si would require a 9% compression and result in a metallic substrate.[31] The DFT calculations are performed using the Vienna ab initio simulation package(VASP), based on the Perdew-Wang 1991 version of the generalized gredient approximation for exchange-correlation energy and ultrasoft-pseudopotentials, with the Pb *d*-orbitals treated as core states.[47] The Pb/Ge(111) system is modeled by a 2x2 Pb supercell and a ten-layer $\sqrt{3}\times\sqrt{3}$ Ge(111) substrate. The Ge atoms located at the bottom layer of the slab are saturated with hydrogen, followed by a vacuum layer of 19 Å, The in-plane lattice constant of the Pb(111) slab is restricted to its theoretical bulk value (3.56Å), while the layer spacings in the film thickness direction are fully relaxed. A default plane wave cutoff energy of 150 eV and 6x6x1 k-point sampling in the surface Brillouin zone are used in the calculations, Energy convergence is reached when the forces on the relaxed atoms are less than 0.01 eV/ Å.

The stability of a thin film can be determined by its thickness-dependent surface energy: The surface energy of a N-layer Pb film is obtained by subtracting the bulk energy that is linear in the film thickness.[10] The film is stable if the surface energy satisfies

$$2E_s(N) < E_S(N-1) + E_S(N+1), \tag{4.1}$$

where N is measured against the Ge substrate (namely, including the wetting layer). The $E_S(N)$ of Pb on the Ge(111) substrate are shown in figure 4.2(a); they are almost in complete agreement with the experiment, including the presence of the bilayer oscillations and the locations of the stability crossovers (indicated by the arrows). The minimum at 6 ML is consistent with the experimentally observed t_C at (1+5) ML. The

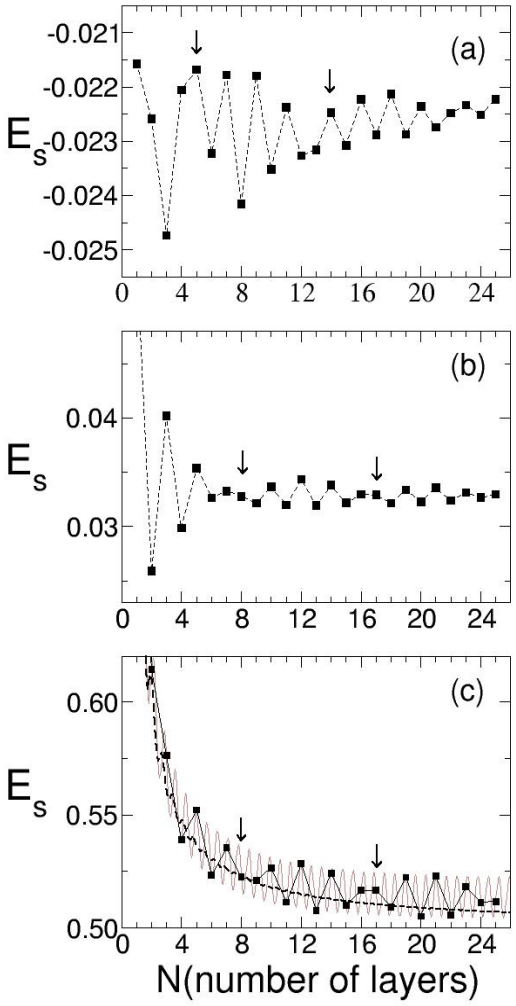

Figure 4.2: (a) Thickness-dependent surface energy E_S (in eV/ Å^2) of Pb(111) films on Ge(111). (b) Same as in (a), but for freestanding Pb(111) films. Notice that the layer numbers in (a) and (b) differs by one from the layer numbers in figure 4.1, due to the presence of a wetting layer in figure 4.1. The arrows indicate even-odd crossovers. (c) Surface energy E_S of a freestanding Pb film calculated using a simple "electrons-in-a-box" model with a constant background potential (dashed line) or a corrugated background potential (red line). The oscillation amplitude v of the corrugated potential, $V_{el}(x) = -v \cos(2k_F x)$, is taken as 0.08 E_F (E_F =9.47eV). The solid squares sample the discrete layer thicknesses, and the surface energies are given in units of $E_F k_F^2/4$.

calculated minimum at 3 ML appears to be the only feature that is inconsistent with experimental observations. Note, however, that the atomic arrangement of the Pb films below 5 ML is not known (Based on our thickness calibration, the density of the Pb layers below 5ML appears to be ~20% less than that of bulk Pb. Once the bilayer growth sets in (> 5 ML), the density of Pb equals that of bulk Pb, as determined from the relative area fractions of the flat terraces and 2 ML voids/islands in the STM images.)

Despite the remarkable agreement between the experimental observations and DFT calculations for Pb/Ge(111), we are yet to fully understand the underlying mechanism for the robustness of the RBBB growth mode. For this purpose, we have also computed the surface energies for freestanding Pb(111) films, as shown in figure 4.2(b).[31] Such calculations show that the RBBB growth mode also exists in freestanding films but the even-odd crossover positions have shifted to 8 ML and 17 ML. The distance of 9 ML between the two crossovers remains the same, indicating that the effect of the substrate is mainly to "phase shift" the crossovers. Therefore, to look for the physics behind the robust RBBB mode, we can focus on freestanding films, avoiding complications caused by the substrate.

For freestanding films, because the existence of the two surfaces will induce Friedel oscillations in the electron density within the films,[48] it has been conjectured that the oscillatory nature of the quantum stability is related to the interplay between the Friedel oscillations in the electron density and the discrete nature of the lattice spacings.[10,31,45,46] In the following we elucidate how such Friedel oscillations in electron density can affect the film stability, which in turn results in the RBBB growth as observed. First, we model

the system as a 2D Fermi gas with a corrugated background potential $V_{el}(x) = -v\cos(2k_F x)$, confined between two hard-wall potential barriers, where $k_F = 1.58 Å^{-1}$ for Pb along the (111) direction, and v is a parameter measuring the magnitude of the oscillatory potential induced by the Friedel oscillations in the electron density. The corresponding surface energies are shown in figure 4.2(c). For a constant background (v=0), there are no apparent oscillations in the surface energy (dashed line), showing that discretization of the kinetic energy spectrum alone does not induce robust oscillations in the quantum stability of the films (Tiny oscillations do show up in the second derivative of the surface energy, particularly for $N < 8$, but this likely does not account for the robust RBBB growth up to at least 25 ML). Oscillations in film stability appear when turning on the $2k_F$ potential (red curve), with the solid squares sampling the energies for discrete layers. Remarkably, these discrete energies clearly indicate the existence of RBBB growth. This simple model calculation even reproduces the crossover locations obtained in DFT calculations of freestanding films. Friedel oscillations decay toward the interior of the film, hence classical layer-by-layer growth should ultimately prevail for thicker films.[43]

In summary, we have presented the first real space observations of a reentrant bilayer-by-bilayer (RBBB) growth mode of Pb on three different substrates of Si(111) and Ge(111). The choice of the Ge(111) substrate enabled quantitative comparison between experimental and theoretical studies of quantum growth and assessment of the role of the substrate at the first-principles level. The RBBB mode of Pb is clearly a manifestation of the accidental near-commensurability of the Fermi wavelength ($\lambda_F / 2$) and the interlayer spacing d_0. Friedel oscillations were invoked to explain the robust quantum growth up to 25 monolayers.

Chapter 5

Overview of the Superconductivity

5.1 Introduction

Superconductivity[40] (SC) is the intriguing ability of the condensed state of matter to carry dissipationless electrical currents below a critical temperature T_c. Superconductivity was first discovered in mercury by Heike Kamerlingh Onnes[49] in 1911 and remained one of the biggest theoretical challenges ever since. The highly successful phenomenological theories of London[50] and Ginzburg-Landau[51] (GL) were developed many years later, in the early 1950's, before a microscopic theory was finally established in 1957 by Bardeen, Cooper and Schrieffer (BCS theory[52]). In 1959, Gor'kov[53] showed that the GL theory could in fact be derived from the microscopic BCS theory. Superconductivity became increasingly appealing for technological applications following the discovery of high temperature superconductors by Bednorz and Müller in 1986.[54] It quickly became clear, however, that the traditional BCS theory could not explain the persistence of

superconductivity up to fairly high temperatures. The record T_c at ambient pressure currently stands at 138 K.[55]

Almost all of the technologically relevant superconductors are type II superconductors. These materials can support supercurrents up to fairly large magnetic fields. This fact, combined with the continuing miniaturization of solid state electronic devices, underscores the need for studying superconductivity in low-dimensional systems or even at the nanoscale. This is an area where fundamental understanding of a longstanding academic problem will be essential for developing tomorrow's nanoscale superconducting devices. The key issues related to superconductivity in low dimensions are the anticipated destruction of superconductivity via disorder and/or entropic fluctuations. In our study, we have approached the extreme two-dimensional limit where the film thickness is much smaller than the characteristic length scales for superconductivity. By employing quantum growth of clean materials, we prepared a system where scattering effects can be explored systematically so that their role in suppressing superconductivity can be elucidated.

In this chapter, first we present a brief summary of the fundamentals of superconductivity. Issues that are particularly relevant to low dimensional systems, such as disorder and fluctuations, will be reviewed.

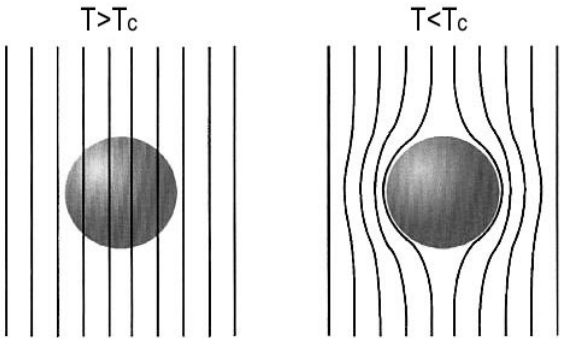

Figure 5.1: Meissner effect: Flux expulsion below the superconducting transition temperature.

5.2 Meissner Effect and London Equations

1n 1933, Meissner and Ochsenfeld[56] discovered that ideal superconductors are perfectly diamagnetic, meaning that magnetic fields are totally expelled from a massive superconducting body. Although the Meissner phenomenon looks deceptively similar to the generation of eddy currents in a perfect, i.e., zero-resistance conductor, the effect is fundamentally different. A superconductor that is cooled below its transition temperature also expels magnetic flux lines in the absence of time varying magnetic field; see figure 5.1. A perfect conductor only responds to time varying fields.

The superconducting state should be suppressed at some critical field H_c when the magneto-static energy of the expelled field lines overcomes the condensation energy of the superconducting state, i.e.,

$$\frac{H_c^2(T)}{8\pi} = F_n(T) - F_s(T)\,. \tag{5.1}$$

$F_n(T)$ and $F_s(T)$ are the free energies of the normal and superconducting states respectively. A phenomenological theory explaining the Meissner effect is the London theory. In 1935 London and London[50] proposed the following equations to explain the basic features of superconductivity:

$$E = \frac{\partial}{\partial t}(\Lambda J_s) \tag{5.2}$$

$$h = -c\nabla \times (\Lambda J_s) \tag{5.3}$$

where

$$\Lambda = \frac{4\pi\lambda_L^2}{c^2} = \frac{m}{n_s e^2}\,. \tag{5.4}$$

Here, c is the speed of light, and n_s is the density of "superconducting electrons". λ_L turns out to be the penetration depth of magnetic field, and m and e are the mass and charge of the electron, respectively. We note that these equations neither contradict nor override the Maxwell equations. They merely constitute some additional constraints, which the fields must obey. The first equation shows that the presence of an electric field would continuously accelerate the electrons, whereas electrons maintain a constant time-veraged velocity in an ordinary conductor. With the help of Maxwell's equations, the second equation gives

$$\nabla^2 h = \frac{h}{\lambda_L^2} \tag{5.5}$$

according to which the microscopic field h must decay exponentially with a characteristic penetration depth λ_L. The above equations 5.2 and 5.3 can be combined into

$$J_s = -\frac{n_s e^2 A}{mc} = -\frac{A}{\Lambda c} \tag{5.6}$$

which is valid in the London gauge, i.e. $\nabla \cdot \mathbf{A} = 0$, where $\mathbf{A}$ is the vector potential.

5.3 BCS Theory

Two important observations suggest that superconductivity is accompanied by the presence of some well-ordered electronic state in which the current carriers have a charge equal to two times the free electron charge.

The first property follows from the exponential decrease of heat capacity:

$$C_{es} \sim e^{-\Delta/T} \tag{5.7}$$

where C_{es} denotes the electronic part of the heat capacity in the superconducting state and Δ is the energy gap borrowed from the end of this section. This fast drop implies a rapid decrease of the entropy. The second property follows from the uniqueness of the superconducting wave function, which can be used to prove flux quantization inside a superconducting ring. The result is

$$\Phi_0 = n(\frac{2\pi\hbar c}{q}) \tag{5.8}$$

where n is an integer and q is the electric charge of the carriers. Experimental verification of flux quantization dictates that $q = 2e$ where e is the electron charge.

One way of explaining this factor of 2 in electric charge and fast drop of entropy would be the formation of electron pairs. First, the total angular momentum of the electron pair would be an integer; hence the pairs would be bosons instead of fermions. These bosonic particles can occupy the same quantum state at low temperature, which would explain the low entropy of the superconducting state. Moreover, the $2e$ charge

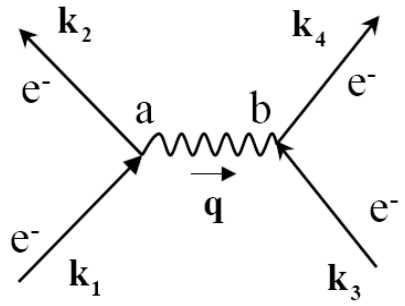

Figure 5.2: Lowest order process describing electron-electron interaction via phonon exchange.

inferred from the flux quantization would be accounted for. Note, however, that although the boson-like behavior of the superconducting transition seems analogous to Bose-Einstein condensation, these phenomena are not identical as was nicely explained in the Nobel Lecture of Schrieffer.[57]

Two ingredients are necessary for realizing such a bosonic system. First, there must be an attractive interaction between electrons to form such bound pairs. Second, the total energy of the bound-pair system must be lower than that of the fermionic system. Cooper has shown that the Fermi sea of electrons is unstable against the formation of bound pairs, regardless of how small the interaction is as long as it is attractive. The origin of the attractive potential is a quantum field theoretic subject about which we will not say much, although we will present a physical motivation.

Besides ordinary electromagnetic interactions mediated by the virtual exchange of photons, electrons in a solid also interact via the lattice, suggesting the following phonon exchange process.

Figure 5.2 shows a schematic of the simplest electron-electron interaction via an "exchange phonon." Using momentum conservation, the momentum of the exchange

phonon, **q**, can be determined at vertices a and b. However, using the phonon dispersion relation, it is easy to show that energy and momentum cannot be conserved simultaneously at the vertices. Nevertheless, such virtual processes can still occur during very small time intervals as allowed by the time-energy uncertainty principle $\Delta E \cdot \Delta t \simeq \hbar$. It then follows from detailed calculations that if the energy difference of the incoming and outgoing electrons is smaller than the phonon energy, i.e. $E_1 - E_1' < \hbar\omega_q$, then the overall process becomes attractive. Finally, the possibility of an attractive interaction also follows from including the ion core displacement into the dielectric function of the medium. These ideas of pair formation were actually developed before the BCS theory, mainly by Cooper and Fröhlich.[40] The BCS theory completed the picture by employing a many body approach so that the behavior of ~10^{23} electrons could be successfully described.

The most important outcomes of the BCS theory are the energy gap $\Delta(T)$ and critical transition temperature T_c. Heat capacity measurements, electromagnetic absorption measurements in the microwave region, and the absence of thermoelectric phenomena imply the presence of an energy gap between the ground state and the quasi-particle excited state. The quasi-particles are the nearly free electrons that are generated if a Cooper pair is broken. The energy required for breaking the Cooper pairs is given by

$$E_g = 2\Delta(T) \tag{5.9}$$

According to the BCS theory,

$$E_g(0) = 2\Delta(0) = 3.528 k_B T_c . \tag{5.10}$$

Finally, BCS coherence length is defined by

$$\xi_0 = \frac{\hbar v_F}{\pi \Delta(0)}. \tag{5.11}$$

The coherence length is roughly the distance over which the superconducting electron density can vary appreciably. In the nonlocal generalization of the London theory, the current at some location **r** depends on the electric field inside a sphere of radius ξ_0 centered at **r**. This "Pippard coherence length" can be estimated using the uncertainty principle in which the momenta of the superconducting electrons are restricted within the range $\Delta p = kT_c / v_F$. This yields

$$\xi_0 = a \frac{\hbar v_F}{kT_c} \tag{5.12}$$

where a is a numerical constant, which was experimentally determined to be $a = 0.15$. Using gap equation 5.10 and comparing 5.11 with 5.12 we get $a = 0.18$; that is a pretty nice way of testing BCS theory. From now on, unless otherwise is stated, ξ_0 will stand for BCS coherence length.

5.4 Ginzburg-Landau Theory

Ginzburg-Landau (GL) theory was developed 7 years before the microscopic BCS theory was established. It concentrates merely on the density of superconducting electrons instead of the excitations. GL theory generalizes the London theory by considering nonlinear effects of the fields strong enough to change the superconducting electron density n_s, and its spatial variation. In this theory, a complex pseudowave-function ψ plays the role of an order parameter within framework of Landau's theory of

second order phase transitions. It can be thought of as the wave function associated with the center of mass motion of the Cooper pairs. The superconducting electron density of the London theory is given by

$$n_s = |\psi(x)|^2 . \tag{5.13}$$

A possible misunderstanding should be remedied: the squared wave function of an electron cannot be thought of as a smeared out electron density. It represents a probability density. Only for a bosonic system in which ψ represents the collective wave function of a very large number of particles, the probability of finding some number of particles in a small volume will average out to be particle density. Here, of course, the particles are Cooper pairs.

In GL theory the free energy density can be expanded as

$$F = F_{n0} + \alpha |\psi|^2 + \frac{\beta}{2} |\psi|^4 + \frac{1}{2m^*} \left| \left(\frac{\hbar}{i} \nabla - \frac{e^*}{c} \mathbf{A} \right) \psi \right|^2 + \frac{h^2}{8\pi} \tag{5.14}$$

where α and β are the expansion coefficients. Writing $\psi(\mathbf{r}) = |\psi(\mathbf{r})| e^{i\varphi(\mathbf{r})}$ and employing a variational procedure to minimize the free energy, the GL equations are obtained as

$$\alpha\psi + \beta |\psi|^2 \psi + \frac{1}{2m^*} \left(\frac{\hbar}{i} \nabla - \frac{e^*}{c} \mathbf{A} \right)^2 \psi = 0 \tag{5.15}$$

and

$$\mathbf{J} = \frac{e^*}{m^*} |\psi|^2 \left(\hbar \nabla \varphi - \frac{e^*}{c} \mathbf{A} \right) = e^* |\psi|^2 \mathbf{v}_s \tag{5.16}$$

where $\mathbf{v}_s$ is the velocity of the supercurrent. An increase of $\mathbf{v}_s$ implies an increase of kinetic energy, which in turn favors a decrease of the order parameter. However, for fixed

order parameter, the supercurrent density is proportional the velocity of the Cooper pairs. This competition sets a maximum to the loss-free current density, which is given by

$$\mathbf{J}_{Depair} = 2e\psi_\infty^2 \frac{2}{3}\left(\frac{2}{3}\frac{|\alpha|}{m^*}\right)^{1/2} = \frac{cH_c(T)}{3\sqrt{6}\lambda(T)} \propto (1-t)^{3/2} \tag{5.17}$$

where ψ_∞ is the order parameter deep inside the material.

Two important outcomes of GL theory are the coherence length $\xi(T)$ and penetration depth. GL theory yields the temperature dependent coherence length as

$$\xi(T) = \frac{\Phi_0}{2\sqrt{2}\pi H_c(T)\lambda_{eff}(T)} \tag{5.18}$$

where λ_{eff} is the scattering modified penetration depth (see below). GL theory gives the temperature dependence of the coherence length for pure and dirty materials in terms of the reduced temperature $t = T/T_c$:

$$\xi(T) = 0.74\frac{\xi_0}{(1-t)^{1/2}} \quad \text{(pure)}, \tag{5.19}$$

$$\xi(T) = 0.855\frac{(\xi_0 l)^{1/2}}{(1-t)^{1/2}} \quad \text{(dirty)}. \tag{5.20}$$

The penetration depth emerging from GL theory is

$$\lambda_{eff} = \frac{m^* c^2}{4\pi|\psi|^2 e^{*2}} \tag{5.21}$$

and has the same temperature dependence as ξ. We note that this penetration depth agrees with London penetration depth if we identify $|\psi|^2 = n_s^*$, $m^* = 2m$ and $e^* = 2e$. However, especially for dirty materials, the deviation is strong because $\lambda_{eff}^2 \approx \lambda_L^2(\xi_0/l) \gg \lambda_L^2$. This can be attributed to an increased m^* or reduced n_s^*.

Finally, the presence of a critical current density beyond which superconductivity disappears, combined with the limited volume in superconducting thin films through which the screening currents can flow, leads to a 2-D screening length $\lambda_\perp$ for fields perpendicular to the film according to

$$\lambda_\perp = \lambda^2 / d \tag{5.22}$$

which for ultrathin films can reach centimeters very close to T_c.

5.5 Surface Energy and Classification of Superconductors

First, assume the situation shown in figure 5.3, which describes a system where *macroscopic* normal and superconducting regions coexist in a slab. "S" denotes superconducting regions and flux lines are passing through normal regions. A surface energy per unit area associated with the interface between normal-superconducting regions can be incorporated into GL theory. This *additional* energy due to presence of the interface is given by

$$\gamma = \frac{H_c^2}{8\pi}\delta\,. \tag{5.23}$$

The overall state of a system like in figure 5.3, i.e. the size and shape of the superconducting and normal regions is determined by the energy balance of surface energy, F_1, and energy stored in the distorted field lines, F_2, which strongly depends on the field configuration just outside the superconducting regions. If δ in equation 5.23 were negative we would not obtain a stable configuration between macroscopic normal and superconducting regions. So, for now we take $\delta > 0$. Assume the slab shown in

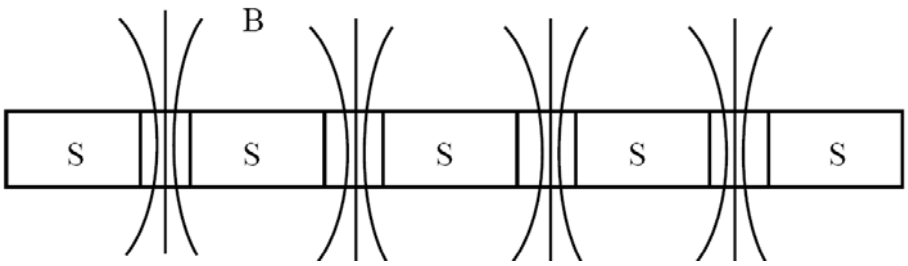

Figure 5.3: Intermediate state of a wide slab. Field lines are passing through normal regions.

figure 5.3, were a single piece superconductor with no interruptions of normal regions. A very high field energy, which would be stored around the perimeter of the sample, would make this configuration unfavorable. The trade off between surface and field energies makes the situation shown in figure 5.3 stable. This state is called "intermediate state". In such a case, it is easy to imagine that there will be so many different patterns of superconducting (normal) regions on the sample with nearly the same total free energy. Hence, in an experiment the sample quality and exact experimental conditions will determine the pattern.

It turns out that $\delta \approx \xi - \lambda$ and is positive for the so-called type I superconductors which exhibit either perfect field screening or intermediate state depending on the sample geometry. If $\delta < 0$, however, the interfaces would proliferate so that the surface energy becomes lower and lower as the field energy also does; because in this case field lines would also run parallel to each other. This case is named "Abrikosov vortex state" and the corresponding superconductors with $\delta < 0$ are called type II superconductors. Abrikosov has anticipated the presence of type II superconductors before their experimental observation and has also shown that "vortices," made of circulating

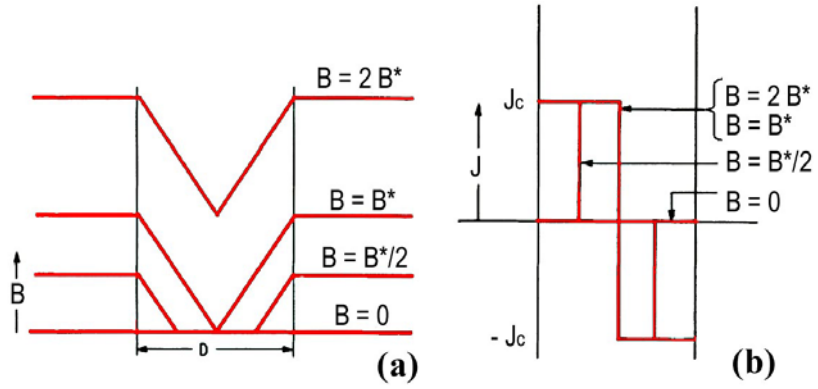

Fig 5.4: Schematic showing the field and current profiles inside a cylindrical sample within Bean model.

supercurrents around normal cores, form a regular lattice. A single flux quanta defined by equation 5.8, with $\Phi_0 = \hbar c / 2e$ is associated with each vortex.

5.6 Bean's Critical State Model

Non-uniform penetration of magnetic field lines through an arbitrarily shaped object and the dependence of the critical current density J_c on the magnetic field in general makes the analytical calculation of the field and current distribution in a given configuration quite difficult. Nevertheless, a simple instructive model was developed by C. P. Bean, which is generally referred to as the critical state model (figure 5.4). This toy model is surprisingly adequate to at least qualitatively understand our dc magnetization curves and ac measurements. The Bean model employs an infinite cylindrical sample geometry, which avoids complications due to demagnetization effects, to be discussed

later. J_c is assumed to be independent of the magnetic field. The resulting field and current profiles can be obtained from Maxwell's equations:

$$\nabla \times B = \frac{4\pi}{c} J \,, \tag{5.24}$$

which becomes due to cylindrical symmetry

$$-\frac{\partial B_z}{\partial r} = \frac{4\pi}{c} J_\phi \,. \tag{5.25}$$

Since J is taken to be independent of B, linear dependence of B on r inside the cylinder is evident. Figure 5.4a and 5.4b show B and J respectively. B* corresponds to minimum field that is necessary to fully penetrate the interior of the cylinder. Screening currents are then circulating throughout the entire volume of the sample.

The highly irreversible nature of the process is evident from the fact that the critical current density is field independent. Suppose a field somewhat above B* is applied first. In figure 5.5, this corresponds to start from point **o** and reach point **a**. Then, the emf induced by slightly *reducing* this field would quickly reverse the current direction which produces a magnetization that is equal in magnitude but opposite in direction, even though the applied field never changed direction. This explains the segment **a-b** in figure 5.5. Following same arguments one more through the path **b-c-d** easily explains why the dc magnetization loops are strongly hysteric. The small trapezoid shown in figure 5.5 is called the minor hysteresis loop. Here, a small-amplitude ac field is superimposed on some dc field. In this case, since B^* is not exceeded at the lower and upper ends of the minor hysteresis loop, the signal picked (m) will be nearly linear in the small ac field unlike the large hysteresis loop **a-b-c-d.** However, if the ac amplitude exceeds B*, then the ac pick-up signal will no longer be sinusoidal. Accordingly, the real part of

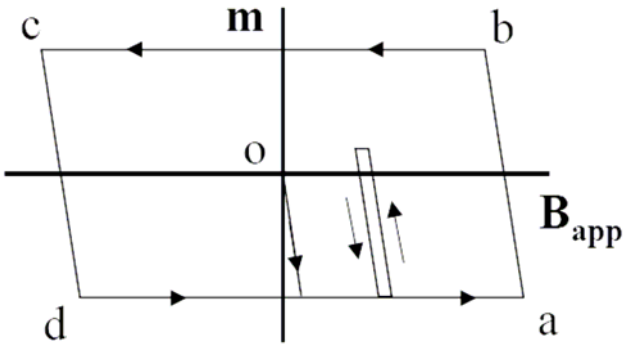

Figure 5.5: Illustration of a hysteretic magnetization loop through the path **o-a-b-c-d-a**... within the Bean model. Small trapezoid represents the minor hysteresis loop traversed during an ac+dc measurement, employing a small ac amplitude.

magnetization may decrease with increasing ac amplitude, which is perceived to be an artifact.

5.7 BKT Transition and Fluctuation Effects

Historically, the superconducting transition in 2-D systems was expected to be driven by the Berezinskii-Kosterlitz-Thouless[1,58] (BKT) mechanism, known from the theoretical works on superfluid He films. A vortex in a 2D superconductor is a so-called topological defect, analogous to a dislocation in a 2-D solid lattice. In the following, we will discuss the BTK scenario for dislocations, keeping in mind that vortices behave very similarly.

In a 2-D system, the long-range strain field induced by a dislocation falls off according to $1/r$ and the associated energy cost, calculated from elasticity theory, diverges logarithmically with the system size according to $\sim \ln(A/b^2)$.[1] Here, A is the areal size

of the system and *b* the magnitude of the Burgers vector. This precludes the formation of isolated defects (i.e., dislocations or vortices) in thermodynamic equilibrium at low temperature. However, geometrically it is easy to see that for pairs of dislocations with equal but opposite Burgers vectors, the strain field decays much faster and the elastic energy cost remains finite (see figure 5.6). In fact, the energy cost depends on the logarithm of the linear distance between the dislocations. Accordingly, there will always be a finite equilibrium population of bound pairs for T > 0 K. Due to the competing effect of entropy, which favors a random distribution of defects, the dislocation pairs (or vortex-antivortex pairs) will dissociate at some temperature T_{BKT}. This is the essence of the BKT transition. In the original work of Kosterlitz and Thouless,[1] it was stressed that the logarithmic interaction energy of a pair of Pearl[59] vortices in superconducting thin films *only* extends to a characteristic distance $\lambda_\perp = \lambda^2 / d$ beyond which the energy falls off as $1/r$. It was therefore questioned whether a BKT transition could be observable in thin film superconductors. Beasley *et al.*,[60] however argued that close to T_c, $\lambda_\perp = \lambda^2 / d$ becomes macroscopic for extremely thin films so that $r \leq \lambda_\perp$ for most vortices, thus restoring the analogy with the original BKT scenario. Subsequent studies have indicated, however, that in practice the BKT scenario is preempted by other mechanisms such as pinning and disorder,[61] which will be discussed in chapter 6.

For a superconductor, the most probable state is the ground state described by the GL equations. However, thermal energies of order $\sim kT$ induce entropic fluctuations which allow for some finite resistance below T_c or some superconductivity above T_c.[40] For the latter case, the conductivity diverges according to $(T\text{-}T_c)^{-1}$ when approaching T_c from

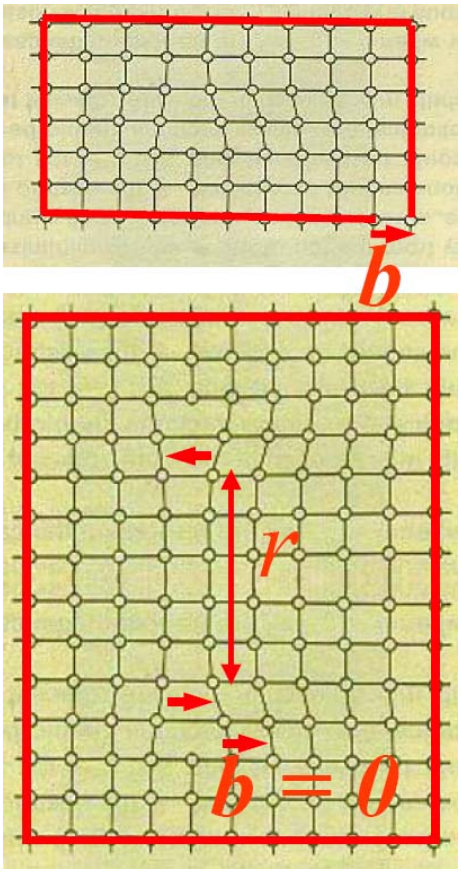

Figure 5.6: Schematic showing the Burgers vectors associated with dislocations.

above.[62]

Fluctuation effects are much more significant in the high temperature superconductors because of their short coherence length ξ_0.[40] In classic superconductors, where ξ_0 is much larger, the coherent volume contains an enormous number of interacting pairs so that fluctuations are very costly and the superconducting transition is very sharp. In the next chapter we will show that even for our extremely 2D sample geometry, the estimated fluctuation width is considerably smaller than theoretical estimates for granular or disordered films.

5.8 Supplementary Notes on Magnetization

There is a certain amount of confusion regarding some basic quantities of electromagnetism: *B* and *H*, the so-called flux density and magnetic flux strength respectively, and magnetization *M*. These quantities are well defined in many textbooks; hence our aim is not to present a formal discussion of them. Instead we will try to emphasize a few of issues assuming that the basic formalism is known.

The presence, magnitude and direction of *B* can be known by measuring the Lorentz force acting on a small test particle, small enough not to disturb the electrodynamics of the existing medium. This definition naturally makes *B* the fundamental magnetic quantity in the sense the electric field *E* in electrostatic is.

The magnetization, *M* is the magnetic moment, *m*, per unit volume induced or present inside a material. In the case of magnetism produced by microscopic magnetic moments, the above definition is a natural one. Here, *M*(x) is a local quantity that indicates the

magnetization averaged over atomic or at most mesoscopic dimensions. On the other hand, if the sample behaves like a large electromagnet that produces magnetism by macroscopic circulating currents, the definition still holds i.e. $M = m/V$ inside the sample and zero outside. Here V is the volume of the sample. The magnetic field strength H is defined by

$$H = B - 4\pi M \tag{5.26}$$

and yields the well known result

$$\oint H \cdot dl = \frac{4\pi}{c} J_{ext} \tag{5.27}$$

where J_{ext} represents the external currents only.

As promised, we will not go into details of why this quantity is defined. It merely helps us to write Ampere's law in terms of free currents, excluding currents that are produced by the response of the medium and simplifies the boundary value problems. However, one should be aware that in the case of a type I superconductor, the induced magnetization is due to *real* currents circulating the macroscopic body of the sample instead of uniformly distributed microscopic magnetic current loops. In the latter case, some authors interpret the induced currents as real currents, which *balance* the external currents so as to keep the flux density, B, zero inside the superconductor. Still, it is useful and customary to adopt (5.27). However, in the case of a macroscopic current loop it is not trivial to define M, a point-wise magnetic moment per unit volume, in equation (5.26). A very useful correspondence between microscopic and macroscopic magnetization exists. See figure (5.7). It can be shown that the macroscopic current loop on the left hand side of this figure can be replaced by fictitious microscopic current loops

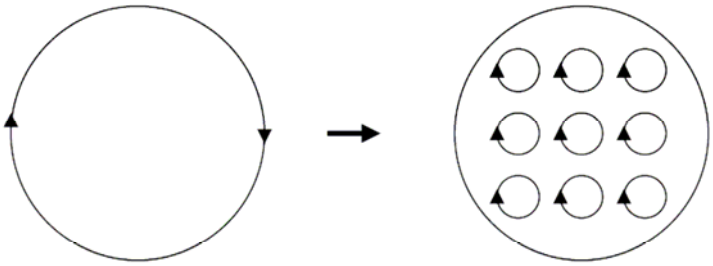

Figure 5.7: Magnetic equivalence of a macroscopic current loop to a collection microscopic magnetic centers.

or magnetic dipoles shown on the right. In this case we recall the definition of M from above; $M = m/V$, where M is the magnetization depicted on the right had side of figure 5.7 and m is the magnetic moment created by the loop on the left.

Up to here, we have summarized the "current" terminology. However, an inspection of Bean's paper[63] for example reveals at once that H instead of B is taken to be zero inside the superconductor and that is given as the volume average of the H, which is clearly a constant. In modern terminology, however, $B = 0$ inside a type I superconducting long cylinder and H inside is the same as the outside and equal to $H_a = -4\pi M$.

Finally, for samples of arbitrary shape

$$H_{in} = H_a - 4\pi nM \tag{5.28}$$

where n is the "demagnetizing factor" and depends on the geometry; $n = 0$ for an infinite cylinder in parallel field geometry and $n = 1$ for infinite sheet in transverse field. We now have

$$H_{in} = H_a + nH_{in} \tag{5.29}$$

and

$$H_{in} = H_a /(1-n)\,, \tag{5.30}$$

which actually indicates the enhancement of the applied field due to bending and compression of the field lines around the sample.

Complicating and confusing the application of these ideas, however, is the fact that the concepts of demagnetizing factor is rigorously applicable only for uniformly magnetized bodies. Consequently, the enhancement implicit in equation 5.30 applies in the Meissner state of a superconductor, but *not* in the intermediate or vortex state.

Chapter 6

Robust Superconductivity in Quantum-confined Pb

6.1 Introduction

Suppression of superconductivity in reduced dimensionality is a long-standing and widely studied phenomenon. Fundamental understanding of the consequences of dimensional confinement for superconductivity is imperative for potential applications of superconductivity in tomorrow's nano-scale devices. Apart from the technological relevance of the subject, issues regarding formation, coherence, and robustness of quantum-confined Cooper pairs are intriguing academic questions.[3,64,65,66,67] The destruction of the ordered phase in two-dimensions in principle proceeds via topological fluctuations of the Berezinskii-Kosterlitz-Thouless (BKT) type,[58,68] but the anticipated BKT transition is usually preempted by much stronger fluctuations, driven by enhanced Coulomb interactions in the presence of disorder.[61] Numerous experimental and theoretical studies of superconductivity in 2D systems considered the normal-state resistance as the primary control parameter for tuning the pairing attraction.[12,69,70,71,72,73,74]

For instance, it has been shown that superconductivity disappears in the ultrathin film limit when the resistance per square, $R_{\square}$, approaches $h/4e^2$ = 6.45 kΩ, which is the quantum resistance for Cooper pairs.[12]

All of the above studies, with the exception of the high-T_c materials, have focused on quenched-condensed, high resistivity films that are strongly disordered or granular in nature, emphasizing fluctuations in the amplitude or in the phase of the superconducting order parameter, respectively (sometimes referred to as the "fermionic" and "bosonic" mechanisms of T_c suppression, respectively[75]). In this study, we explore superconductivity of *single crystalline*, *low-resistivity* Pb films that are atomically flat on a *macroscopic* length scale.[8] The unusual morphology and superior quality of the films can be attributed to the quantum nature of the film stability, as pointed out by several groups.[7,10,2127,43,45] A recent study indicated possible oscillations in the superconductive transition temperature T_c, due to the quantum size effect in atomically smooth Pb films.[76,83] Here, we investigate the thermodynamic and non-equilibrium critical state properties of significantly thinner films, ranging in thickness d from 5 to 18 monolayers (ML) where 1 ML = 2.86 Å, which complements and expands an initial report[8] with additional data and in-depth analysis. The thermodynamic parameters T_c and upper critical magnetic field $H_{c2}(T)$ appear to be extraordinarily robust and are primarily affected by the thin film boundary conditions. The robustness was also indicated by recent STM studies of the tunneling gap for flat-topped Pb islands.[77]

The quantum growth mode of these films naturally leads to the formation of nanoscale voids of atomically-uniform 2 ML depth, which strongly pin the Pearl vortices in the film.[40,59] The observed, *macroscopic* critical currents of several MA/cm^2 are quite

comparable with the levels calculated from the known pinning geometry and superconducting length scales and imply an ideal Bean-like critical state.[40] Thus, both the thermodynamic and non-equilibrium superconductivity parameters of these high-quality films display an extraordinary robustness that is quite unexpected for low-dimensional geometries.

6.2 Experimental Details

In this paper we study the various superconducting properties of ultra-thin Pb films deposited on Si (111) substrates. After chemical cleaning with acetone, well-defined 7x7 reconstructed surfaces were obtained by flashing the samples to about 1470 K in ultra high vacuum (UHV). Pb was subsequently evaporated using a thoroughly degassed effusion cell. The deposition rates (~0.3 ML/min.) were determined using *in-situ* X-Ray Photoemission Spectroscopy (XPS) and *ex-situ* Rutherford Backscattering Spectroscopy (RBS). The crystalline structure of the films were verified by Low Energy Electron Diffraction (LEED). If carefully executed, a reentrant bilayer-by-bilayer growth mode can be established at moderately low deposition temperatures, ranging from 200 K - 250 K (see figure 6.1). This novel quantum growth mode is interrupted periodically by the growth of a single-layer or trilayer.[7] The minimum thickness for smooth layer growth is 5 ML. In this study, we have thicknesses d = 5, 7, 9, 11, 13, 14, 16 and 18 ML. (For the [111] direction in Pb, 1 ML = 0.286 nm.) This layer count excludes the wetting layer which is known to be 1 ML.[23,78,] A small excess amount of Pb, i.e., ($N+\varepsilon$) ML, produces 2 ML nano-mesas on top

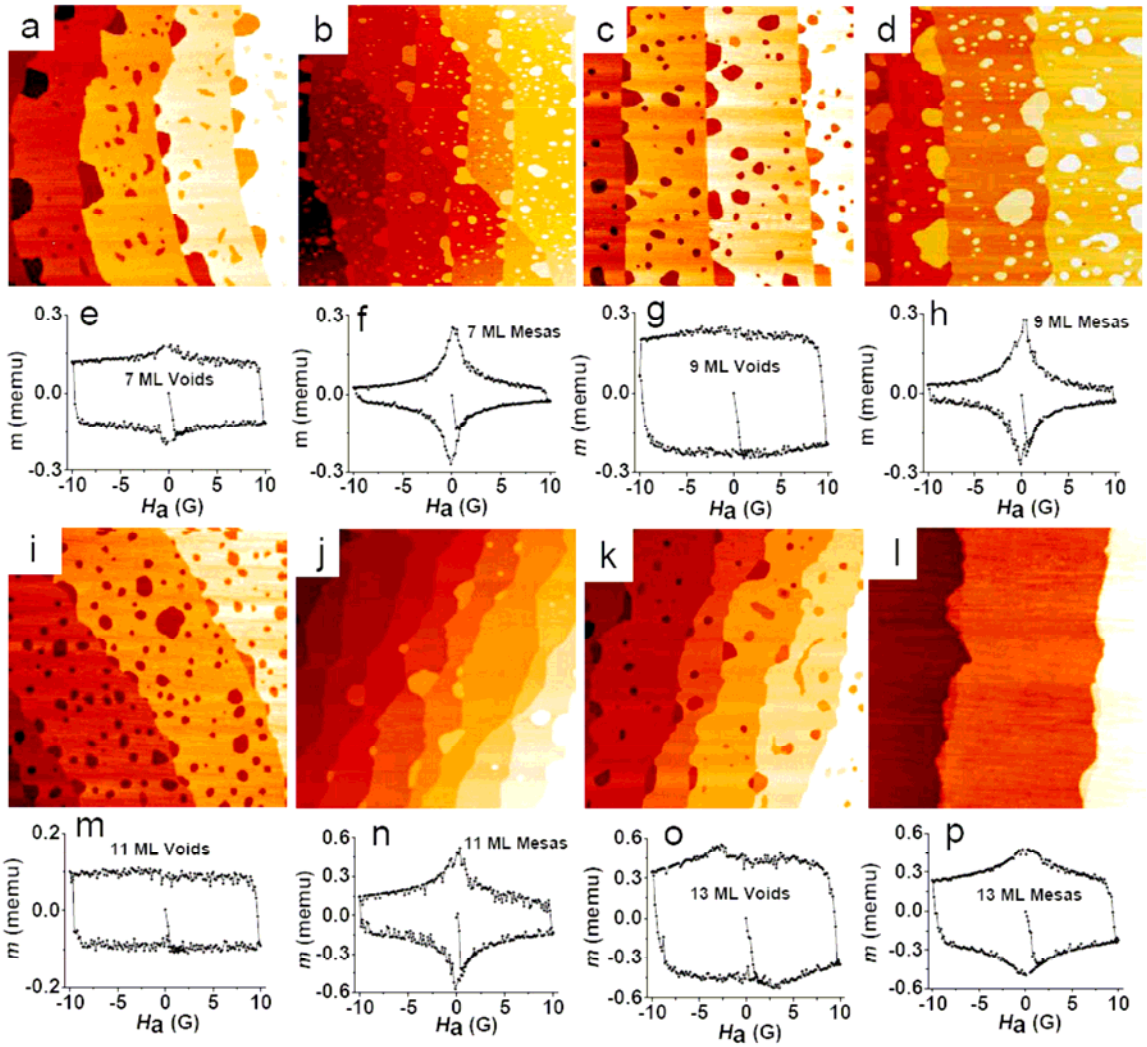

Figure 6.1: Scanning Tunneling Microscopy (STM) images of Pb films on Si(111) substrates. (a, c, i, k) show 7, 9, 11 and 13 ML (monolayer) films with voids (slightly underdosed) with corresponding magnetization loops (e, g, m, o). Same thicknesses with voids (overexposed) are shown in (b, d, j, l) with corresponding magnetization loops (f, h, n, p). All STM images measure about 700 × 700 nm^2; dc magnetic signals are for samples with lateral area of 3 × 3 mm^2.

of an otherwise smooth *N*-layer film; small deficits of Pb generate 2 ML deep nano-voids. Figure 6.1 shows STM images of 7, 9, 11, and 13 (± ε) ML thin films, which reveal the presence of nano-voids and nano-mesas, respectively. The metastable morphology of the Pb films and its chemical integrity were protected by depositing a ~0.1 μm thick capping layer of amorphous Ge at ~100 K substrate temperature, prior to their removal from UHV. The morphological stability of the capped layers at room temperature was verified with STM and will also be evident from the thickness-dependent T_c data.

The superconductive properties of the films were measured inductively as a function of temperature and perpendicular magnetic field, using a SQUID magnetometer (Quantum Design model MPMS-XL). Both reversible (i.e., the superconducting transition) and irreversible (magnetic hysteresis) properties of the samples were investigated employing colinear dc+ac magnetic fields. This contactless method eliminates the need for a conductive capping layer and has the additional advantage that it avoids potential changes in physical properties, e.g., via a proximity effect introduced by metal contacts or metallic capping layers.[76] Furthermore, the inductive determination constitutes a more stringent criterion for the existence of macroscopic supercurrents (obtained from a macroscopic magnetic moment), as opposed to dc transport measurements, which merely detect the onset of a filamentary supercurrent path. For ac studies, a small 100 Hz ac probing field was superimposed parallel to a dc field. These external fields generate circulating screening currents and an associated magnetic moment m. The ac moment, $m = m' - im''$ contains a diamagnetic in-phase term and a lossy, out-of-phase component. Figures 6.2 and 6.3 are examples of the ac magnetic

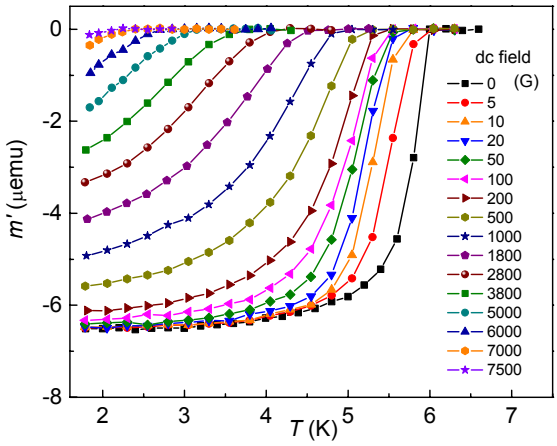

Figure 6.2: Real part *m*' of the ac magnetic response of a 9 ML Pb film with voids, measured in various dc fields. All curves employ an ac probing amplitude of 10 mG superimposed on the dc fields shown in the legend (the superconducting onsets shift from high to low temperature). The shift of the superconductive onset with applied dc magnetic field delineates the H_{c2}(T) phase boundary.

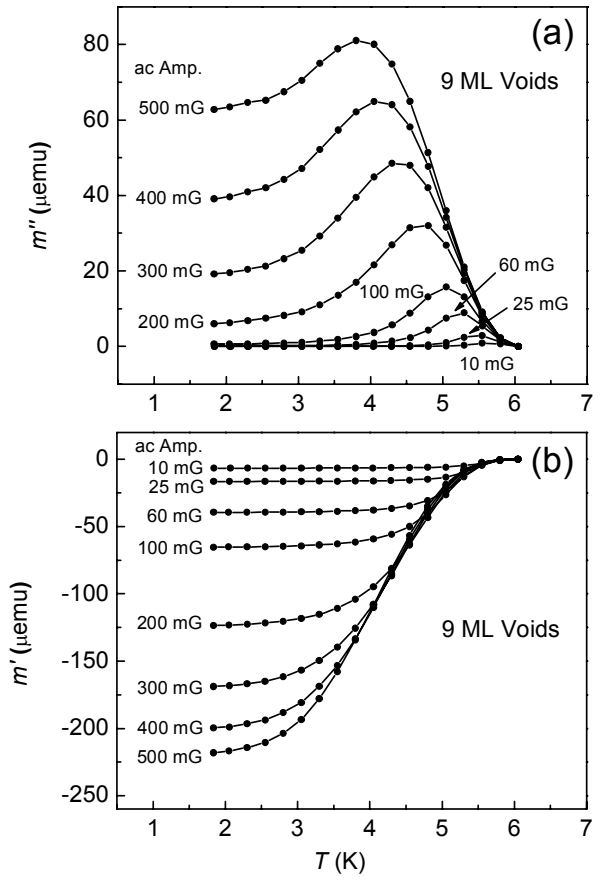

Figure 6.3: (a) Imaginary part *m*″ of the ac magnetic response of a 9 ML Pb film with voids, measured in a 5 G dc field using various probing amplitudes of the 100 Hz ac field. (b) Corresponding real signal *m*' plotted vs. temperature as above.

moments at different dc fields and different ac amplitudes, respectively. Full Meissner-like screening implies $m' = -(4\pi)^{-1}(1-D)^{-1}HV$ where V is the film volume and H is the applied magnetic field. Hence the initial diamagnetic response is amplified by a factor $(1-D)^{-1}$, where the demagnetization factor $D \approx 1$ for a thin film in perpendicular magnetic field. Assuming a thin disc with radius $r \approx 1.5$ mm and thickness d, the susceptibility corresponding to the maximum screening is given (in dimensionless cgs form) by[79] $-4\pi\chi_{\max} = 8r/3\pi d$, which is in excellent quantitative agreement with the measured SQUID signal shown in figure 6.4. By varying the temperature and applied dc fields, we obtain T_c, $H_{c2}(T)$, and the critical current density $J_c(T, H)$, as discussed below.

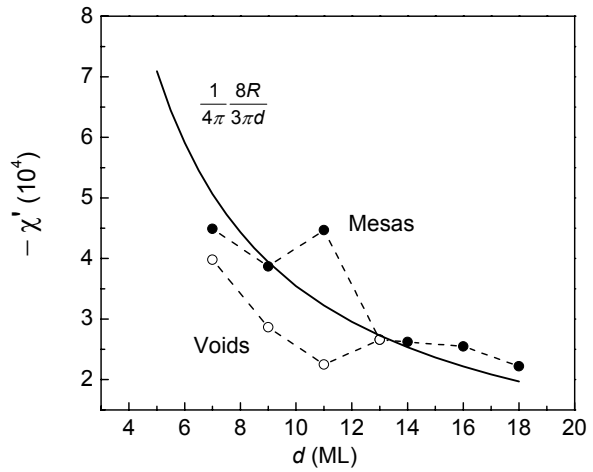

Figure 6.4: ac susceptibilities of 3x3 mm^2 under- and overexposed (overdosed) samples measured at 1.8 K with only 10 mG ac amplitude (0 G dc). Solid curve shows the calculated full-screening values assuming circular samples with 3 mm diameter. The analytical expression is taken from Clem and Sanchez.[79]

6.3 Results and Discussions

6.3.1 Equilibrium Properties

Lead, ordinarily a type I superconductor in bulk form, takes on Type II behavior[80,81] below a critical thickness of ~250 nm.[82] This critical thickness significantly exceeds our film thicknesses. We first consider the equilibrium properties of these ultrathin films. Later, we will show how their unique morphology controls the currents and vortices in these materials. The filled squares in figure 6.5 show the superconductive transition temperature T_c plotted as a function of $1/d$. The T_c data are obtained from the onsets of the in-phase ac response using a 10 mG probing amplitude (Figure 6.5 inset). T_c values of the $(N \pm \varepsilon)$ ML Pb films with mesas or with voids are identical to within 0.1 K. The solid line is a linear fit to the data that nicely extrapolates to the bulk T_{c0} (7.2 K) at infinite thickness. Hence this linear behavior can be expressed as

$$T_c(d) = T_{c0}(1 - d_c / d). \tag{6.1}$$

The "critical thickness" d_c for the appearance of superconductivity is 1.5 ML. This suggests that a single bilayer of Pb should still sustain superconductivity. Note that the interfacial wetting layer is excluded in this layer count. If the wetting layer were included, the $1/d$ plot would no longer extrapolate to the correct bulk T_{c0} which suggests that the wetting layer does not play a substantial role in superconductivity.

Figure 6.5 also includes the T_c data from Guo *et al.*[76,83] The latter values are consistently lower than the present data and do not extrapolate to the correct bulk T_{c0},

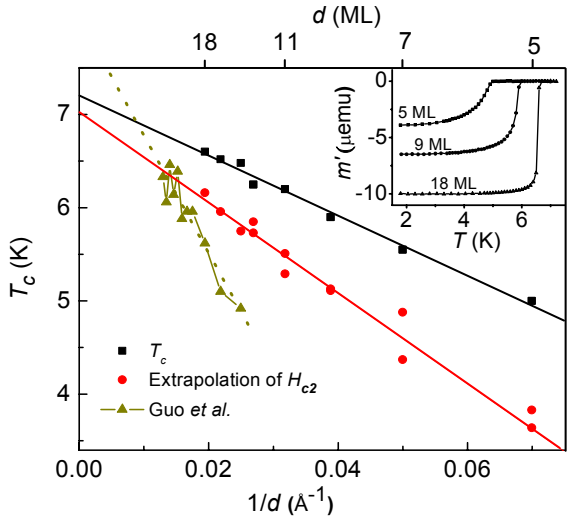

Figure 6.5: T_c data indicated in the legend are obtained from the onset of real ac magnetization taken with 10 mG probing amplitude as exemplified in the inset for some film thicknesses. T_c values scale linearly with $1/d$ and extrapolate to bulk value (7.2 K) in the thick film limit. T_c^* values are obtained by extrapolating the linear part of H_{c2}(T) to zero dc field, as illustrated in Fig. 6. Extrapolating $T_c^*(d)$ to $1/d = 0$ gives a value of (6.96±0.13 K), which is about $1\frac{1}{2}$ standard deviations below the T_c of bulk Pb. Data of Guo *et al.*[76,83] show oscillations in T_c in the layer-by-layer growth regime, which is accessible only for thicknesses above about 20 ML.

suggesting an influence of the Au capping layer used in that study or some other effect. Notice the quantum oscillations in $T_c(d)$ (Reference 76, 83) that are superimposed on the overall $1/d$ falloff in the plot. While a $1/d$ variation of $T_c(d)$ has been observed in many thin film systems, the film smoothness and accuracy of the layer thickness in the present study are clearly unprecedented. The lowering of T_c in thin films was originally interpreted in terms of a BKT transition[1,5860] while later reports emphasized the role of enhanced pair-breaking Coulomb interactions in the presence of strong disorder.[61,84,85] Using the direct proportionality between the mean free path and film thickness, which will be shown in the next Section, we can rule out both scenarios. Specifically, the BKT and pair breaking mechanisms predict that to first order $\Delta T_c(d) = T_{co} - T_c(d)$ should be proportional to $R_{\square}(d)$. Our Pb films are highly ordered. Their sheet resistance can be estimated from the relation for Pb that[86] $\rho \times l = 1.5 \times 10^{-11} \Omega\,\mathrm{cm}^2$; the sheet resistance then follows from ρ and layer thickness d. For thinnest film (5 ML), $R_{\square}$ is only ~200 Ω (as estimated from the mean free path). These values are consistent with normal state properties of ultrathin Pb films determined by Vilfan *et al.*[87] This low resistance would not only produce a negligible $\Delta T_c(d)$ for the BKT scenario but it also lies far below the critical resistance of the superconductor-insulator transition in the pair breaking scenario.[12] In addition, according to reference 87, the normal state conductivity $\sigma_{2D} \propto d$, meaning that $R_{\square}(d)$ and hence $\Delta T_c(d)$ should be proportional to $1/d^2$ instead of the observed $1/d$ dependence. The Finkelstein theory for pair breaking is low dimensionality[84] also does not reproduce the correct thickness dependence.

Simonin[88] provided an alternative explanation for the $1/d$ dependence of T_c by explicitly including a surface term in the three dimensional Ginzburg Landau (GL) free energy. This essentially modifies the boundary condition for the superconducting order parameter in thin films, predicting that $T_c(d) = T_{c0}(1 - 2C\xi^2(0)/d)$. Here, $\xi(0)$ is the coherence length at $T = 0$ K and C is a constant whose microscopic origin is related to the electron-phonon coupling strength and density of states in the bulk. Our data qualitatively agree with this phenomenological model although it should be realized that the explicit expression for C and the resulting expression for critical thickness d_c, are oversimplified.[88] In particular, the experimental values of d_c are considerably smaller than those expected from the Simonin theory.

Figure 6.6 shows $H_{c2}(T)$ data in perpendicular field, as obtained from the onset temperatures of m' in the presence of a dc magnetic field, as illustrated in figure 6.2. At low temperatures $H_{c2}(T)$ varies nearly linearly with temperature, conforming to the standard $(1 - T/T_c)^{-1/2}$ dependence of the GL coherence length.[40] Two observations are very striking. First, the slope of $H_{c2}(T)$ versus T increases systematically for decreasing film thickness. As will be shown in Section B, this can be fully attributed to boundary scattering. Secondly, $H_{c2}(T)$ markedly flattens near T_c resulting in a characteristic "knee profile", which is particularly noticeable for the thinner films. The knee profile is hardly observable at 18 ML, which is also the reason why it has not been noticed in previous studies of films which thickness greater than 18 ML.[83] This feature directly reflects the large shifts in the $m'(T,H)$ data when applying a small dc field; see figure 6.2. This behavior of $H_{c2}(T)$ is reminiscent of that in superconductive-normal metal multilayers.

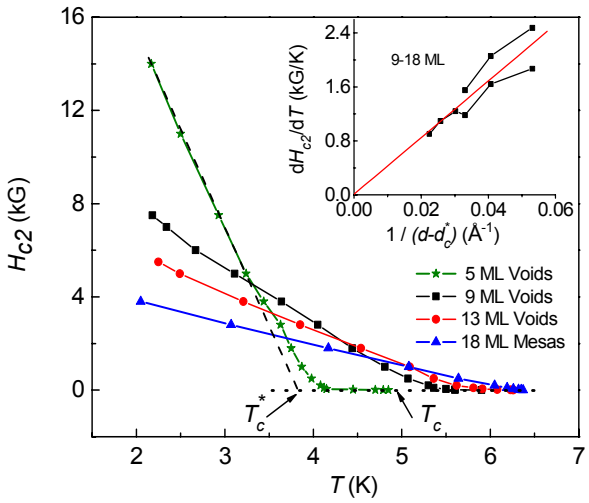

Figure 6.6: $H_{c2}(T)$ values are obtained from the onset of diamagnetic screening in various dc fields, measured using a 10 mG ac amplitude as illustrated in Fig. 6.2. Due to systematic rounding of H_{c2} values near T_c, the linear parts of the H_{c2} curves do not extrapolate to T_c, but rather to a new set of characteristic temperatures denoted as T_c^*; the extrapolation is shown for a 5 ML film. The inset shows the slope of H_{c2} curves in the linear regime, plotted as a function of $\left(d - d_c^*\right)^{-1}$; see text.

For such systems, Takahashi and Tachiki[89] showed theoretically that a similar "knee" structure arises when the temperature-dependent $\xi(T)$ becomes comparable with some T-independent length scale L (e.g., a layer thickness). Subsequently, Gvozdikov[90] showed that a knee structure could also arise in a *thin film* exhibiting structural inhomogeneities with locally elevated T_c. For our Pb films, the length scales L may be associated with distances between scattering centers (which reduce ξ and elevate H_{c2}). For instance, L could be the average terrace size, or the size of (or separation between) the nano-mesas or voids, etc. While this conjecture provides qualitative understanding of the low slope of H_{c2} near T_c and the scattering-enhanced H_{c2} at lower temperatures, further theoretical development is clearly needed.

One theoretical constraint comes from the fact that, in the current data, the knee profile is directly correlated with the film thickness. Extrapolation of the linear $H_{c2}(T)$ segments to zero dc field produces a set of extrapolated GL temperatures $T_c^*(d)$ as shown in figure 6.6. Most remarkably, $T_c^*(d)$ as well as $T_c(d)$ and hence $\delta T_c(d) = T_c(d) - T_c^*(d)$ *all* scale linearly with $1/d$ as plotted in figure 6.5. An alternative interpretation for the existence of a T_c^* would be that $T_c^*(d)$ could perhaps be interpreted as an extrapolated GL or "mean field" superconducting transition temperature, implying that the region between $T_c^*(d)$ and $T_c(d)$ should be dominated by fluctuations. As will be shown below, macroscopic critical currents can still flow in the T-region between T_c and T_c^*, which greatly reduces the likelihood of explanations based on fluctuations or flux melting scenarios. Moreover, we estimated the width of the possible fluctuation region in thin Pb by evaluating the 2D Ginzburg number $G_i = \delta T_c / T_c$ using the expression derived by

Bulaevskiĭ *et al*.[91] The resulting value of δT_c is smaller than the observed $\Delta T_c(d)$ by at least one order of magnitude. In addition, inserting the mean free path result $l(d) \cong 2 \times d$ into the Bulaevskiĭ expression again implies that $\delta T_c \propto 1/d^2$, rather than the observed $1/d$ dependence. Specifically, the magnitude and thickness dependence of δT_c of these low-resistivity, crystalline thin films cannot be accounted for within the bosonic or fermionic fluctuation scenarios of T_c suppression,[61,84,85]nor can it be explained by involving mesoscopic fluctuations.[75] Finally, we did not observe a qualitative agreement between our data and the 2-D flux-line melting theory[92] because the curvature of H_{c2} near T_c should then be opposite to what we observe.

6.3.2 Length Scales

Having discussed the equilibrium properties of the ultrathin lead films, we now consider the fundamental length scales, which will be needed later to evaluate the non-equilibrium critical-state properties. While the Type I-Type II crossover in thin films is fundamental and does not require an altered Ginzburg-Landau parameter[93] $\kappa = \lambda/\xi$, the fundamental length scales in these Pb films are significantly affected by the 2D geometry. For instance, the dominant role of surface scattering in the ultra-thin limit reduces the GL coherence length ξ_{GL} significantly below the BCS value of bulk Pb, $\xi_0^{bulk} = 905$ Å. Values for $\xi_{GL}(T)$ were obtained from upper critical field data via the relation $H_{c2}(T) = \Phi_0 / 2\pi\xi_{GL}^2(T)$ where Φ_0 is the flux quantum.[40] $H_{c2}(T)$ was measured down to 1.8 K as shown in figure 6.6 for some selected thicknesses . For a 9 ML Pb film,

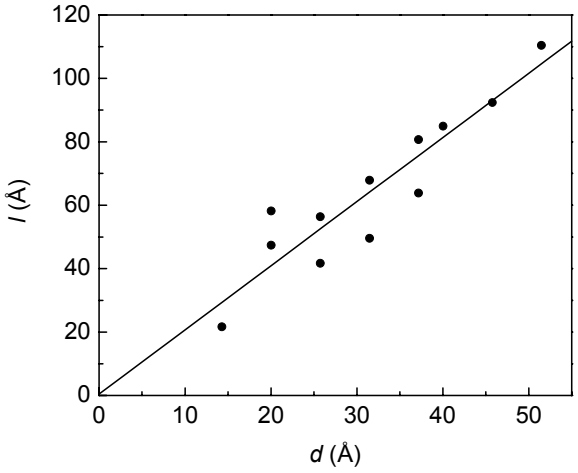

Figure 6.7. Electronic mean free path (mfp) values obtained from the full value expression[94], equation 6.2. The mfp for a film with voids is always smaller than that with mesas. Hence two sets of values are shown for some thicknesses.

$\xi_{GL}(1.8K) \approx 200$ Å, which is reduced significantly from the value of bulk Pb. The reduction in ξ_{GL} is attributed primarily to the small electronic mean free path $l(d)$. Disorder in the interfacial wetting and possibly the capping layers is most likely the dominant contributor to the scattering rate. From the "full value" expression,[94]

$$\xi_{GL}(d) = 0.739[\xi_0^{-2} + 0.882(\xi_0 l)^{-1}]^{-1/2}(1 - T/T_c)^{-1/2} \qquad (6.2)$$

we obtain $l(d) \cong 2 \times d$ at 1.8 K These values shown in figure 6.7 are somewhat smaller than the values given in reference[8] which were calculated for 0 K. Alternatively, they are significantly larger than the mean free paths $l \approx 0.5 \times d$ inferred from Bao *et al.* (reference 83) from their upper critical field data and, independently, from their resistivities using the $\rho \times l$ product of Strongin *et al.*[86] Note that we find *l(d)* to be

systematically smaller for the films with voids as compared to those with mesas. The linear fit in figure 6.7 was not forced to pass through zero. For calculating *l(d)*, the BCS coherence length ξ_0' has been renormalized to account for the lower T_c in thin films, using[94] $\xi_0' T_c^{film} = \xi_0^{bulk} T_c^{bulk}$. Our mean free path estimates are slightly smaller than those of Vilfan and coworkers from normal state transport measurements.[87] These authors also find that $\sigma \propto d$ and consequently $R_{\square} \propto 1/d^2$.

According to the Anderson theorem,[95] the product $\lambda\xi$ should be independent of scattering and thus independent of the film thickness; consequently $\lambda_{eff}\xi_{GL} \approx \lambda_L \xi_0'$ where λ_L is the London penetration depth of bulk Pb (~370 Å). For a 9 ML film we obtain $\lambda_{eff} \approx 1500$ Å so that $\kappa = \lambda/\xi \approx 5$. Finally, the 2D screening distance for a thin film in a perpendicular magnetic field is $\Lambda \equiv 2\lambda_{eff}^2 / d$; the length Λ can be interpreted as the lateral radius of a "Pearl vortex"[40,59] which could exceed the sample dimensions (3x3 mm^2) for very thin films very near T_c.[96]

Finally we note that the above estimates can be used to explain the systematic thickness dependence of H_{c2} in the GL regime, using the combined effects of the $1/d$ variation of $T_c^*(d)$ and a mean free path limited by boundary scattering. Using equation 1, it can then be shown that $-\mathrm{d}H_{c2}/\mathrm{d}T$ should be proportional to $\left(d - d_c^*\right)^{-1}$ as is indeed observed experimentally (Figure 6.6: inset). Here, $d_c^* \cong 2.4$ ML is the thickness where $T_c^*(d)$ extrapolates to 0 K. Hence, the thermodynamic parameters T_c, T_c^*, and $H_{c2}(T)$ of high quality Pb films are primarily determined by the boundaries of the film and thus display a robustness that is quite unexpected for low dimensional geometries.

6.3.3 Non-equilibrium Critical-State Properties

The non-equilibrium properties of the Pb films are also remarkably robust. Figure 6.1 shows the dc magnetization loops of underdosed 7, 9, 11, 13 ML films with 2 ML deep voids and those of the overdosed films with 2 ML tall mesas. The contrast between the two cases is striking, consistently showing hard, nearly rectangular hysteresis loops for the films with voids and soft hysteresis loops for the films with mesas. From the highly irreversible magnetization of the film with voids, we conclude that those films are almost ideal Bean-like[40,63] superconductors due to the exceptionally strong vortex pinning by the nano-voids. Their areal density N_A is estimated to be ~2.6×10^{10} cm^{-2} and the diameter of the blind holes is comparable to ξ_{GL}. By attaching one flux quantum Φ_0 per void, one obtains a "matching field" $B_\Phi = N_A \times \Phi_0 \cong 5500$ Gauss meaning that the pinning array is strongly underfilled at low dc field. The critical current density was calculated using the critical state relation $J_c = 30m/Vr$ where m is the measured dc magnetic moment, V is the volume of the film and r is the macroscopic radius of the sample (≈ 1.5 mm). This yields J_c = 2.0 MA/cm^2 for the underdosed 9 ML film at 2 K in 5 Oe dc field. In contrast, application of small dc fields quickly depresses the magnetization of the overdosed films, indicating that the areal density of *effective* pinning centers is too small to accommodate even a low density of vortices. While voids attract vortices and pin them, mesas repel them, meaning that vortices can move and dissipate energy by simply avoiding the mesas.

J_c was also measured using ac susceptibility. It follows from the critical state model that the critical current density can be calculated from the peak position of the imaginary ac susceptibility (Figure 6.3) using $J_c = 1.03 H_{ac} d^{-1}$ where H_{ac} is the amplitude of the applied ac modulation field.[79] Accordingly, we have measured χ'' in various ac+dc fields as shown in figure 6.3, to obtain a comprehensive set of $J_c(T, H)$ values. Within the resolution of the measurement, the onset of χ'' signaling dissipative irreversible magnetization always coincides with the onset of diamagnetic screening χ'. This indicates that the thermodynamic $H_{c2}(T)$ phase boundary coincides with the onset of irreversible magnetization. Notice that the formula $J_c = 1.03 H_{ac} d^{-1}$ does not include the sample volume. The consistency between the J_c values from ac susceptibility (2.8 MA/cm^2) and dc magnetization (2.0 MA/cm^2) thus indicates that the critical currents are truly macroscopic. For instance, if the sample were subdivided into $N \times N$ disconnected superconductive domains, then the dc measurement would produce J_c values smaller by a factor of $1/N$. In fact, this macroscopic nature of the screening response was already evident from figure 6.4 where it is shown that m' corresponds to *maximum* diamagnetic screening. Hence the ~ 2 MA/cm^2 critical currents follow a macroscopic trajectory along the sample's circumference, despite many surface imperfections such as atomic steps on the substrate. For a 9 ML film, these current densities imply circulating macroscopic supercurrents of order 100 mA.

In figure 6.8 we show the critical currents obtained from ac+dc measurements as a function of temperature for various film thicknesses at 5 G dc field. The significantly lower J_c of the films with mesas is consistent with the observation of magnetically soft

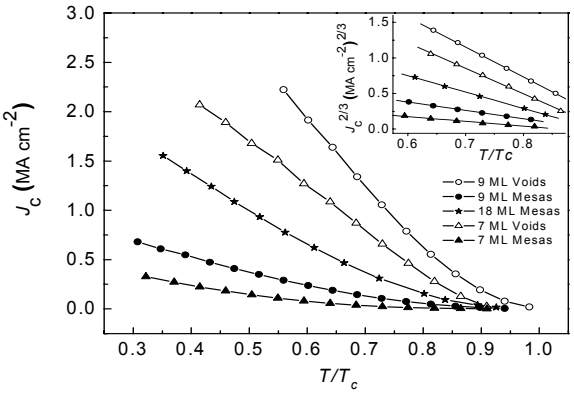

Figure 6.8: Critical current density J_c, as obtained from the peak positions of the imaginary ac magnetization curves using $J_c = 1.03 h_{AC} d^{-1}$. Note that for each ac amplitude, one only obtains the J_c value at the temperature where χ'' is maximum. J_c values for other temperatures were calculated from the other χ'' values using the analytical results of Clem-Sanchez[79] for a Bean-like superconductor. Inset shows $J_c^{2/3}$ to illustrate the GL temperature dependence of the critical current density.

loops in the dc measurements. We estimate the depairing current density of our films using $J_d \approx H_c / \lambda_{eff} \cong 20$ MA/cm^2 (for a 9 ML film with voids). This result indicates that in the thin film superconductors reach ~10% or more of the theoretical depairing current density, which is extraordinarily high. This observation is further illustrated by a simple model calculation, as shown below.

The scale of the vortex line energy per unit length is given by[40] $\varepsilon_0 = \Phi_0^2 / (4\pi\lambda_{eff})^2$. The 2 ML depth of the voids amounts to a significant percentage of the total film thickness, which in turn implies that voids must act as trapping centers of the Pearl vortices. Because the uniform depth of the quantum defects can be thought as a segment

of a columnar defect or "blind hole," the critical current density can be estimated from a slightly modified expression of Nelson and Vinokur:[97]

$$J_c = [c\Phi_0 / (4\pi)^2 \lambda_{eff}{}^2 \xi] \times (\Delta d / d) \tag{6.3}$$

where c is the speed of light and Δd = 2 ML is the depth of the pinning center. Estimating J_c from this expression gives a value of about 4 MA/cm^2 at low temperatures and indicates a pinning energy $U_0 = \varepsilon_0 \Delta d$ of ~500 K. The experimental value of J_c is ~2.8 MA at low temperatures and compares quite well to the calculated value. Furthermore, the observed temperature dependence illustrated in the inset of figure 6.8, $J_c \propto (T_c^* - T)^{3/2}$ in the GL regime below T_c*, is fully consistent with the expected $(T_c^* - T)^{-1/2}$ variation of λ_{eff} and ξ in GL theory where H_{c2}(T) is linear.

Within the critical state model, the relation between χ' and χ'' can be calculated as a function of $2H_{ac} / J_c d$.[79] This relation makes it possible to interpolate the J_c values between the discrete J_c values that were obtained from the peak positions in χ'' (Figure 6.3). It furthermore allows us to extrapolate J_c outside our measurement range. Figure 6.9 shows a set of J_c values obtained in this manner.

The demarcation between loss-free current flow and dissipative conduction in a superconductor can be parameterized using the power law exponent n in the current-voltage relation $E = E_c (J / J_c)^n$ (E is the electric field).[79,98] The Bean model implies perfect loss-free currents, or $n = \infty$. Ohmic transport, on the other hand, implies n = 1. The relation between χ' and χ'' can be calculated numerically for different values of n.[98] Hence, n can be estimated by comparing the experimental (χ', χ'') relation with the

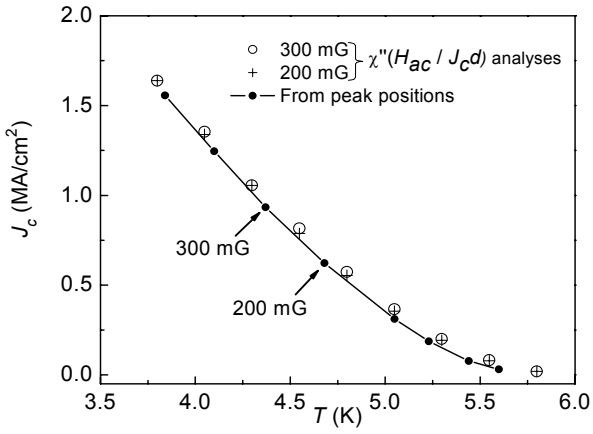

Figure 6.9: Critical current densities obtained from (a) the peak positions of the imaginary magnetization, or (b) off-peak measurements, using the calculations[79] according to Clem and Sanchez, all for a 9 ML film with voids. Two independent J_c calculations using the 200 and 300 mG data are shown.

theoretical relations for different n. Indeed, the (χ', χ'') values obtained from the ac response nicely collapse onto the Cole-Cole diagram of the Bean critical state ($n = \infty$), as shown in figure 6.10(a) for 9 ML film with voids. These data include all the (χ', χ'') pairs measured between 1.8 K and T_c, at 5 Gauss dc field with ac amplitudes ranging from 200 to 1100 mG. Data that are measured with ac amplitudes below 200 mG significantly deviate from the collapsed Cole-Cole data, which will be discussed later. The maximum of the Cole-Cole plot is located at $\chi'' \cong 0.245$, in excellent agreement with the theoretical maximum of a Bean-like critical state for a thin disk, which gives $\chi'' \cong 0.241$.

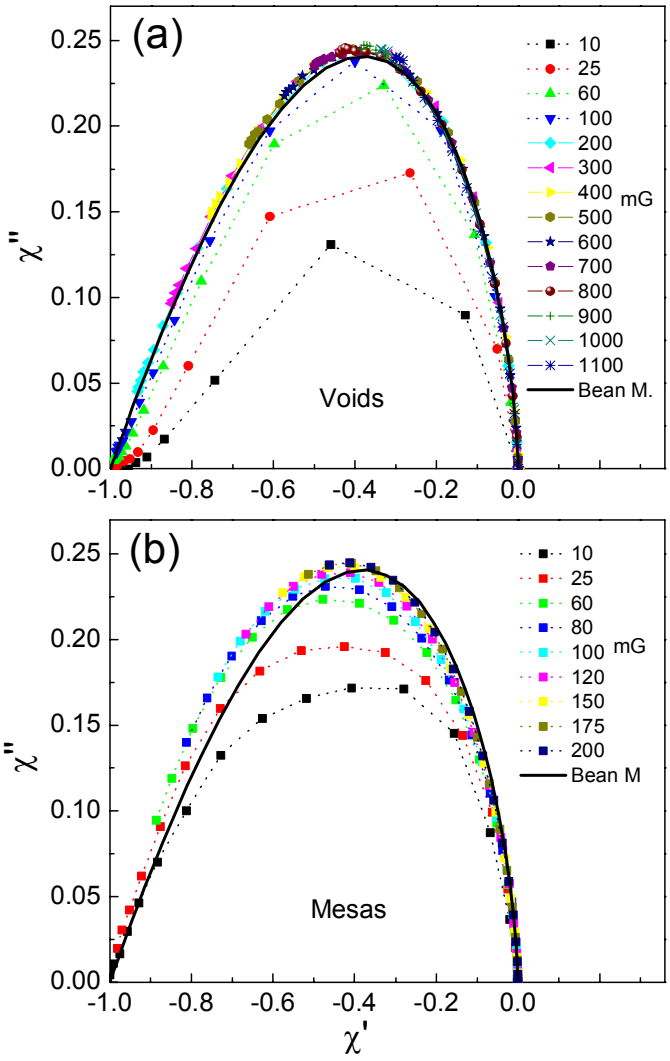

Figure. 6.10. Cole-Cole plot of χ'' versus χ' for 9 ML films. (a) with voids and (b) with mesas, all measured in a 5 G dc field using many different ac field amplitudes, as shown. Solid curves correspond to the ideal Bean case.

Cole-Cole plots for various dissipation mechanisms were calculated by Shantsev *et al*.[99] Comparison between the collapsed Cole-Cole data in figure. 6.10(a) and theoretical Cole-Cole plots for finite creep exponents indicate that n>100. This conclusion of very large n-value was verified independently by real time measurements of the current decay rate, as discussed later. Qualitatively, the Cole-Cole plot for the film with mesas in figure 6.10(b) exhibits a pronounced deviation from the ideal Bean curve, compared with the film with voids; the shift of the peak toward more negative values of χ' is consistent with the weaker pinning[99] and softer hysteresis loops in the former material.

As noted, for small ac amplitudes the experimental maxima of χ'' fall well below the Cole-Cole plot of the Bean model. To delineate this effect, we have plotted the observed maximum of χ'' as a function of the ac field amplitude for 9 ML films (Figure 6.11). It is likely that the reduced dissipation at low H_{ac} arises from "elastic motion" of the vortices in the Campbell regime[100] in which the low driving force is too weak to depin vortices. At very low ac fields, the force on the vortices is proportional to their *elastic* displacement. The associated Meissner-like, non-dissipative currents serve to screen the film and restrict the loss (χ''_{max}) to levels below that obtained in a strictly Bean-like critical state. Qualitatively similar reductions in χ''_{max} were observed in low ac fields by Pasquini[101] *et al*. (and references therein) in thin films of the high-T_c superconductor $YBa_2Cu_3O_7$; these researchers successfully analyzed their findings in terms of a high screening, low dissipation Campbell regime at low amplitudes. Also, Herzog *et al*.[102] observed an amplitude dependence similar to that in figure 6.11 (with, however, a small but experimentally significant continuing increase in χ''_{max} in large fields H_{ac}). These

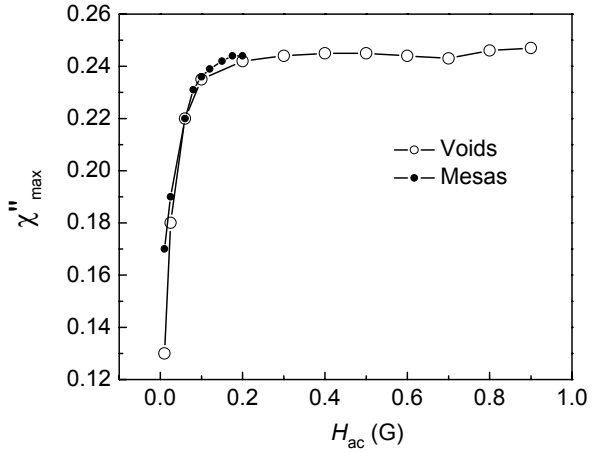

Figure 6.11: Maximum value of χ"attained, plotted as a function of the applied ac probing amplitude. Samples are 9 ML films with either voids or mesas, in an applied dc field of 5 G.

authors too attributed the low field falloff in χ''_{max} to an "increased dominance of screening rather than a change towards a different loss mechanism." Given the marked differences in their J_c-values, it is curious that the films with voids and mesas behave so similarly in figure 6.11; it may be that the difference between two morphologies are irrelevant for the extremely low flux density at low ac amplitudes.

6.3.4 Flux Creep

Lastly, let us consider the time dependence of the critical current density or "flux creep". In order to measure the decay rate of the critical currents without potential measurement artifacts, the sample was held stationary during the measurements. To begin, we quickly moved the sample from a position with low field (8 cm below the

center of the magnet) into the high field region at the center of the SQUID pickup coils. This induces the critical state. The sample was then kept stationary as the SQUID signal was monitored over time.[103] The resulting data were analyzed according to the relation

$$J(t) = J_0 - J_1 \ln(1 + t/\tau) \tag{6.4}$$

where τ is an initial transient time.[104] Here,

$$J_1 = \frac{\partial J(t)}{\partial \ln(t)} \tag{6.5}$$

and

$$\tau = 0.41 \frac{J_1 d}{dH_a / dt} \tag{6.6}$$

Equation (4) describes the signal decay reasonably well, as illustrated in figure 6.12 for data at T = 2.5, 3.5 and 4.5 K. The normalized creep rate S then follows from

$$S = \frac{1}{J_c} \frac{dJ}{d\ln(t)} \cong \frac{J_1}{J_0} = \frac{T}{U_0} \tag{6.7}$$

where the last equality comes from standard Anderson-Kim theory for flux creep and U_0 is the vortex pinning energy. The resulting values for S are shown in the inset of figure 6.13. Using the relation[105] for the power law exponent $n = 1 + S^{-1}$, we obtain independently that n ~100, in good agreement with conclusions from the Cole-Cole analysis. According to the Kim-Anderson framework of flux creep[106,107] $S(T) = \frac{T}{U_0(T)}$. From the vortex pinning energy for single-vortex pinning,

$$U_0(T) = \varepsilon_0 \Delta d \propto \frac{1}{\lambda^2(T)} \propto \left[1 - \left(\frac{T}{T_c}\right)^2\right] \tag{6.8}$$

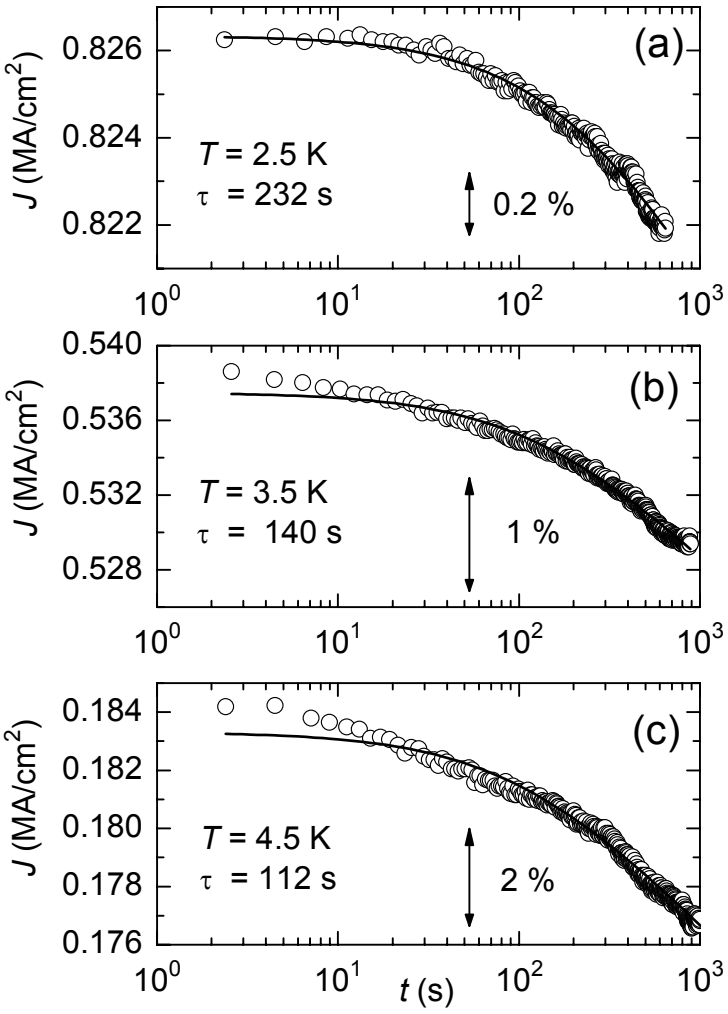

Figure 6.12: Decay of the critical current density vs. time (log scale) for a 9 ML film with voids. Data taken at (a) T = 2.5 K, (b) T = 3.5 K and (c) T = 4.5 K. Solid curves are fitted to equation 6.4 in the text. Markers show fractional change in magnitude of the signal.

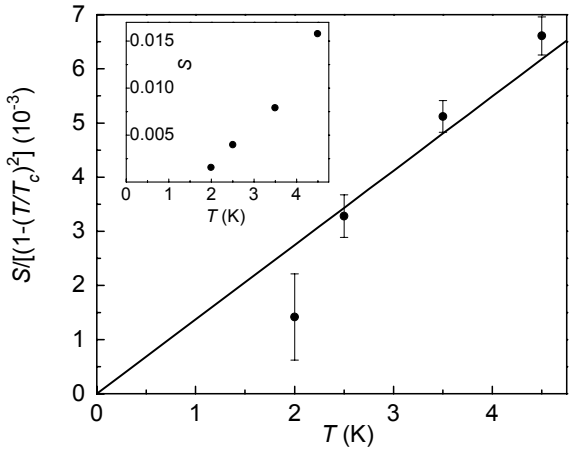

Figure 6.13: The normalized creep rate *S* as corrected for the temperature dependence of vortex energy ε_0, plotted vs. temperature. Plotted quantity demonstrates the temperature dependence of the creep rate in the Kim-Anderson formulation for a 9 ML film with voids. Inset shows the measured creep rate *S*, which is quite low.

we finally obtain

$$S \times \left[1 - \left(\frac{T}{T_c} \right)^2 \right] = \frac{T}{U_0(T=0)} \quad . \tag{6.9}$$

A plot of this quantity vs. temperature in figure 6.13 reveals a reasonably linear dependence, thus supporting this analysis and yielding $U_0(T=0) \cong 700$ K This result is in quite good agreement with the earlier *independent* estimate $U_0 = \varepsilon_0 \Delta d$ ~500 K. Within our resolution, quantum tunneling of vortices does not seem to play a role in our system, as this would imply a non-zero creep rate *S* as $T \to 0$. Attempts to perform similar "stationary sample" creep measurements on a film with mesas were unsuccessful, due to the smaller signals and lower values of J_c. Overall, these "flux creep" results are

consistent with the findings of the ac response study, that the ultrathin Pb films with voids exhibit strong vortex pinning and robust critical-state behavior.

6.4 Concluding Remarks

In summary, superconductivity in atomically flat, quantum confined Pb films is unexpectedly robust against superconducting fluctuations and pair breaking mechanisms that are usually associated with disorder and screening in reduced dimensionality. Superconductivity is controlled via a single parameter (thickness), which is varied with atomic precision. The film thickness directly affects T_c via the boundary conditions for the superconducting order parameter, while the superconductive length scales λ and ξ are affected via boundary scattering. The experiments provide an internally consistent set of parameters that semi-quantitatively describe the thermodynamics and non-equilibrium response of the superconducting critical state. The power and validity of the 3D GL analysis for this extreme 2D geometry is perhaps the greatest surprise. This observation, however, may be rationalized on the basis of the time-energy uncertainty principle $\Delta E \geq \hbar < v_F > l(d)^{-1}$ (v_F is the Fermi velocity). ΔE appears to be of the order of a few tenth of an eV, comparable to the intersubband spacing in quantum confined Pb, so that carriers are easily scattered between 2D subbands. Strict 2D Cooper pairing thus requires long mean free paths or, equivalently, a perfect interface between the film and the substrate.

Chapter 7

Growth and superconductivity of Pb-Bi alloys in the quantum regime

The phrase "quantum engineering" generally refers to the possibility of creating novel electronic structures through atomic-scale control of the quantum mechanical boundary conditions. It has been firmly established that the quantum confinement of itinerant electrons can be exploited to precisely control the formation and stability of atomically smooth crystalline metal films, a process, which was originally coined "electronic growth."[10] The thermodynamic and non-equilibrium properties of these ultrathin metal films are strongly modulated by the quantum size effect. These include formation energy,[7,32] lattice relaxations,[108,109] work function,[16] chemical reactivity[110,111] and electrical transport properties.[87,112] In the previous chapter, it was demonstrated that superconductivity in quantum confined Pb films[7] can be extraordinarily robust, meaning that these films shows very little or no sign of defect- or fluctuation-driven suppression of superconductivity.[8] The surprising robustness of the superconducting critical state has been attributed to the minimal disorder in these high-quality films, in conjunction with

the presence of intrinsic vortex traps that evolve naturally from the quantum growth morphology. It is evident that quantum engineered superconductors represent ideal model systems for theories on low-dimensional superconductivity. Moreover, they may unveil novel critical-state properties that could potentially be useful for superconductive nanodevices.

The vast majority of studies in this field have focused on ultrathin Pb, which exhibits remarkably strong quantum size effects.[21,22,23,29,32,45] As noted, Pb has the property that the Fermi wavelength λ_F is almost perfectly commensurate with the interatomic layer spacing d along the <111> direction, that is, $2.07d \cong 3\lambda_F / 2$. The accidental matching of the electronic and crystallographic length scales results in reentrant bilayer-by-bilayer (RBBB) growth under the appropriate kinetic circumstances.[7] The RBBB growth mode represents a novel quantum growth phenomenon that is characterized by strong preference for bilayer growth with periodic interruptions of a single-monolayer or even a trilaye. The periodic interruption of the bilayer growth follows a well-defined beating pattern with a nine monolayer superperiod, which is due to the fact that λ_F and d are not exactly commensurate. This suggests the untested possibility of (1) altering the quantum growth mode by tuning the Fermi wave vector k_F via carrier doping; and (2) monitoring the superconducting properties of the resulting thin film alloy. The first possibility would expand the appeal of electronic growth to multi-component nanostructures. The second possibility in principle allows for systematic tuning of the density of states, electron-phonon coupling, and quantum coherence in low-dimensional superconductors.

In this chapter, we show that it is possible indeed to control the growth mode of metallic Pb films while maintaining the atomically smooth quantum growth morphology

by substituting Pb with up to 20% of Bi. The observed quantum oscillations in the thin film stability are fully consistent with the expected increase of the Fermi wave vector upon alloying, at least for the 11% random alloy. The superconducting properties of these quantum alloys indicate a significant increase of the critical temperature T_c, as expected from the increased electron density,[113] and a strongly enhanced upper critical field $H_{c2}(T)$, which can be attributed to increased carrier scattering in random alloys. Specifically, by increasing the bismuth content, it is possible to systematically increase the impurity scattering rate while leaving the boundary scattering rate unchanged. From the upper critical field data of Pb and PbBi quantum alloys, we establish an empirical correlation between the characteristic rounding of $H_{c2}(T)$ near T_c, which has been described in chapter 6 for quantum-confined Pb,[7,8] and the scattering mean free path. The puzzling rounding of $H_{c2}(T)$, which becomes increasingly pronounced with stronger quantum confinement[7,8] and increased scattering, implies a scattering induced crossover phenomenon that is strongly reminiscent of multi-gap superconductivity. If confirmed, this would be the first example of a multi-gap superconductor other than bulk MgB_2[13] although in principle any nanoscale superconductor with a quantized band structure could in principle be a multi-gap superconductor.

PbBi alloy films were deposited onto Si(111)7x7 surfaces in ultrahigh vacuum (UHV). The substrates were prepared by flashing up to ~ 1450 K in UHV. Co-deposition was employed to ensure random alloying. The Pb and Bi deposition rates were calibrated with X-ray Photoemission Spectroscopy (XPS), following the procedures outlined in Chapter 3. Films were deposited at ~120 K and post-annealed to produce atomically flat single-crystalline alloy films as observed with Low Energy Electron Diffraction (LEED)

for $Pb_{89}Bi_{11}$ and Scanning Tunneling Microscopy (STM) for both $Pb_{89}Bi_{11}$ and $Pb_{80}Bi_{20}$ thin film alloys. The optimal annealing temperature for creating atomically smooth films depends on the film thickness and Bi content. Thicker films (up to 23.5 ML) of $Pb_{89}Bi_{11}$ and $Pb_{80}Bi_{20}$ required annealing to room temperature. On the other hand, a 7 ML $Pb_{89}Bi_{11}$ deposit already becomes smooth at about 190 K while 150 K is sufficient to flatten a 7 ML $Pb_{80}Bi_{20}$ thin film. If the annealing temperature is too high, then the films are easily broken into 3D island morphology. These alloy films did not show any noticeable Bi segregation, according to XPS.

The Pb-Bi phase diagram does not show any ordered phases between 0% and 20% Bi.[114] This part of the phase diagram constitutes a solid solution with a face centered cubic structure and a lattice constant equal to that of bulk Pb (4.95 Å). There is a competing hexagonal epsilon phase above 20% Bi, which tentatively sets the upper limit of our alloying experiment. Finally, the superconducting properties of the films were studied using a SQUID magnetometer. The advantage of this contactless method and details of the measurements have been reported in chapter 6.

As already discussed, pure Pb(111) films evolve according to the RBBB quantum growth mode. The superperiod associated with the long wavelength beating pattern is $\lambda_{beat} = \lambda_F /(3\lambda_F - 4d) \cong 9.6$ ML for pure Pb.[115] Accordingly, we observed an even-odd crossover in the thin film stability of pure Pb at 4-5 ML, at 13-14 ML and at 22-25 ML;[7] this averages to $\lambda_{beat} = 9.5$ ML; this agrees well with the calculated value 9.6 ML. Here, we wish to tune the Fermi wavelength of Pb by introducing Bi, which has 5 valance electrons whereas Pb has 4. According to the free electron model, the Fermi wave vector

is given by $k_F = (3\pi^2 n)^{1/3}$ where n is the electron density. Therefore, the free electron density of a $Pb_{89}Bi_{11}$ film increases by 2.75% compared to Pb. This in turn increases the Fermi wave vector by 0.9% and, consequently, the associated beating period becomes ~12.7 ML. For $Pb_{89}Bi_{11}$ alloy films, the observed thickness sequence is 4-6*7-9-11-13-15-17-19*20… ML (this layer count excludes the wetting layer; see Ref 8) where * indicates the even-odd crossover. The agreement between the observed 13 ML periodicity and calculated 12.7 ML is striking. Furthermore, it is found in the first principles DFT calculations of Y. Jia *et al*. shown in figure 7.1. In these calculations, we observe that the location of the first crossover in DFT has shifted from 4-5 ML for clean Pb to 6-7 ML in the case of the $Pb_{89}Bi_{11}$ alloy and also see that a beat period of 13 ML is obtained. The QSE does not "reenter" after 20 ML, unlike the case of pure Pb.[8] Note, however, that the QSE is also very difficult to observe in pure Pb after the second crossover between 22-25 ML. The random scattering potential induced by random Bi substitution is most likely responsible for the relatively weaker QSE. Finally, higher concentration $Pb_{80}Bi_{20}$ alloys do not exhibit quantum growth at all in our experiments and simply follow classical layer-by-layer growth throughout the entire thickness range. This is consistent with the increased suppression of quantum coherence upon increasing the Bi content. Free electron model calculations for the $Pb_{80}Bi_{20}$ alloy would yield a beating period of ~17 ML.

The superconducting properties of the Pb films are significantly affected by alloying. The two fundamental equilibrium parameters, T_c and $H_{c2}(T)$ increase systematically with the Bi content. The T_c increase is similar to that in Pb-Bi bulk alloys, which has been attributed to an increasing electron density of states at the Fermi level and the enhanced

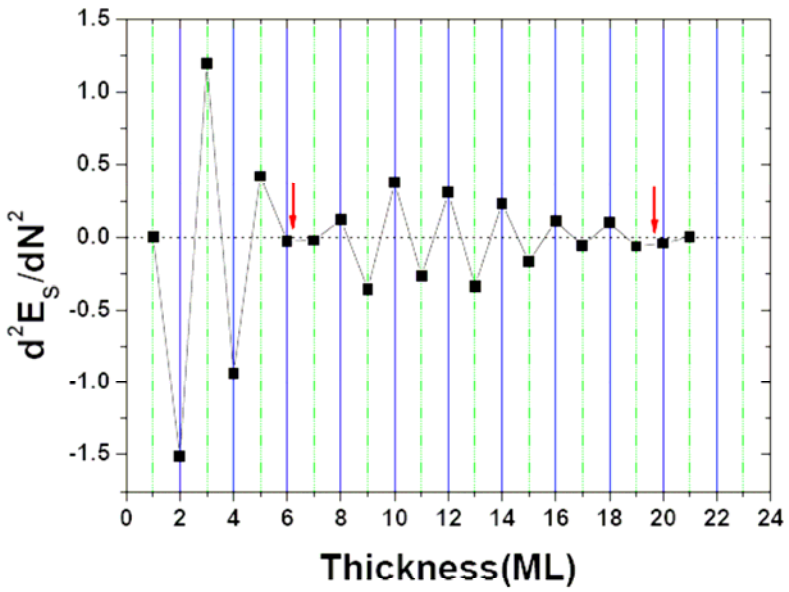

Figure 7.1: Second derivative of the total film energy of $Pb_{89}Bi_{11}$ alloy films obtained from first principles DFT calculations. (Y. Jia *et al*., to be published).

electron-phonon coupling.[113] Figure 7.2 shows the variation of T_c as a function of the inverse film thickness d. As observed for the pure Pb films,[8] we obtain that $T_c(d) = T_{c0}(1 - d_c/d)$ where T_{c0} is the critical temperature of the corresponding bulk alloy, and d_c the extrapolated threshold for the emergence of superconductivity. This linear variation with the inverse film thickness is usually interpreted as a boundary effect and naturally arises from the inclusion of a surface-energy term into the Ginzburg-Landau equations for the free energy of a superconductor.[88] Extrapolation to infinite ($1/d \to 0$ thickness) yields a remarkable agreement with the reported bulk T_c values of 7.20, 7.69 and 8.05 K for Pb, $Pb_{89}Bi_{11}$ and $Pb_{80}Bi_{20}$ alloys, respectively.[113]

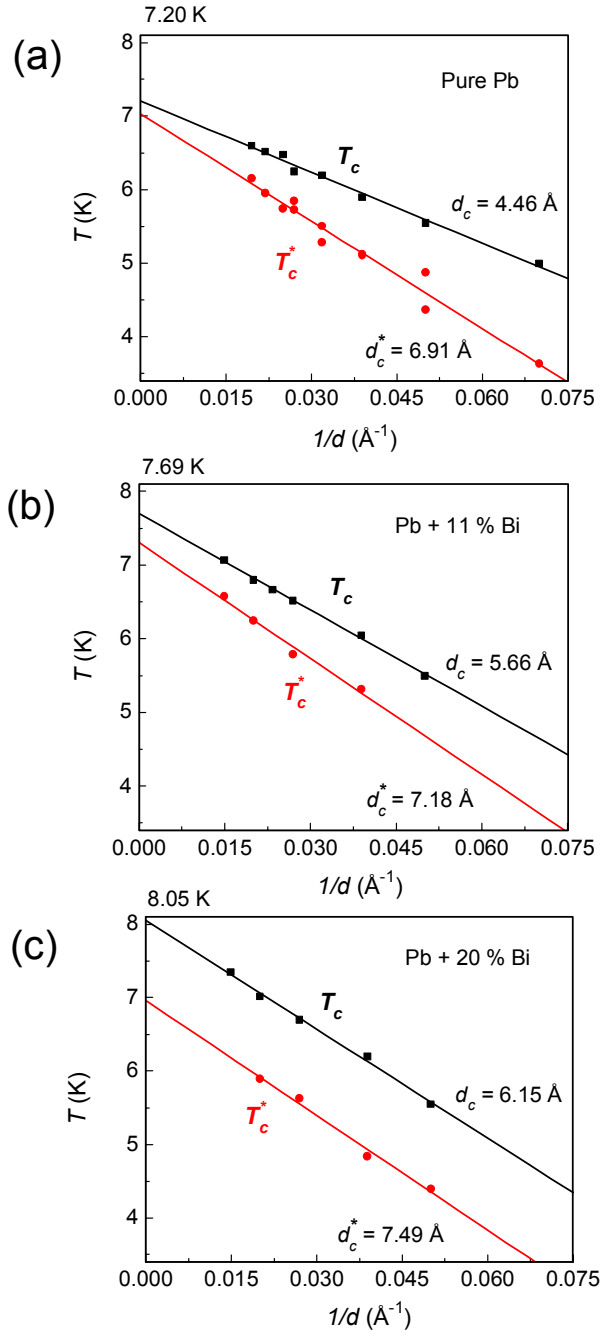

Figure 7.2: (a), (b), and (c), respectively, show T_c and T_c^* values for pure Pb, $Pb_{89}Bi_{11}$ and $Pb_{80}Bi_{20}$ alloys. T_c^* values are obtained by extrapolating the linear part of $H_{c2}(T)$ to zero dc field, as illustrated in figure 7.4.

For a given film thickness and temperature, H_{c2} increases with increasing Bi concentration. According to the well-known Ginzburg-Landau result[40] $H_{c2}(T) = \Phi_0 / 2\pi\xi_{GL}^2(T)$, this elevation of the upper critical field indicates a reduced coherence length ξ which must be due to increased scattering. The H_{c2} increase is still marginal in the thinnest films because scattering arises mostly from boundary scattering. However, for d near 20 ML, the H_{c2} of the $Pb_{80}Bi_{20}$ alloy has almost doubled compared to the H_{c2} of pure Pb, indicating that disorder scattering in the random alloy becomes increasingly important in thicker films. The carrier mean free paths have been calculated from the H_{c2} data using the "full value formula":[40]

$$\xi_{GL}(d) = 0.739[\xi_0^{-2} + 0.882(\xi_0 l)^{-1}]^{-1/2}(1 - T/T_c)^{-1/2} \tag{7.1}$$

where $\xi_0 = 905\,\text{Å}$ is the bulk BCS coherence length of bulk Pb.[40]

Figure 7.3 shows the variation of the mean free path with film thickness. The mean free path l_d of pure Pb varies linearly with the film thickness, indicative of simple boundary scattering. However, the mean free path of the 20% alloy seems to saturate due to the short impurity mean free path l_{imp}. The mean free path data can be fitted using Matthiessen's rule,

$$\frac{1}{l} = \frac{1}{l_d} + \frac{1}{l_{imp}}, \tag{7.2}$$

yielding values l_{imp} = 200 Å and 90 Å for the 11% and 20% alloys respectively, which agree reasonably with the values obtained from the $\rho \times l$ product of the corresponding

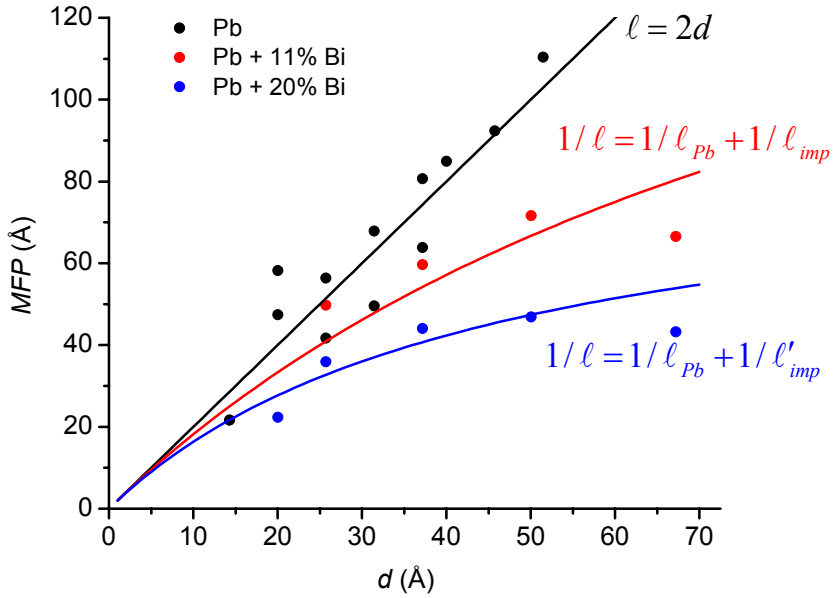

Figure 7.3: Mean free path values for pure Pb and both alloy films as described in the text.

bulk alloys.[*116]

Figure 7.4 shows the temperature dependence of the upper critical field for pure Pb and for the 11% alloy films. As described in chapter 6 for clean Pb, $H_{c2}(T)$ markedly flattens near T_c resulting in a characteristic "knee profile", which is particularly noticeable for the thinner films. In fact, this "knee profile" is even more pronounced for the $Pb_{89}Bi_{11}$ and $Pb_{80}Bi_{20}$ quantum alloys than for pure Pb. The strong curvature near T_c marks a significant departure from the Ginzburg Landau theory, which would predict

[*] According to this reference, the room temperature resistivity of pure Pb is $20\ \mu\Omega$ cm and the increase of resistivity of PbBi alloys is proportional to the Bi content; for example it becomes $31\ \mu\Omega$ cm for 11% alloy at room temperature. To first order approximation, we have assumed that phonon scattering contribution to resistivity is independent of Bi content. So, resistivity due to impurity scattering of 11 % alloy can be taken as $31-20=11\ \mu\Omega$ cm. Same consideration applies for 20 % alloy.

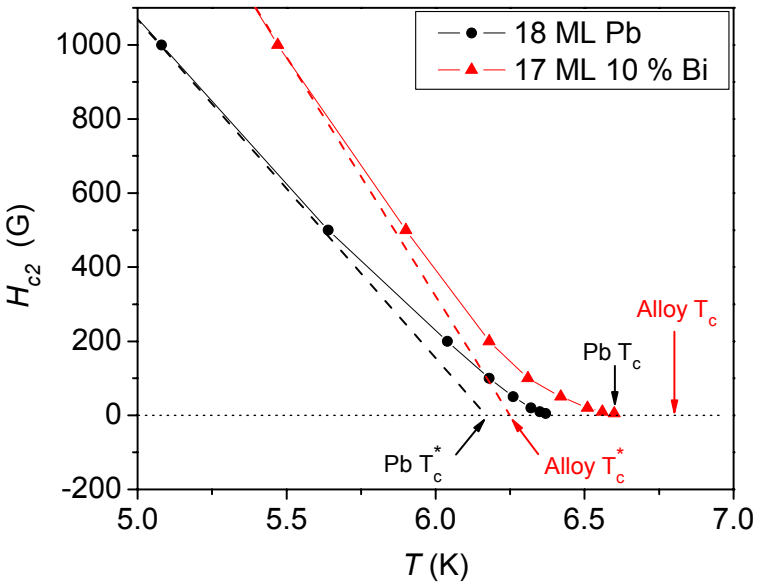

Figure 7.4: Temperature dependence of the upper critical field for pure Pb and 11% Bi alloy films of similar thickness, showing more pronounced curvature for the alloy.

$H_{c2} \propto (1-T/T_c)$. The upper critical field resumes Ginzburg-Landau like behavior below a characteristic temperature T_c^*, which is defined by extrapolating the linear part of H_{c2} curve to zero dc field (see figure 6.6 for an expanded temperature window). The T_c* values of the 11% and 20% alloys have been included in figure 7.2. Interestingly, the difference between T_c and T_c^* increases with Bi content in figure 7.2. Note that T_c^* (unlike T_c) does *not* extrapolate to the bulk T_c when $d \rightarrow \infty$.

Although a rounding of $H_{c2}(T)$ near T_c is often attributed to structural inhomogeneities in conjunction with the boundary conditions for the pair wave function,[89] the rounding here changes systematically with the fundamental nanoscale dimension *d,* because both T_c and T_c* vary linearly with $1/d$ while the low temperature slopes $dH_{c2}/dT \propto \left(d-d_c^*\right)^{-1}$ also

vary systematically with thickness.[8] Instead, we speculate that the knee profile of the upper critical field may signal multi-gap superconductivity, as observed in bulk MgB_2 ( ). This is not unreasonable, considering the fact that these ultrathin Pb and Pb-Bi alloy films exhibit strong quantum size effects, implying the existence of multiple 2D subbands. The knee profile would then reflect a crossover phenomenon, involving several superconducting subband channels that are coupled via off-diagonal electron-phonon coupling and interband scattering.[117]

According to the Anderson theorem,[95] T_c should be independent of scattering, that is, if the scattering is nonmagnetic. However, in the case of multi-gap superconductivity, this argument only holds for intraband scattering. Interband scattering would be pair-breaking, even if the impurities are non-magnetic.[118,119] If the electron-phonon coupling between the 2D subbands were zero, then the system would consist of "decoupled" superconductors, each having their own T_c. In such as case, superconductivity would nucleate in one of the subbands, presumably the lowest subband which has the longest scattering mean free path.[120],[121*] This onset then defines the T_c of the film. The higher and increasingly "dirtier" subbands would become superconducting at some lower temperature, which would mark a significant upturn of the scattering-enhanced upper critical field as seen in the experiment. When all bands are involved, linear H_{c2} behavior would be restored and the slope would be determined by the average mean free path. Note that interband scattering would not change these qualitative features but interband

[*] These QM calculations indicate increasing surface scattering with increasing k_z. Our argument is a clear-cut analogy with MgB_2, where superconductivity is nucleated in the clean σ band.

electron-phonon coupling could smear out this crossover region.[117] However, it is likely that some significant curvature remains, as in the case of MgB_2.[119,122]

The scenario of multigap superconductivity in these ultrathin films is speculative of course, and certainly requires theoretical understanding of the intraband and interband coupling- and scattering mechanisms. Although we have no direct information on the electron-phonon coupling in this system, the bismuth alloying experiment does provide new insight into the role of scattering. Inspired by the fact that interband scattering in a multigap superconductor suppresses the critical temperature by $\Delta T_c / T_c \propto \gamma / T_c$ where $\gamma \propto 1/l$ is the interband scattering rate,[118] we have plotted $(T_{c0} - T_c^*)/T_{c0}$ as a function of the inverse mean free path as determined from equation 7.1; see figure 7.5. Notice that the data of clean Pb and the 11% and 20% Pb-Bi alloys nicely collapse onto a straight line that passes almost through the origin. No such collapse is possible when plotting this quantity as a function of 1/*d*. This strongly suggests that the puzzling existence of T_c* (and H_{c2} upturn) must be attributed to a scattering-induced suppression or crossover of superconductivity. In the absence of magnetic scattering, this supports the possibility of multi-gap superconductivity

We emphasize that the collapse of the Pb and Pb-Bi alloy data cannot be achieved when plotting $(T_{c0} - T_c)/T_{c0}$ versus 1/*l*. In other words, the variation of T_c with layer thickness *d* thus appears to be the exclusive result of dimensionality, as originally predicted by Simonin[88] while T_c* appears to be related to a pair breaking scattering mechanism.

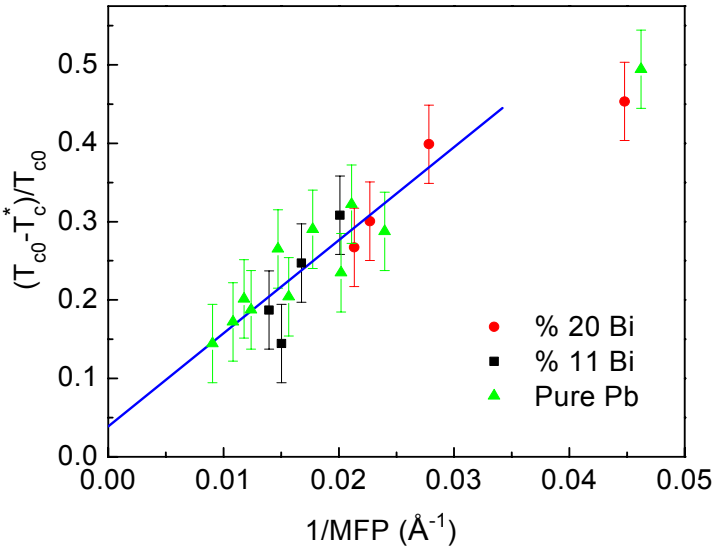

Figure 7.5: $(T_{c0} - T_c^*)/T_{c0}$ as a function of the inverse mean free path.

In summary, we have presented the first quantum growth experiment involving a random alloy. It is shown that the growth and superconductive properties of ultrathin films of Pb and Pb-Bi alloy films can be tailored via Fermi surface engineering. Alloying experiments shed an interesting new light on the puzzling curvature of the upper critical field near T_c in strongly confined 2D geometries. The curvature appears to be correlated, at least empirically, with the scattering mean free path. This indicates the intriguing possibility of multi-gap superconductivity in quantum-confined 2D electron systems. In contrast to bulk MgB_2 --the only other known multi-gap superconductor-- such a low-dimensional superconductor would be fully tunable, which opens up interesting possibilities for future experimental and theoretical research on low-dimensional multigap superconductors.

References

References

[1] J. M. Kosterlitz and D. J. Thouless, J. Phys. C **6,** 1181 (1973).
[2] D. P. DiVincenzo, Science **270**, 255 (1995).
[3] A.M. Goldman, N. Markovic, Physics Today **51**, 39 (1998).
[4] Herbert Kroemer, Nobel Lectures, Physics (Edited by Gösta Ekspong, World Scientific Publishing Co., Singapure, 2002).
[5] J. Faist, F. Capasso, C. Sirtori, D. L. Sivco, J. N. Baillargeon, A. L. Hutchinson, S. N. G. Chu, and A. Y. Cho, Appl. Phys. Lett. **68**, 3680 (1996).
[6] I. Žutić, J. Fabian, and S. Das Sarma, Rev. Mod. Phys. **76**, 323 (2004).
[7] M. M. Özer, Y. Jia, B. Wu, Z.Y. Zhang, and H. H. Weitering, Phys. Rev. B **72**, 113409 (2005).
[8] M. M. Özer, J. R. Thompson and H. H. Weitering, Nature Phys. **2,** 173 (2006).
[9] A.R. Smith, Kuo-Jen Chao, Qian Niu, and Chih-Kang Shih**,** Science **273**, 226 (1996).
[10] Z. Zhang, Q. Niu, and C.-K. Shih, Phys. Rev. Lett. **80**, 5381 (1998).
[11] A. Yazdani, Nature Phys. **2,** 151 (2006).
[12] D.B. Haviland, Y. Liu, and A.M. Goldman, Phys. Rev. Lett. **62**, 2180 (1989).
[13] M. Iavarone, G. Karapetrov, A. E. Koshelev, W. K. Kwok, G. W. Crabtree, D. G. Hinks W. N. Kang, Eun-Mi Choi, Hyun Jung Kim, Hyeong-Jin Kim, and S. I. Lee, Phys. Rev. Lett. **89**, 187002 (2002).
[14] A. Zangwill, Physics at Surfaces, (Cambridge University Press, Cambridge, 1998).
[15] H, H, Weitering, Growth and Electronic Structure of Thin Epitaxial Metal Layers, (PhD Thesis, University of Groningen, 1991).
[16] F. K. Schulte, Surf. Sci **55**, 427, (1976).
[17] D. Griffiths, Introduction to Quantum Mechanics, (2nd Edition, Prentice Hall, 2004).
[18] R. C. Jaklevic and J. Lambe, Phys. Rev. B **12**, 4146 (1975).
[19] P. J. Feibelman, Phys. Rev. B **27**, 1991 (1983).
[20] T.-C. Chiang, Surf. Sci. Rep. **39**, 181 (2000).
[21] W. B. Su, S. H. Chang, W. B. Jian, C. S. Chang, L. J. Chen, and Tien T. Tsong, Phys. Rev. Lett. **86**, 5116–5119 (2001).
[22] B. Altfeder, K. A. Matveev, and D. M. Chen, Phys. Rev. Lett. **78**, 2815 (1997).
[23] A. Mans, J. H. Dil, A. R. H. F. Ettema, and H. H. Weitering, Phys. Rev. B **66**, 195410 (2002).
[24] D.-A. Luh**,** T. Miller, J. J. Paggel, M. Y. Chou, and T.-C. Chiang, Science **292**, 1131 (2001).
[25] B. J. Hinch, C. Koziol, J. P. Toennies, G. Zhang, Europhys. Lett. **10**, 341 (1989).
[26] J. Braun and J. P. Toennies, Surf. Sci. **384**, L858 (1997).
[27] K. Budde, E. Abram, V. Yeh, and M. C. Tringides, Phys. Rev. B **61**, R10602 (2000).
[28] M. Hupalo, S. Kremmer, V. Yeh, L. Berbil-Bautista, E. Abram and M. C. Tringides, Surf. Sci. **493**, 526 (2001).
[29] V. Yeh, L. Berbil-Bautista, C. Z. Wang, K. M. Ho, and M. C. Tringides, Phys. Rev. Lett. **85**, 5158 (2000).
[30] E. Ogando, N. Zabala, E. V. Chulkov, and M. J. Puska, Phys. Rev. B **71**, 205401 (2005).
[31] H. Hong, C.-M.Wei, M.Y. Chou, Z.Wu, L. Basile, H. Chen, M. Holt, and T.-C. Chiang, Phys. Rev. Lett. 90, 076104 (2003).
[32] C. M. Wei and M. Y. Chou, Phys. Rev. B 66 233408 (2002).
[33] H. Lüth, Surfaces and Interfaces of Solid Materials, (3rd Edition, Springer Verlag, Berlin, 1995).
[34] Eric Ganz, Ing-Shouh Hwang, Fulin Xiong, Silva K. Theiss and Jene Golovchenko, Surf. Sci. **257**, 259 (1991).
[35] J. M. Carpinelli, H. H. Weitering, E. W. Plummer, and R. Stumpf, Nature **381**, 398 (1996).

[36] R. Shioda, A. Kawazu, A. A. Baski, C. F. Quate, and J. Nogami, Phys. Rev. B **48**, 4895 (1993).
[37] T. Nagao, J. T. Sadowski, M. Saito, S. Yaginuma, Y. Fujikawa, T. Kogure, T. Ohno, Y. Hasegawa, S. Hasegawa, and T. Sakurai, Phys. Rev. Lett. **93**, 105501 (2004).
[38] N. W. Ashcroft, N. D. Mermin, Solid State Physics (Saunders College Publications, Philadelphia, 1976).
[39] R. Wiesendanger, Scanning Probe Microscopy, (Cambridge University Press, Cambridge, 1994).
[40] M. Tinkham, Introduction to Superconductivity, (Dover Publications, Mineola NY, 1996).
[41] D.A. Evans, M. Alonso, R. Cimino, and K. Horn, Phys. Rev. Lett. **70**, 3483 (1993).
[42] E. Bauer and J.H. van der Merwe, Phys. Rev. B **33**, 3657 (1986).
[43] H. Okamoto, D. Chen, and T. Yamada, Phys. Rev. Lett. **89**, 256101 (2002).
[44] C.-S. Jiang, S.-C. Li, H.-B. Yu, D. Eom, X.-D.Wang, Ph. Ebert, J.-F. Jia, Q.-K. Xue, and C.-K. Shih, Phys. Rev. Lett. 92, 106104 (2004).
[45] M. H. Upton, C. M.Wei, M.Y. Chou, T. Miller, and T.-C. Chiang, Phys. Rev. Lett. 93, 026802 (2004).
[46] P. Czoschke, Hawoong Hong, L. Basile, and T.-C. Chiang, Phys. Rev. Lett. **93**, 036103 (2004).
[47] G. Kresse and J. Furthermuller, Phys. Rev. B **54**, 11169 (1996) and references cited therein.
[48] N.D. Lang and W. Kohn, Phys. Rev. B **1**, 4555 (1970).
[49] H. K. Onnes, Leiden Comm. **120b, 122b, 124c** (1911).
[50] F. London and H. London, Proc. Roy. Soc. **A149**, 71 (1935).
[51] V. L. Ginzburg and L. D. Landau, Zh. Eksperim. i Teor. Fiz. **20**, 1064 (1950).
[52] J. Bardeen, L. N. Cooper, and J. R. Schrieffer, Phys. Rev. **108** (1957).
[53] L. P. Gor'kov, Zh. Eksperim. i Teor. Fiz. **36**, 1918 (1959).
[54] G. Bednorz and K. A. Müller, Z. Phys. **B64**, 189 (1986).
[55] P. Dai, B. C. Chakoumakos, G. F. Sun, K. W. Wong, Y. Xin, and D. F. Lu, Physica C **243**, 201 (1995).
[56] W. Meissner and R. Ochsenfeld, Naturwissenschaften **21**, 787 (1933).
[57] J. R. Schrieffer, Nobel Lectures, Physics (Edited by Stig Lunqvist, World Scientific Publishing Co., Singapure, 1992).
[58] V. L. Berezinskii , Sov. Phys. JETP **32,** 493 (1970); Sov. Phys. JETP **34,** 610 (1971).
[59] J. Pearl, Appl. Phys. Lett. **5,** 65 (1964).
[60] M.R. Beasley, J.E. Mooij, and T.P. Orlando, Phys. Rev. Lett. **42**, 1165 (1979).
[61] J.M. Graybeal and M.R. Beasley, Phys. Rev. B **29**, 4167 (1984).
[62] R. E. Glover, III, Phys. Lett. 25A, **542** (1967).
[63] C. P. Bean, Phys. Rev. Lett. **8,** 250 (1962).
[64] A. Yazdani and A. Kapitulnik, Phys. Rev. Lett. **74**, 3037-3040 (1995).
[65] A. Bezryadin, C. N. Lau, and M. Tinkham, Nature **404**, 971-974 (2000).
[66] M. Zgirski, K.-P. Riikonen, V. Toubolotsev, and K. Arutyunov, Nano Letters **5**, 1029-1033 (2005).
[67] M. Hermele, G. Refael, M. P. A. Fisher, and P. M. Goldbart, Nature Physics **1**, 117 (2005).
[68] G. Blatter, M. V. Feigel'man, V. B. Geshkenbein, A. I. Larkin, and V. M. Vinokur, Rev. Mod. Phys. **66,** 1125 (1994).
[69] A.E. White, R.C. Dynes, and J.P. Garno, Phys. Rev. B **33**, 3549 (1986).
[70] J.M. Valles, Jr., R.C. Dynes, and J.P. Garno, Phys. Rev. B **40**, 6680 (1989).
[71] S.J. Lee and J.B. Ketterson, Phys. Rev. Lett. **64**, 3078 (1990).
[72] J.W.P. Hsu and A. Kapitulnik, Phys. Rev. B **45**, 4819 (1992).
[73] J.A. Chervenak and J.M. Valles, Jr., Phys. Rev. B **59**, 11209 (1999).
[74] T.R. Kirkpatrick and D. Belitz, Phys. Rev. Lett. **68**, 3232 (1992).
[75] M. A. Skvortsov, and M. V. Feigel'man, M.V. Phys. Rev. Lett. **95**, 057002 (2005).

[76] Y. Guo, Y.-F. Zhang, X.-Y. Bao, T.-Z. Han, Z. Tang, L.-X. Zhang, W.-G. Zhu, E. G. Wang, Q. Niu, Z. Q. Qiu, J.-F. Jia, Z.-X. Zhao, and Q.-K. Xue, Science **306**, 1915 (2004).
[77] D. Eom, S. Qin, M. Y. Chou, and C. K. Shih, Phys Rev Lett 96, 027005 (2006).
[78] R. Feng, E. H.Conrad, M. C. Tringides, C Kim, and P. F. Miceli, Appl. Phys. Lett. **85**, 3866 (2004).
[79] J. R. Clem, and A. Sanchez, Phys. Rev. B **50**, 9355 (1994).
[80] A. A. Abrikosov and L. P. Gor'kov, Zh. Eksp. Teor. Fiz. **35,** 1558 (1958); **36,** 319 (1959) [Sov. Phys. JETP **8,** 1090 (1959); **9,** 220 (1959)].
[81] A. A. Abrikosov, Rev. Mod. Phys, **76,** 975 (2004).
[82] G. J. Dolan and J. Silcox, Phys. Rev. Lett. **30,** 603 (1973).
[83] Xin-Yu Bao, Yan-Feng Zhang, Yupeng Wang, Jin-Feng Jia, Qi-Kun Xue, X. C. Xie, and Zhong-Xian Zhao, Phys. Rev. Lett. **95,** 247005 (2005).
[84] A. M. Finkel'stein, Pis'ma Zh. Eksp. Teor. Fiz. **45**, 37 (1987) [JETP Lett. **45**, 46 (1987)].
[85] S. Maekawa and H. Fukuyama, J. Phys. Jpn. **51,** 1380 (1981).
[86] M. Strongin, R. S. Thompson, O. F. Kammerer, and J. E. Crow, Phys. Rev. B **1**, 1078 (1970); The $\rho \times l$ product in Ref. 87 is slightly smaller ($\rho \times l = 1.1 \times 10^{-11}\,\Omega\mathrm{cm}^2$), which would imply that the $R_{\square}$ of the 5 ML film could even be lower (~150 Ω).
[87] I. Vilfan, M. Henzler, O. Pfennigstorf, and H. Pfnür, Phys. Rev. B **66,** 241306 (2002).
[88] J. Simonin, Phys. Rev. B **33,** 7830 (1986).
[89] S. Takahashi and M. Tachiki, Phys. Rev. B **33**, 4620-4631 (1986).
[90] V. M. Gvozdikov, Low. Temp. Phys. **25**, 936-942 (1999).
[91] L. N. Bulaevskiĭ, V. L. Ginzburg, and A. A. Sobyanin, Sov. Phys. JETP **68,** 1499 (1988).
[92] D. S. Fisher, Phys. Rev. B **22,** 1190 (1980).
[93] K. Maki, Annal. Phys. **34,** 363 (1965).
[94] T. P. Orlando, E. J. McNiff, Jr. and S. Foner, and M. R. Beasley, Phys. Rev. B **19,** 4545 (1979).
[95] P. W. Anderson, J. Phys. Chem. Solids **11,** 26 (1959).
[96] F Tafuri J. R. Kirtley, D. Born, D. Stornaiuolo, P. G. Medaglia, P. Orgiani, G. Balestrino, and V. G. Kogan, Europhys. Lett. **73,** 948 (2006).
[97] D. R. Nelson and V. M. Vinokur, Phys. Rev. B **48,** 13060 (1993).
[98] E. H. Brandt, Phys. Rev. B **55,** 14513 (1997).
[99] D. V. Shantsev, Y. M. Galperin, and T. H. Johansen, Phys. Rev. B **61,** 9699 (2000).
[100] A. M. Campbell and J. E. Evetts, Adv. in Phys. **50** 1249 (2001).
[101] G. Pasquini, L. Civale, H. Lanza, and G. Nieva, Phys. Rev. B 65, 214517 (2002).
[102] Th. Herzog, H. A. Radovan, P. Ziemann, and E. H. Brandt, Phys. Rev. B **56,** 2871 (1997).
[103] J. R. Thompson, K. D. Sorge, C. Cantoni, H.R. Kerchner, D. K. Christen, and M. Paranthaman, Supercond. Sci. Technol. **18,** 970 (2005).
[104] A. Gurevich and E. H. Brandt, Phys. Rev. Lett. **73,** 178 (1994).
[105] Yamasaki, Y. Nakagawa, Y. Mawatari, and B. Cao, Physica C **274**, 213 (1997).
[106] P. W. Anderson, Phys. Rev. Lett. **9,** 309 (1962).
[107] P. W. Anderson and Y. B. Kim, Rev. Mod. Phys. **36,** 39 (1964).
[108] A. Mans, J. H. Dil, A. R. H. F. Ettema, and H. H. Weitering, Phys. Rev. **B** 72, 155442 (2005).
[109] P. Czoschke, Hawoong Hong, L Basile, and T.-C. Chiang, Phys. Rev. Lett. **91**, 226801 (2003).
[110] N. Binggeli and M. Altarelli, Phys. Rev. Lett. **96**, 036805 (2006).
[111] L. Aballe, A. Barinov, A. Locatelli, S. Heun, and M. Kiskinova, Phys. Rev. Lett. **93**, 196103 (2004).
[112] M. Jalochowski and E. Bauer, Phys. Rev. B **38**, 5272 (1988).
[113] R. C. Dynes and J. M. Rowell, Phys. Rev. B **11**, 1884 (1975).

[114] R. Hultgren, P. D. Desai, D. T. Hawkins, M. Gleiser, K. K. Kelley, Selected Values of the Thermodynamic Properties of Binary Alloys, (American Society for Metals, Ohio, 1973).
[115] Y. Jia, B. Wu, H. H. Weitering, and Z. Zhang, Phys. Rev. B (in press).
[116] Klaus Schröder, CRC Handbook of Electrical Resistivities of Binary Metallic Alloys, (CRC Press, Boca Raton FL, 1983).
[117] M. Mansor, J. P. Carbotte, Phys. Rev. B **72**, 024538 (2005).
[118] I. I. Mazin, O. K. Andersen, O. Jepsen, O. V. Dolgov, J. Kortus, A. A. Golubov, A. B. Kuz'menko, and D. van der Marel, Phys. Rev. Lett. **89**, 107002 (2002).
[119] A. Gurevich, S. Patnaik, V. Braccini, K. H. Kim, C. Mielke, X. Song, L. D. Cooley, S. D. Bu1, D. M. Kim, J. H. Choi, L. J. Belenky, J. Giencke, M. K. Lee, W. Tian, X. Q. Pan, A. Siri, E. E. Hellstrom, C. B. Eom and D. C. Larbalestier, Supercond. Sci. Technol. **17,** 278 (2004).
[120] N. Trivedi and N. W. Ashcroft, Phys. Rev. B **38**, 12298 (1988).
[121] X.-G. Zhang and W. H. Butler, Phys. Rev. B **51**, 10085 (1995).
[122] M. Zehetmayer, M. Eisterer, J. Jun, S. M. Kazakov, J. Karpinski, A. Wisniewski, and H. W. Weber, Phys. Rev. B **66**, 052505 (2002).

Vita

Mustafa Murat Özer was born in Alaşehir, Turkey, in 1971. After graduating from Bornova Anatolian High School in İzmir, he attended the Middle East Technical University (METU) in Ankara, Turkey. After studying Mechanical Engineering one year, he decided to continue in the Physics Department of the same University and graduated in 1994. He earned a masters degree in Theoretical High Energy Physics in 1997 from METU. He arrived US in 1999 as a research scholar at UT, Knoxville. In 2000 he started the graduate school of the same University in High Energy Physics program. In 2002 he started a new research in Experimental Condensed Matter Physics within the groups of Dr. Hanno H. Weitering and Dr. James R. Thompson. While he was a student in these groups, he was awarded with "Paul H. Stelson" prize of UT Physics Department and won Nottingham Prize in 66th annual Physical Electronics Conference, Princeton NJ in 2006.